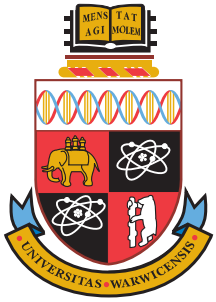


# Forces in a biological context

**Jonathan William Armond**

**Thesis**
Submitted to the University of Warwick
for the degree of
**Doctor of Philosophy**

*Supervisors:* Dr Matthew Turner and Prof Julie Macpherson

MOAC Doctoral Training Centre
September 2010


THE UNIVERSITY OF
WARWICK

**Abstract**

Theoretical modelling of the microtubule-Dam1-ring force generation mechanism and the pulling of tubes from surface-supported lipid bilayers are presented and discussed. Atomic force microscopy (AFM) force data of tube pulling experiments is analysed and compared with theoretical predictions.

Features common to recent computational models are simplified and examined independently where possible. In particular, the steric confinement of the Dam1 ring on a microtubule (MT) by protofilaments (PFs), the powerstroke produced by curling PFs, the depolymerisation of the MT, and the binding attraction between Dam1 and the MT are modelled. Model parameters are fitted to data. Functional force generation is equally demonstrated when attachment is maintained by steric confinement alone (protofilament model) or by a binding attraction alone (binding model). Moreover, parameters amenable to experimental modification are shown to induce differences between the protofilament model and the binding model. Changing the depolymerisation rate of MTs, the diffusion coefficient of the Dam1 ring, or applying an oscillating load force will allow discrimination of these two different mechanisms of force generation and kinetochore attachment.

A previously described theoretical model of pulling lipid bilayer tubes from vesicles is modified for the case of pulling tubes from surface-supported lipid bilayers. A shape equation for axisymmetric membranes is derived variationally and solved numerically for zero pressure. Free energy profiles and force curves are calculated for various AFM probe sizes and compared to experimental data where a ground flat AFM probe is used to pull tubes from surface-supported lipid bilayers. The predicted force curves partially fit the experimental data, although not at short distances, and estimates of the bilayer surface tension are given. Pressure and volume profiles are calculated for the extension of the model to the nonzero pressure case.

# Contents

# List of Figures

# List of Tables

# Acknowledgements

First of all I would like to thanks my supervisors, Dr. Matthew Turner and Prof. Julie Macpherson, for giving me the opportunity to work with them and for providing guidance throughout the project. I would also like to thank Dr. Neil Wilson for his training on the AFM in the early days.

I would like to thank Alison Rodger, Dorothea Mangels, and Mónica de Lucena from MOAC, for their help throughout these past years.

My family has always supported my choice to avoid a 'real' job and pursue my love of science, and for this I am most thankful.

Finally, to my fiancé Elina, for always supporting, loving and encouraging me, I am deeply grateful - σ'αγαπώ πολύ.

This work was funded by the Engineering and Physical Sciences Research Council (EPSRC) through the Molecular Organisation and Assembly in Cells (MOAC) Doctoral Training Centre.

# Declaration

The work contained herein is entirely original and my own work, except where acknowledged in the text. I confirm that this thesis has not been submitted for a degree at another university.

Part of this work has been published in the following journal article:

J. W. Armond and M. S. Turner. Force transduction by the microtubule-bound Dam1 ring. *Biophysical Journal*, 98:1598-1607, 2010.

A reprint of this article is included in Appendix D.

# 1 Introduction

## 1.1 Interface of physics and biology: biological physics

Biological physics as a field can perhaps be said to have begun with E. Schrödinger's classic book *"What is life?"* [4]. Since then science at the interface of physics and biology has had a fruitful development, perhaps most notably in biomolecular structure determination using physical techniques, e.g., X-ray crystallography, nuclear magnetic resonance (NMR), electron microscopy (EM). Optical traps and atomic force microscopes (AFMs) allow forces at the single molecule level to be measured. Statistical mechanics, both equilibrium and nonequilibrium, proves extremely valuable in understanding microscopic biological processes. Many of the pioneers of molecular genetics have been physicists, e.g., Francis Crick and Max Delbrück. Biological physics may be described as the sub-discipline of physics concerned with applying physical principles to understand biological systems, and furthermore, using biological systems (which are often complex, disordered and far-from-equilibrium) to infer new physics.

This thesis is an attempt to form an understanding of two simplified biological systems from a biological physics perspective. The following topics will be discussed:

- a mathematical model of the Dam1 ring-based microtubule (MT) force transduction system that operates during mitosis (Chapter 4).
- theoretical and experimental investigations into the formation of lipid membrane tubes from surface-supported bilayers (Chapter 5 and Chapter 7), which has relevance to inter- and intra-cell trafficking.

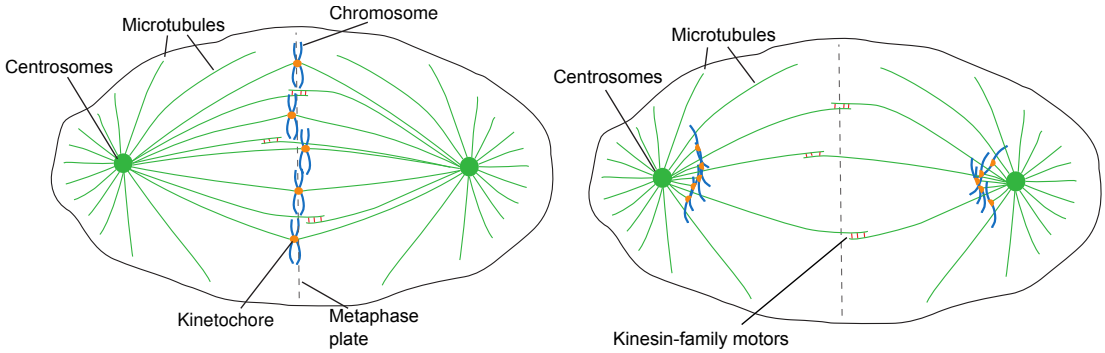


**(a)** At metaphase chromosomes are condensed and visible, and line up in an imaginary plane called the metaphase plate.

**(b)** After anaphase has completed the chromosomes are segregated to opposite poles of the cell.

**Figure 1.1:** Diagram of the transition between metaphase and late anaphase.

## 1.2 Chromosome segregation

Essential to the continuation of life is the ability of cells to replicate. The stage during the lifetime of a cell when replication visibly takes place is called mitosis during which a cell divides into two. Deoxyribonucleic acid (DNA) forms the cell's genome which provides an encoded description of the proteins required by the cell and performs regulatory functions. It is organised into dense structures called chromosomes which condense and become visible during mitosis. A critical feature of mitosis is ensuring that the correct number of copies of the cells DNA is transported to each daughter cell before division.

### 1.2.1 Mitosis

Mitosis is the mechanism of cell replication in eukaryotic cells, first observed by W. Flemming in 1882 [5]. Mitosis can itself be divided in six phases: prophase, prometaphase, metaphase, anaphase, telophase and cytokinesis. At prophase the cell's chromosomes condense, becoming visible, and a scaffold called the mitotic spindle begins forming from MTs. In prometaphase the nuclear envelope breaks down and the *centrosomes* – a microtubule organising centre (MTOC) that nucleate MTs – are positioned at both poles of the cell making the spindle bipolar. During metaphase, MTs attach to chromosomes, becoming kinetochore-attached microtubules (kMTs), and are organised into alignment on an imaginary plane called the metaphase plate at the centre of the cell by the mitotic spindle. After alignment, the cell proceeds to anaphase where chromosomes are segregated and transported to the cell poles, while MTs retract. By telophase the two sets of chromosomes are at opposite cell poles and nuclear envelopes begin to form around them. Finally, in cytokinesis, the cell is physically divided by a contractile

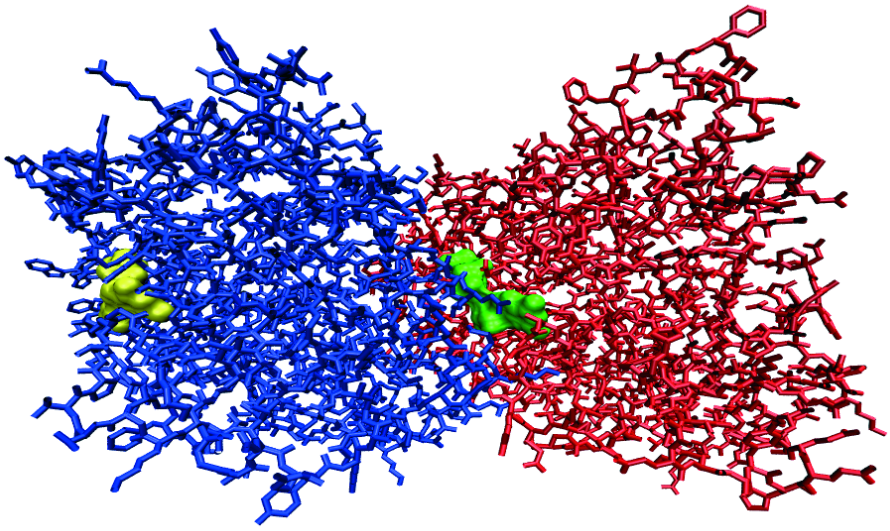

**Figure 1.2:** Structure of the tubulin dimer. The $\alpha\beta$-tubulin dimer is shown with guanosine 5′-triphosphate (GTP) (green) bound to the $\alpha$-tubulin (red), and guanosine 5′-diphosphate (GDP) (yellow) bound to the $\beta$-tubulin (blue).

ring of myosin and actin filaments and two diploid daughter cells are produced[1].

### 1.2.2 Microtubules

Microtubules (MTs) are 25 nm diameter fibres, composed of $n$ (typically $n = 13$) parallel protofilaments (PFs) forming a hollow cylinder. Each PF is built from stacked 8 nm long tubulin protein dimers. Tubulin exists primarily as a dimer (shown in Figure 1.2) composed of $\alpha$-tubulin and $\beta$-tubulin, each of which is present in all eukaryotes and is approximately 55 kDa in mass. Each monomer binds one guanosine 5′-triphosphate (GTP) molecule, but only the GTP bound to $\beta$-tubulin is hydrolysable to guanosine 5′-diphosphate (GDP). In the MT lattice adjacent protofilaments are staggered; the monomers are arranged as a 3-start helix[2]. As a consequence, after a complete turn the last $\alpha$-tubulin is adjacent to the first $\beta$-tubulin of the next turn, creating a seam in the MT lattice [6].

MTs are rigid structures with a flexural rigidity of $7.9 \pm 0.7 \times 10^{-24}\ \mathrm{N\,m^2}$ [7]. Their length is highly variable and is subject to a phenomenon known as *dynamic instability* [8]. Within a population of MTs with steady average length, individual MTs will undergo periods of growth, followed by rapid shrinking, or *catastrophes*, as shown in Figure 1.3. During a catastrophe, the MT may be *rescued* and polymerisation restarted. This dynamic instability is caused by the difference in structure between tubulin dimers containing GTP-$\beta$-tubulin and those containing GDP-$\beta$-

[1]During the similar process of meiosis, only one set of chromosomes is passed to daughter cells, resulting in haploid cells.

[2]A $n$-start helix means one complete turn extends the fibre by $n$ monomer lengths.

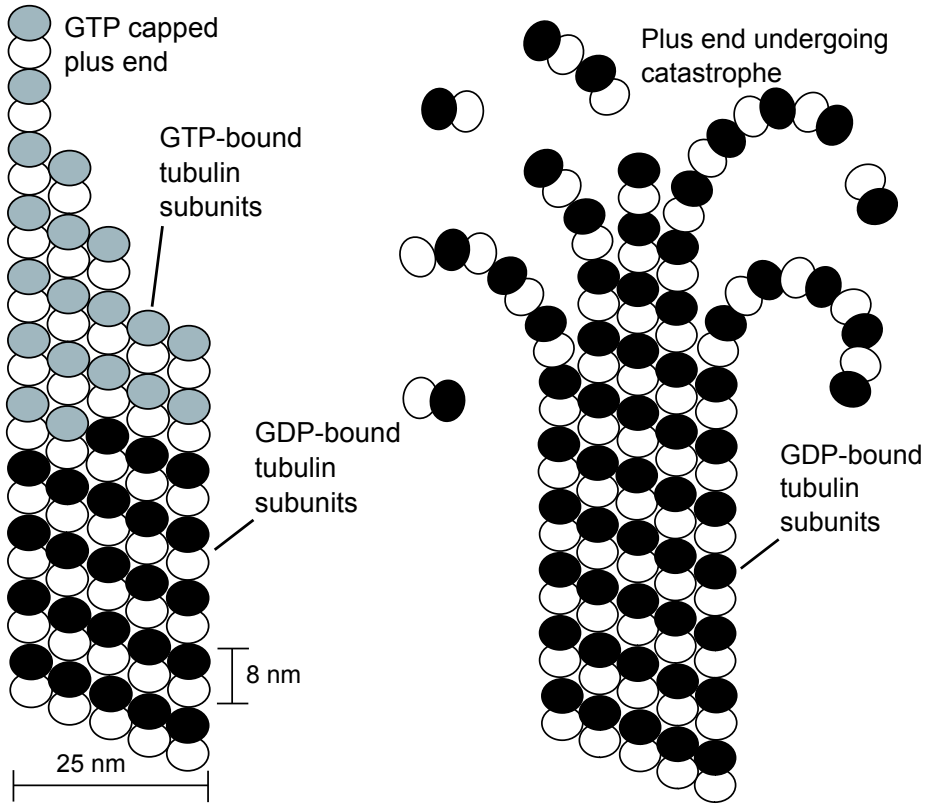


**(a)** Growth **(b)** Shinkage

**Figure 1.3:** Diagram of microtubule dynamic instability. During growth protofilaments (PFs) extend linearly and close up to form the microtubule (MT) lattice. After the GTP cap is lost, a catastrophe occurs resulting in rapid depolymerisation of curling PFs.

tubulin; the former is straight and the latter bent. MTs grow by addition of dimers containing only GTP. The GTPase activity of tubulin stochastically hydrolyses the GTP bound to $\beta$-tubulin to GDP. However, as long as a cap of GTP-$\beta$-tubulin remains at the growing end, the MT lattice constrains the GDP-bound tubulin in a straight configuration, storing elastic energy. Randomly, the cap may become hydrolysed, unleashing the stored energy and causing the MT to undergo catastrophe.

With a sufficiently high concentration of tubulin MTs may be grown in vitro. MTs extend by tubulin polymerisation onto PFs, forming long sheet-like extensions from the MT end, which close up to form the lattice. Depolymerisation occurs by a different process in which PFs laterally separate, adopting a curved 'ram's horn' configuration, before individually depolymerising.

MTs emanate from centrosomes, a type of MTOC, where they are nucleated by the $\gamma$-tubulin ring complex [9, 10]. During mitosis, MTs form the mitotic spindle by attaching to the kinetochores located at centromeric-regions of chromosomes and bridging with MTs originating from the opposite centrosome.

### 1.2.3 Forces in anaphase

To achieve segregation and complete anaphase, a force must be applied to the chromosomes to overcome drag in the cytosol and move polewards [11]. This force could conceivably be produced by non-kinetochore MTs forming the spindle bracing against each other and extending. Alternatively, the force could be generated by motor proteins at the kinetochore, using kMTs as tracks. Yet another possibility is the depolymerisation of kMTs pulls the kinetochores towards the poles. In particular, it has been suggested that a protein ring complex called Dam1 is directly involved in force generation. Much effort has been applied to the solution of this problem; major results are discussed in detail in §2.1.

## 1.3 Lipid bilayer tubes

In certain situations biological cells form tubes connecting intra-cellular compartments, which allow the transfer of material and signals. Some types of bacteria also form inter-cellular tubes. The tubes are formed from the lipid membranes that enclose the cell itself, as well as internal cell compartments such as the nucleus and endoplasmic reticulum.

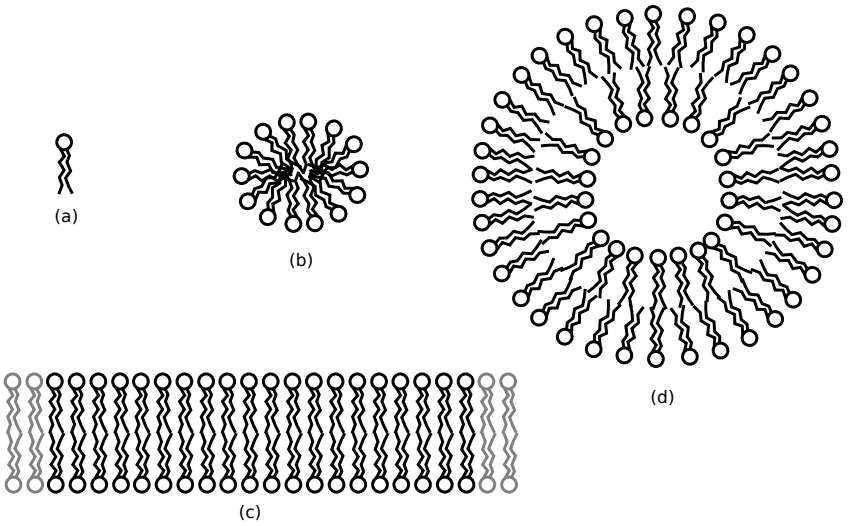


**Figure 1.4:** Micelles, vesicles and membranes - three common lipid structures in aqueous environments. The schematic representation here shows a cross-section; each of these structures is three-dimensional. (a) A single lipid molecule; (b) lipids aggregate to contain their hydrophobic tails away from water, forming a micelle; (c) two layers of lipids, or leaflets, come together forming an extended bilayer membrane; (d) a vesicle is essentially a closed bilayer membrane.

### 1.3.1 Lipids

A wide group of molecules are known as lipids including fatty acids, glycerides and sterols. The major class of lipids that form biological membranes are phospholipids, which are roughly cylindrical and composed of three parts: a hydrophobic tail and a hydrophilic head, connected by a glycerol with a phosphate group. Containing both hydrophobic and hydrophilic parts means phospholipids are amphipathic. The hydrophobic tail is a pair of hydrocarbon chains, saturated or unsaturated, with a carboxyl group joining them to the glycerol. The length and type of tail affects the melting temperature of the lipid. Common hydrophilic heads include phosphatidylcholine, phosphatidylethanolamine, phosphatidylserine and phosphatidylinositol. The different head types can have different sizes and different charges.

### 1.3.2 Membranes

In an aqueous environment, the amphipathic nature of phospholipids causes them to form structures that expose the hydrophilic heads to the water and contain the hydrophobic tails. Three common structures, shown in Figure 1.4, are micelles, vesicles and membranes; both vesicles and membranes are bilayers.

Membranes are essential for cells. Most importantly, they define the boundary of the cell itself. They also allow the cell to maintain separate compartments such

as the nucleus and endoplasmic reticulum. Furthermore, the natural environment of many proteins is within the membrane bilayer itself. Many of these proteins perform signal transduction across the membrane or form pores to allow the transmission of small molecules and other proteins.

### 1.3.3 Tubes

Membranes are flexible and, at biological temperatures, usually fluid, i.e. the constituent lipid molecules are free to move within the membrane. This important difference with other elastic materials results in an absence of shear stress, as lipids can move in response to a force. This allows large elastic deformations such as the formation of long, thin tubes. The formation of tubes will be discussed in detail in §2.2 and Chapter 5.

## 1.4 Aims of this thesis

This thesis is concerned with modelling force in two different biological contexts: MT-Dam1 ring attachment and lipid tube formation. The aims, which apply to both contexts, are to formulate parsimonius theoretical models of the biological system in question and, crucially, compare predictions with data. In the case of lipid tube formation, experiments have been performed for this purpose; for the MT-Dam1 ring attachment problem, published data has been used.

# 2

# Literature review

The mitotic spindle and the process of chromosome segregation have been the subject of extensive study in the last half-century. The literature most relevant to the question of force production during segregation is summarised in the first section of this chapter[1]. Recent advances in the sensitivity of force measurements, enabled by technologies such as optical trapping and atomic force microscopy, has led to direct measurements of the forces involved in membrane fusion, fission and tube formation. Previous lipid membrane modelling efforts and some recent experiments involving the formation of lipid membrane tubes are described in the second section of this chapter.

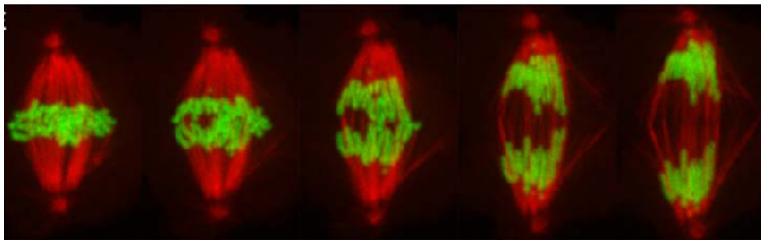

**Figure 2.1:** Time-lapsed images of a *Dropsophila* S2 cell undergoing anaphase. The tubulin is labelled red; the DNA is labelled green. In the first image the chromosomes reside at the metaphase plate at the cell centre. By the end of the sequence the chromosomes are fully segregated. Figure taken from [1].

## 2.1 Mitotic force generation

In §1.2.3 it was noted that the movement of chromosomes during segregation in anaphase A (see Figure 2.1) requires an applied force to overcome viscous drag, at observed velocities in the range 0.2 to 0.5 $\mu$m/min [1]. This force has been estimated to be between 0.1 and 10 pN per chromosome [12–15]. Measurements made by observing, using phase-contrast microscopy, the deflection of a thin glass needle snagged by a chromosome, have shown the stalling force, that is, the force required to halt chromosome motion, is on the order of 700 pN for the whole spindle (for *Melanoplus sanguinipes*, or grasshopper, spermatocytes) [13].

In the 1960's, electron microscopy made it possible to visualise MTs within the mitotic spindle region [16]; previously unidentified fibres had been observed using polarised light microscopes [17]. Around 20–25 microtubules attach to each kinetochore in mammalian cells [18]. It was first proposed that the depolymerisation of MTs during anaphase could be performing the mechanical work, thus generating a force, by Inoué and Sato in 1967 [19]. The mechanisms for the continued attachment and force generation of a kinetochore to a depolymerising MT are still not fully understood. Furthermore, it is not known whether two distinct mechanisms are independently responsible for attachment and for force generation, or if a single mechanism or several coupled mechanisms cooperate to ensure segregation. A number of mechanisms have been proposed over several decades and will be explored later in this section.

### 2.1.1 Directional instability

It is observed that during anaphase A (see Figure 2.1) chromosomes do not follow a direct route toward the poles. Instead, chromosome movement, in several different cell types, abruptly switches between poleward and anti-poleward directions. Each phase lasts around 1.5 min on average. This property is termed *directional instability* [20], and also occurs in late prometaphase and metaphase, although may have a different cause in these phases. Poleward motion is driven by a force generating mechanism at the kinetochore; the motion is opposed by polar ejection forces which push chromosome arms away from the pole, although laser microdissection experiments show this is not necessary for instability [21]. The polar ejection force is thought to arise from the action of non-kinetochore-MT-based kinesins on chromosome arms, known as chromokinesins [22], or from

[1]The microtubule (MT)-Dam1 force generation model in Chapter 4 is based on the assumption that Dam1 forms a ring and was developed before recent results suggesting otherwise. To allow the model to be assessed on its own merits, the most recent literature is deferred for review in the discussion in Chapter 8.

the polymerisation of MTs against chromosome arms [23].

### 2.1.2 Kinetochore attachment and force coupling

The discoveries of several protein complexes involved in initiating and maintaining kinetochore attachment are beginning to shed light on the anaphase chromosome segregation mechanism. Together with new in vitro data, and electron microscopy observations, these results are providing a rich source of speculation on the force coupling and transduction mechanism.

#### 2.1.2.1 Protofilament curl

Cryo-electron microscopy and video-enhanced differential-interference contrast (DIC) microscopy has revealed depolymerising MTs to have frayed plus ends, where individual protofilaments (PFs) separate laterally and adopt a highly curved conformation prior to dissociation of individual tubulins or short oligomers [24–26]. These structures have been referred to as 'nano-hooks' and 'rams-horns'. The transformation from straight ends to curled ends is thought to be the mechanism behind the rapid catastrophes that are part of the dynamic instability of MTs. The tubulin dimer bound to guanosine 5'-triphosphate (GTP), or tubulin-GTP, has a straight conformation across the dimer bond [27], while tubulin bound to guanosine 5'-diphosphate (GDP) or tubulin-GDP has a 11° bent conformation [28]. During MT growth, tubulin-GTP is added to the plus-end of the MT lattice. A growing MT maintains a monolayer cap of tubulin-GTP near the growing tip [29]. The GTPase action of tubulin beneath the cap hydrolyses GTP so the majority of the lattice is constructed from tubulin-GDP. Due to the curved conformation of tubulin-GDP, the PFs in the MT are under strain, hence store elastic energy. This energy is thought to drive the 'catastrophic' depolymerisation of MTs [30, 31].

By fixing a silica bead to the side of a MT and then inducing depolymerisation, Grishchuk et al. were able to measure the force exerted on the bead by the conformational change of PFs using an optical trap system [32]. Assuming, due to curvature considerations, the bead is attached to only 1–2 PFs, and compensating for a ten-fold lever arm effect, they estimate a maximum force production of 5 pN for 1–2 PFs. Extrapolating to the full MT cylinder yields a force in the range 30–65 pN.

Prior to the actual observation of curved, depolymerising PFs and the force measurements, a model known as the 'conformational wave model' was postulated to harness the conformational change of PFs to drive kinetochore movement [33, 34]. These measurements have lent support to the notion that the energy re-

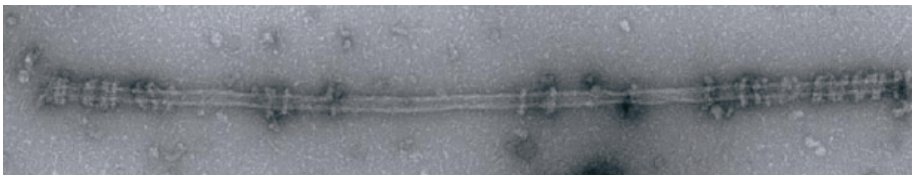

**Figure 2.2:** Electron micrograph of Dam1 rings bound to a microtubule. Figure taken from [36].

leased by the curling process is directly involved in driving chromosome transport [35].

#### 2.1.2.2 Dam1 complex

The discovery that the yeast Dam1 complex could form a ring around MTs in vitro [36, 37] caused considerable speculation that the mechanism of coupling between depolymerising MTs and the kinetochore had been found. Figure 2.2 shows Dam1 rings populating an MT. Dam1, also known as DASH, is a 210 kDa complex of 10 proteins: Dam1, Duo1, Dad1, Dad2, Spc19, Spc34, Ask1, Dad3, Dad4 and Hsk3 [37]. Dam1 rings have an outer diameter of about 54 nm and an inner diameter of about 32 nm [36]; the diameter of a microtubule is 25 nm meaning the Dam1 ring is apparently not a tight fit. Three-dimensional reconstruction by electron microscopy single-particle analysis indicates the complex has a C-terminal domain that protrudes toward the MT [38]. End-on electron microscopy images show the ring having a 16-fold symmetry [39].

Dam1 complex is essential for the proper segregation of chromosomes in budding yeast (*Saccharomyces cerevisiae*) [40, 41]. Furthermore, the artificial recruitment of Dam1 complex to deoxyribonucleic acid (DNA) lacking a centromere produces a vastly simplified artificial kinetochore that is capable of bi-orientation and segregation [42]. In fission yeast (*Schizosaccharomyces pombe*) Dam1 is non-essential, but important for avoiding mis-segregation problems [43]. No analogous protein complex has yet been found in higher eukaryotes [44], although the Ska complex may prove to perform a similar function in human cells [45].

Fluorescence microscopy of Dam1 rings on taxol-stabilised MTs in vitro reveals that Dam1 rings can diffuse freely along the MT. Moreover, the Dam1 ring remains attached during depolymerisation of the MT to which it is bound [39], but reduces the depolymerisation rate around four-fold. Rings with the C-terminal protrusion truncated only slow depolymerisation marginally [46], indicating specific binding between the protuberance and specific sites on the MT lattice.

Dam1 rings, bound to a polystyrene bead, can remain attached to depolymerising MTs even when an optical trap is used [47] to apply forces via the bead in the range 0.5–3 pN opposite to the direction depolymerisation [48]. In fact, when

applying such a load force the Dam1 ring can remain attached as the MT elongates, tracking the MT tip. The MT depolymerisation rate is reduced at higher load forces. Furthermore, the frequency of ring detachment events is also increased [49].

#### 2.1.2.3 KNM network and Ndc80

The highly-conserved KNM network – comprising KNL-1, Mis12 complex and Ndc80 complex – has emerged as essential for kinetochore interactions with MTs *in vivo*. Depletion of KNL prevents kinetochore-attached microtubule (kMT) associations. Depletion of Mis12-like complexes inhibits kinetochore assembly, and depletion of Ndc80 hinders the ability of the kinetochore-MT system to hold tension [50].

The Ndc80 complex is of particular interest to chromosome segregation. It is a complex of four proteins: Ndc80 (known as Hec1 in human cells), Nuf2, Spc25 and Spc24, in equal stoichiometric ratios [51], with a total weight of ~170–190 kDa [52]. The complex has been shown to be essential for chromosome segregation [53–55]. Structurally, the complex is a 57 nm rod with globular domains at each end [56]. Electron microscopy of MTs and Ndc80 at saturating concentration revealed that Ndc80 binds, and coats, the MT at an approximately constant angle with respect to the MT polarisation creating a barbed MT [50].

By the same procedure used for Dam1 force measurements, purified Ndc80, bound onto a bead held in an optical trap, has been shown to remain attached to depolymerising microtubules (dMTs) under tensions in the range 0.5–2.0 pN. However, arrays of Ndc80 are required to maintain attachment; single complexes cannot sustain force. Individual Ndc80 complexes are also able to diffuse along the MT [57]. Despite this ability to transduce force, Ndc80 and Dam1 are not redundant in yeast; both are required for MT attachment [58]. In fact, Dam1 enhances the ability of Ndc80 to remain attached to dMTs as a cooperative processivity factor, increasing the distance travelled three-fold and decreasing detachment five-fold. Furthermore, the mean force sustainable increased about two-fold to $4.4 \pm 0.2$ pN [59]. The interaction of the Ndc80 complex with the kinetochore, the MT and the Dam1 complex [44] suggests it could function as a linking complex between the Dam1 complex and the kinetochore.

#### 2.1.2.4 Fibrils

Electron tomography of mitotic $PtK_1$ cells has revealed the presence of tenuous fibrillar structures apparently joining the kinetochore and the curved PFs at the depolymerising end of kMTs. Statistical analysis of hundreds of images of PFs in-

dicates that depolymerising kMTs associated with fibrils have reduced curvature near where they join the MT, but increased curvature close to their fibril attachment. It is argued that this is due to the fibril opposing the force generated by PF strain release. The identity of the fibrils remains unknown; candidates include CENP-E and Ndc80 [60]. It should be stressed that the fibrils in the electron microscopy (EM) images are somewhat faint and it is not clear whether the fibrils bind directly to the MT or to another MT-bound structure.

#### 2.1.2.5 Molecular motors

In addition to MT depolymerisation-based chromosome segregation theories, a significant body of evidence has been accumulated toward the involvement of molecular motor proteins in the segregation process [61]. It has been suggested that, due to the necessity of highly accurate chromosome segregation, multiple force production mechanisms may have co-evolved; moreover, different mechanisms may exist or dominate in different species [11].

### 2.1.3 Models of the force transduction mechanism

Many models have been proposed to describe the mechanism of force transduction due to kinetochore-MT coupling, with increasing incorporation of molecular biology information in more recent studies. The models are described here, categorised by the key mechanism they propose.

#### 2.1.3.1 Force-balance models

Joglekar and Hunt describe a force-balance model that reproduces chromosome directional instability [62]. They assume MTs are attached to chromosomes by a Hill sleeve (see §2.1.3.3) and pull chromosomes toward the poles, while unidentified 'polar ejection forces' oppose this. Added to this force balance is a centre spring connecting sister chromatids and a spring connecting each Hill sleeve to the chromosome. With appropriate parameters, their model effectively reproduces the oscillations in chromosome position observed in vivo for newt lung cells.

Civelekoglu-Scholey et al. also model chromosome motility using a force-balance model [15]. In their model, the contributions to the resultant force experienced by a kinetochore is the sum of the poleward directed forces due to depolymerisation motors at the kinetochore and MT depolymerisation at the centromere, and anti-poleward directed forces due to chromosome arm polar ejection forces, chromosome drag and tension due to the attachment with its sister chromosome.

The model is able to reproduce both metaphase chromosome oscillations and anaphase chromosome motility.

However, both of these force-balance models fail to provide mechanistic explanations for how the included forces are generated, and furthermore contain many parameters, several of which are not constrained by experiment.

#### 2.1.3.2 Treadmilling

Significant support for the idea that a dMT could generate force was provided by the discovery that MTs stochastically switch from growth to rapid shrinking (also known as a *catastrophe*), by a process called *dynamic instability* [8]. In steady state conditions in vitro, net tubulin addition occurs at one end of a MT (plus-end) and net loss occurs at the other (minus-end), as observed by electron microscopy [63]. The resulting unidirectional flux of tubulin subunits from the plus-end to the minus-end is called treadmilling and has been suggested as a mechanism for the translocation of chromosomes [64]. Kinetic modelling of the treadmilling process shows that an energy source, provided by GTP hydrolysis, is necessary to maintain the flux of tubulin [65]. Extending the kinetic model to explicitly include the energetics of GTP hydrolysis showed that the free energy released during hydrolysis did not contribute to producing mechanical work [66]. Shortly after, it was realised that, if the MT was constrained between two barriers, as would be the case for a kMT in the spindle, but still able to exchange subunits at the ends, the treadmilling could convert chemical free energy due to GTP hydrolysis into mechanical work [67, 68] (see also [69]). For an unobstructed MT, the change in length is given by

$$\frac{dl}{dt} = ck_{\text{on}} - k_{\text{off}}, \tag{2.1}$$

where $c$ is the concentration of tubulin subunits and the rates $k_{\text{on}}$ and $k_{\text{off}}$ subsume the individual polymerisation and depolymerisation rates at each end.

In the steady state, i.e. with constant length ($dl/dt = 0$),

$$k_{\text{off}}/k_{\text{on}} = c_c \tag{2.2}$$

where $c_c$ is the critical concentration of free subunits for steady state. If the MT is obstructed by a force $f$, the polymerisation rate is reduced so that (2.1) becomes

$$\frac{dl}{dt} = ck_{\text{on}}e^{-fd/k_BT} - k_{\text{off}}, \tag{2.3}$$

where $d$ is the subunit extension length of the polymer, and the critical concentra-

tion increases to

$$c_o(f) = c_c e^{fd/k_B T} \tag{2.4}$$

where $c_o(f)$ is the steady-state concentration for a force $f$ opposing MT elongation, due to the obstruction, and $d$ is subunit length. Rearranging,

$$f = \frac{k_B T}{d} \ln\left(\frac{c_o}{c_c}\right) = \frac{k_B T}{d} \ln\left(c_o \frac{k_{\text{on}}}{k_{\text{off}}}\right). \tag{2.5}$$

During MT shortening in anaphase, the ratio $k_{\text{on}}/k_{\text{off}} \approx 0.001\ \mu\text{M}^{-1}$, yielding a maximum pulling force of 32 pN [11].

On purely thermodynamic grounds, the free energy of GTP hydrolysis $\Delta G_{\text{GTP}}$ constrains the maximum pulling force. The difference in $\Delta G_{\text{GTP}}$ for GTP in free solution and bound in the MT lattice is 4 kcal/mol, or 26 pN nm/subunit, corresponding to a maximal force of around 43 pN (using 8/13 nm as the step distance, see §1.2.2) [70, 71].

During mitosis, the treadmilling of tubulin subunits is often called the *poleward flux* of tubulin. The rate of poleward flux and the degree to which it has an impact on segregation is subject to considerable variation among species. In *Xenopus* egg extracts poleward flux and chromosome motility have been observed to occur at the same rate (~2 μm/min) [72], although these are *meiotic* cells. In mitotic newt lung cells, by inhibiting disassembly at the kinetochore ends using taxol, the unaffected poleward flux due to depolymerisation at the centrosome ends was able to segregate chromosomes at a similar rate to control cells [73]. Mitosis also still proceeds efficiently in human cells when poleward flux is inhibited, although chromosome velocity is reduced 20% [74].

#### 2.1.3.3 Hill sleeve

In 1985, Hill proposed the first quantitative model for maintaining the attachment of a MT to a kinetochore during MT depolymerisation, including the effect of the viscous drag of the chromosome [75]. The Hill model envisions a close-fitting sleeve, around 40 nm long, wrapped around the end of a MT. A sleeve of this length could accommodate up to $M = 65$ tubulin subunits, and at some point in time $1 \leq n \leq M$ spaces are free. The MT end can be considered to be following a random walk in $n$. Calling the free energy of interaction with the sleeve per subunit $w$, the probability of taking steps increasing $n$ (withdrawing the MT) is modified by the Boltzmann factor $e^{-w/k_B T}$. This provides an effective force opposing the withdrawal of the MT. Hill's model predicts a maximal load force, for reasonable parameters, of ~ 17 pN.

#### 2.1.3.4 Pac-man model

Liu and Onuchic postulated a model where an electrostatic attraction exists between the ring and the MT [76]. The attraction is strongest at the point where PFs curl due to the widened diameter. This served to maintain the rings position at the tip of the MT. They combined this with MT depolymerisation and found the ring could remain attached and support forces of up to 1.5 pN before stalling. At the time of publication, no direct experimental data was available for comparison with this model. Furthermore, the electrostatic interaction between tubulin and Dam1 remains unquantified, and in vivo a Debye screening length of around 1 nm would exist, meaning only a very closely fitting interaction would effectively bind the Dam1 and tubulin together.

#### 2.1.3.5 Molecular-mechanical model

A coarse-grained molecular-mechanical model, representing tubulin monomers as spheres, based on an axial interaction that acts to curl PFs and a lateral interaction between PFs opposing curling, demonstrated that the energy released as lateral bonds broke and PFs curled was sufficient to drive the catastrophic depolymerisation of dynamic MTs. The model did not consider the possibility of driving cargo by harnessing this energy [77]. Following the measurement of the PF pushing force (see §2.1.2.1), the authors modified the model to investigate force production by MT depolymerisation and found that a powerstroke due to the conformational change of tubulin would be highly effective, resulting in a force of $\sim 75$ pN per tubulin subunit layer [78].

This model was later extended, after the Dam1 complex was found to form rings around MTs, to include an MT-encircling coupler [79]. Between this ring and the MT was hypothesised to be some unknown protein linkage, with the stiffness of the link and strength of binding being variable parameters. The links were assumed to bind directly to tubulins, and the ring could move by the exchange of bound tubulin sites. They concluded that weakly bound rings are energy efficient but not reliably attached to the MT, since they found the detachment force to $< 15$ pN, while strongly bound rings must walk by a so-called 'forced walk' mechanism. This invokes the powerstroke force generated by the elastic curling of PFs during depolymerisation to push the ring. Such a strongly bound ring shows negligible diffusion, in contrast to previous results [36], and would support forces beyond 40 pN. No direct comparison with experimental data was attempted.

#### 2.1.3.6 Molecular motors

Many MT-related motor proteins are involved in chromosome segregation [61, 80], with functional redundancy between different motors [81], although adenosine 5'-triphosphate (ATP)-depletion experiments have shown that they are not essential for isolated chromosome motility in vitro [14, 33].

Models of the overall chromosome segregation system usually include contributions from forces that are posited to be due to the action of molecular motors (see §2.1.3.1). In particular, Civelekoglu-Scholey et al. incorporate coupling between the kinetochore and MTs [15]. However, no model has focused solely on generation of forces at the kinetochore by molecular motors.

### 2.1.4 Differences between species

It is a remarkable fact that all life is built out of cells (as observed by R. Hooke in 1665 [82]). Consequently, cell division is an essential process for the continued existence of all species, and a critical part of that process is segregation of replicated chromosomes. However, striking mechanistic differences exist between various species, some of which will be briefly highlighted here.

In plant and lower invertebrate cells, poleward flux and minus end disassembly apparently plays a more significant role than in higher vertebrates [11]. In *Drosophila* the minus-end directed motor dynein is required for chromosome motility. However, dynein requires ATP hydrolysis to provide power and chromosome motion occurs in the protozoan *Tetrahymena* even without ATP [14]. Isolated chromosomes in vitro also do not require ATP or GTP for minus-end directed motion [33].

The Dam1 complex, implicated in kinetochore coupling to dMTs (see 2.1.2.2), has only been found in fungi [44], although some evidence suggests the Ska complex may play a similar role in humans [45]. However, the KMN network of protein complexes, which also plays a critical role in kinetochore-MT coupling, is highly conserved across eukaryotic species (from fungi to humans) [52].

Bacteria have only a single, circular chromosome and divide by binary fission, with chromosome segregation occurring through a mechanism that is apparently entirely different to eukaryotes. After replication of a special DNA site, *oriC*, one chromosome copy is translocated to the opposite cell pole while replication is still taking place [83]. A tubulin analog, FtsZ, is implicated in the formation of the contractile ring in cell division [84], rather than segregation of the genome. This FtsZ-based mechanism is also employed by chloroplasts [85]. Much less is known about chromosome segregation in bacteria than eukaryotes, although ParA has been shown to play a direct role in segregation [86, 87].

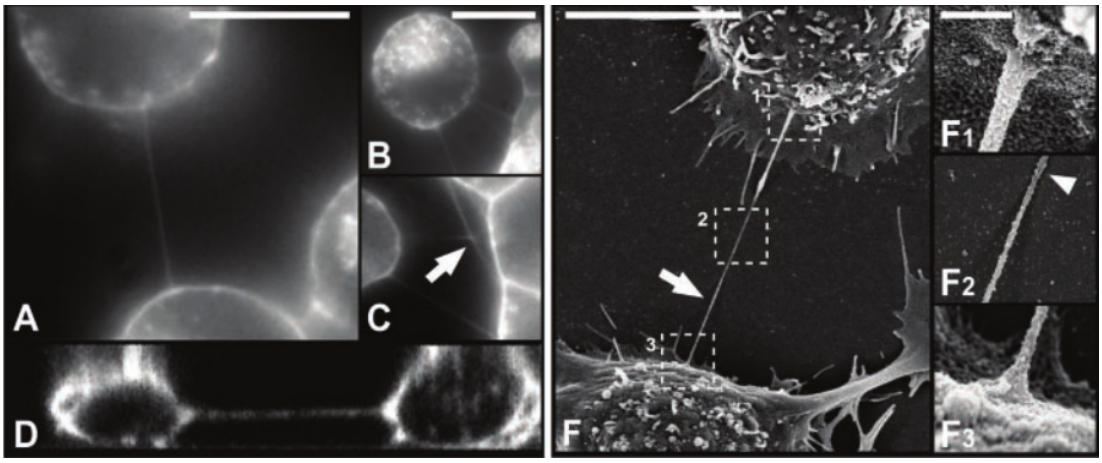


**Figure 2.3:** Three-dimensional fluorescence and scanning electron microscopy images of lipid tubes connecting cells in vivo. Figure taken from Rustom et al. [88].

## 2.2 Lipid tube mechanics

Observation of kidney cells using three-dimensional (3D) fluorescence microscopy reveals the presence of tubes, with diameter 50–200 nm and lengths up to several micrometres, connecting nearby cells. Over a 4 min period a tube was observed to grow to cover the 15 μm distance separating two cells, shown in Figure 2.3A-D. This observation puts the rate of extension of a tube to the order of 60 nm/s, with the caveat that this is based on one measurement and may be particular to this cell type. Strikingly, Rustom et al. also observed, by video microscopy, tubular or vesicular objects moving unidirectionally through the tubes at a mean speed of 25.9 ± 7.9 nm/s. Based on their fluorescent-labelling experiments, they propose that the tubes are formed by actin polymerisation, and material transport is mediated by an actin-based mechanism [88]. The tubes are known to be capable of transferring cargo including organelles, plasma membrane components and small cytoplasmic molecules, although it is possible that other cargo may also be transported by lipid tubes [89].

Lipid tubes have also been observed to connect, and facilitate communication, between immune cells [90, 91]. In particular, the HIV-1 virus can spread through tube interconnections between T-cells [92]. Prions can also travel between infected and non-infected cells through lipid tubes [93].

### 2.2.1 Theoretical modelling of vesicle-based tubes

Recent membrane elasticity models are based on the sum of square principal curvatures model of Canham [94] and the spontaneous curvature model of Helfrich [95]. In these models the free energy $F$ is the sum of contributions from

surface tension, pressure and curvature. The curvature energy term is based on the idea that the lipid bilayer has an intrinsic, spontaneous curvature $C_0$, where deviations of the mean curvature from $C_0$ increase the free energy quadratically. Minimisation of this free energy determines the shape of a membrane structure, such as a vesicle. This is accomplished variationally because $F$ is a functional, resulting in a shape equation which is the equilibrium condition. However, an extremum of $F$ does not necessarily imply a stable shape, and only stable shapes will manifest in experiment. Zhong-can and Helfrich derived a general shape equation and used it to calculate the second variation of $F$ to analyse the stability of extremal energy shapes [96]. If the second variation is positive definite then the shape is stable.

A simpler method for deriving a shape equation is to assume axisymmetry for the vesicles and write $F$ as an integral of a Lagrangian in terms of the arclength $s$ of the contour. A differential shape equation is then derived variationally through the Euler-Lagrange equations [97, 98]. This results in an identical shape equation for axisymmetric vesicles as the method of Zhong-can and Helfrich [99–101].

Several theoretical efforts have examined the shape and stability of tubes formed from vesicles, based on the Canham-Helfrich energy functional. Bukman et al. derived stability conditions for cylindrical vesicles as a model of a tube. They concluded that parameters obtained by experiment fall 'comfortably' within the range predicting stable cylindrical vesicles [102]. Božič et al. variationally minimised a Canham-Helfrich energy functional with an additional term for relative expansion of the membrane area, and obtained shapes of constant volume vesicles been strained axially at both ends. For a bending modulus of $\kappa \approx 10^{-19}$ J, they find tube radii in the 30–150 nm range, with forces $f$ = 25–5 pN. [103]. This analysis was extended, by a Ritz method, to allow the stability of the highly deformed shapes to be analysed. Comprehensively exploring the parameter space, Heinrich et al. were able to plot phase diagrams of the deformed vesicle shapes [104]. Derenyi et al. solved the membrane vesicle shape equation, as derived by Seifert et al. [98], for a portion of a vesicle being pulled by a point force and found that, although the force $f_0$ required for tube elongation is constant, during formation of the tube the force overshoots this value to $f_{\text{over}}$ [105]. Powers et al. independently came to the same conclusion [106], and furthermore observed the tube 'juts out' to larger radius near the tip of the tube. Smith et al. extended vesicle analysis to the surface adhered vesicle case [107], showing that the pulling force continues to increase as the tube is extended, due to the unbinding of the vesicle. Umeda et al. also numerically solved the Canham-Helfrich energy functional with an area expansion term, and observed a hysteresis effect with tube length changes [108].

### 2.2.2 Mechanical experiment producing tubes

Membrane tubes have been formed from giant vesicles using optical tweezers [109, 110], by the action of isolated kinesin motors [111, 112]. Tubes may also have been formed from surface-supported lipid bilayers [3] or surface-supported lipid bilayer stacks [2].

#### 2.2.2.1 Pulled from vesicles by external force

Pulling lipid tubes presents a novel experimental technique for investigating membrane properties. The force $f$ applied to a tube is inversely proportional to the radius of the tube $r_0$ [113], with the membrane rigidity $\kappa$ as the constant of proportionality (see also §5.1.1). Observing $r_0$ as a function of $f$ therefore allows the measurement of $\kappa$ [114].

Perhaps the first experimental production of lipid tubes was by the action of fluid shear stress [115, 116]. More recently, the force response of the tube has been measured over the course of pulling a tube. Raucher and Sheetz attached IgG-coated polystyrene beads to cell membranes, before pulling the bead away from the cell at constant velocity with optical tweezers. Initially the force was low but then rose to a constant value. The tube elongated at this constant force for several micrometres before exponentially increasing. At this point the bead escaped the trap [117]. The constant force elongation was attributed to the depletion of the a membrane reservoir, which serves to buffer the cell membrane surface tension. After the reservoir is depleted the force rises rapidly.

Koster et al. [109] pulled membrane tubes from giant vesicles by attaching a strepavidin-coated polystyrene bead to an immobilised biotinylated giant vesicle and moving the bead away from the vesicle, using optical tweezers, at 500 nm/s. They observed a sharp increase in force, up to a value $f_{\text{over}}$, associated with forming a tube, before a sudden drop back to a much smaller nonzero force $f_0$. Continuing to pull, this force remained constant until dropping back to zero as the tube ruptured. Monte Carlo simulations of the tube-pulling experiment were roughly consistent with the experimental data, although a detailed description of the simulation was not given. Using fluorescence microscopy, they also observed that the tube attached to the bead with a finite radius patch, ranging in size from near zero to 1500nm. In contrast with previous theoretical studies, which assumed a point-force, they found that the formation force $f_{\text{over}}$ was linearly dependent on patch radius.

Cuvelier et al. [110] also pulled membrane tubes from giant vesicles using optical tweezers to lengths of up to 250 μm. They compared the force profile obtained from vesicles held by micropipette aspiration with those from vesicles

adhered to a surface, and found that the force of tube extension continues to increase over many tens of micrometres, in stark contrast to the constant force observed with micropipette aspirated vesicles. They suggested the increase in force during elongation of the adhered vesicle tube could be explained by either by the free area consumption by the elongating tube causing a membrane tension increase, or by the induction of vesicle unbinding from the surface, as considered theoretically by Smith et al. [107].

A phenomenological theoretical approach was taken by Nowak and Chou to investigate the probability of tube extrusion for various parameter regimes. Their model incorporates the possibility that the bond between membrane and pulling device can break. According to their model tube formation is probable for a wide range of rates in both linear force ramp and constant pulling speed experiments [118].

#### 2.2.2.2 Formed by action of molecular motors

In addition to externally applied force, lipid tubes may also be pushed out from vesicles by molecular motors, perhaps also providing an insight into in vivo formation. Fygenson et al. encapsulated purified tubulin protein within vesicles. Although not strictly a motor, tubulin generates a pushing force during polymerisation [119]. Upon polymerisation of the encapsulated tubulin into microtubules, the vesicle become prolate and eventually produced tubular protrusions from each pole. The force sustained at the microtubule growing ends was calculated to increase to around 3 pN [120].

Roux et al. attached kinesin-coated polystyrene beads to giant vesicles. Kinesin is a protein motor that walks along microtubule tracks, consuming ATP, and can tow cargoes of up to 7–8 pN [121]. When incubated with ATP and microtubule tracks, the kinesins produced membrane tubes as well as complex tubular networks. However, directly attaching the kinesins to the vesicle did not produce tubes [122]. Koster et al. directly fixed kinesin motors to the lipids of giant vesicles and then put the vesicles in contact with immobilised microtubule tracks. When a threshold local concentration of motors is exceeded, membrane tubes are formed. Contrary to the findings of Roux et al., the kinesins did not need to be physically linked to each other, suggesting that merely accumulating into clusters is sufficient for cooperative formation of tubes [111]. The existence of a concentration threshold was further confirmed by Leduc et al. by complementing their assay with fluorescence intensity measurements of the motor binding sites. The growing tube tip was characterised by high fluorescence intensity indicating a large cluster of kinesin motors are present there [112].

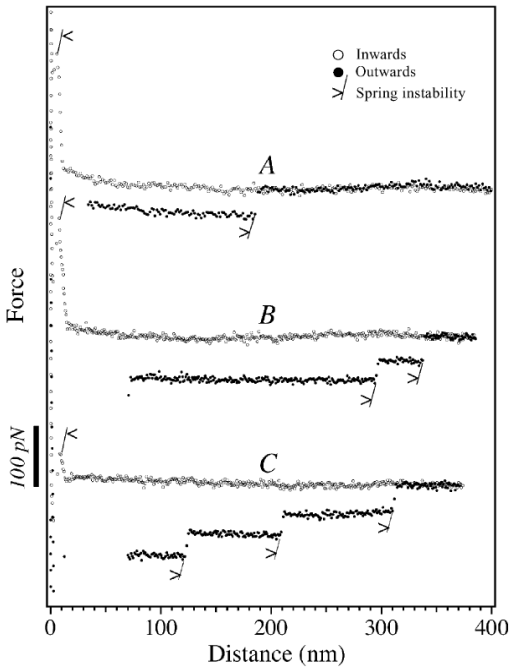


**Figure 2.4:** AFM force curves potentially showing pulled lipid bilayer tubes, produced by Maeda et al. with a bare silicon nitride probe. Figure taken from [2]. The surface was coated with multiple layers of lipid bilayers formed by solvent evaporation. This may explain why short-range forces are not resolved.

#### 2.2.2.3 Pulled from surface-supported lipid bilayers

Lipid tubes can also be pulled from lipid membranes formed on a solid surface. Maeda et al. formed multilamellar stacks of pure 1,2-dipalmitoyl-*sn*-glycero-3-phosphocholine (DPPC), pure 1,2-dimyristoyl-*sn*-glycero-3-phosphocholine (DMPC) and a mixture and used atomic force microscope (AFM) to pull tubes from the stack. During retraction, they observed several consecutive constant force regimes with approximately integral multiples of the final regime, shown in Figure 2.4. For DPPC layers, a single event had a force of 45.4 ± 3.5 pN, while for double and triple events the force was 81.6 ± 3.5 pN and 113 ± 35 pN. This was attributed to concentric tubes being formed [2]. A set of concentric tubes is effectively a multilamellar tube which may be forming due to the surface membrane being multilamellar.

In an effort to construct a more controlled system, Pera et al. formed single bilayers by vesicle deposition and fusion on muscovite mica. With both bare silicon nitride probes and mercapto ethanol-gold coated probes only one jump equivalent to bilayer thickness was observed when the probe approached the surface, leading to the conclusion that the probe was not also coated in bilayer [3] (bare silicon nitride probe data shown in Figure 2.5); if the opposite was true one might expect two jumps as either the two bilayers are penetrated individually

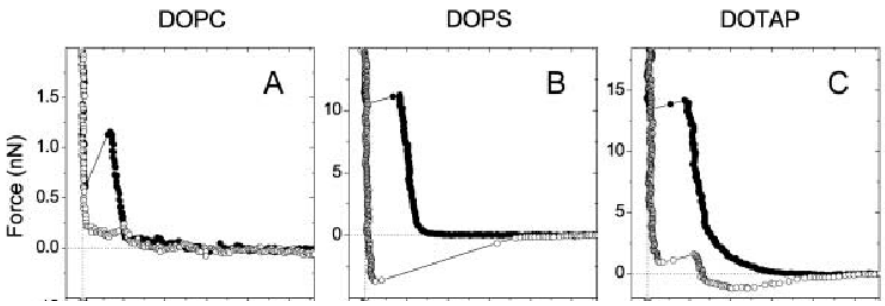


**Figure 2.5:** AFM force curves showing the short-range interaction with unilamellar vesicle deposited bilayers obtained by Pera et al. with a bare silicon nitride probe. The radius of curvature of the probe in the DOPC case was 45–50 nm. Figure taken from [3]. Pera et al. report that they occasionally observed a long-range interaction indicated by a step down in force, but did not show this data.

or, alternatively, the two bilayers fuse and then is penetrated, although this is certainly not clear. Bilayers are known to form on silicon nitride [123] and the lack of bilayer formation on the silicon nitride probe was attributed to the high curvature. With mercapto undecanol-gold coated probes two jumps occurred during approach, indicating that bilayers were formed on both the surface and the probe [3]. The retraction in these experiments were not reproducible and showed features including an adhesion force holding the probe to the surface, and a "weak long-range attraction" of less than 1 nN, which may indicate tube formation.

Membranes tubes have also been formed by using AFM probes on individual Chinese hamster ovary cells, malignant human brain tumour cells and human endothelial cells, and the elongation forces were found to be 28 ± 10 pN, 29 ± 9 pN and 29 ± 10 pN, respectively [124].

# 3

# Materials and methods

In this chapter the experimental procedures used to obtain the results of Chapter 7 are detailed. A brief introduction to the operating principles of atomic force microscope (AFM) is also included.

## 3.1 Atomic force microscope

An AFM is a sensitive instrument for measuring the deflections of a flexible cantilever responding to interactions with a sample [125]. The most common use for an AFM is for imaging the three-dimensional (3D) surface of a sample on a nanometre scale. In such a topography measurement, an Si (silicon) or $SiN_3$ (silicon nitride) cantilever with a sharp probe (radius of curvature $\sim$ 5–40 nm), is brought into 'contact' with the sample. Forces between the probe and surface results in a Hookean deflection of the cantilever (Figure 3.1). A laser focused on the reflective back of the cantilever is reflected onto a split photodiode. The voltage difference across the photodiode segments is proportionally related to the cantilever deflection (Figure 3.1). By using a feedback loop to maintain a constant deflection setpoint through adjustment of the $z$-position (normal to the sample surface) of the cantilever, with a piezoelectric actuator (piezo), while the probe is being raster scanned across the $x$- and $y$-axes (in the plane of the sample), the topography of the sample is mapped out by the $z$-position of the cantilever. This mode of operation is known as *contact mode* because the probe remains in contact with the surface at all times. With a quad-segment photodiode torsion in the cantilever can also be detected revealing the spatial distribution of friction in the sample, due to the torque exerted on the cantilever by friction forces as the probe is dragged across the surface.

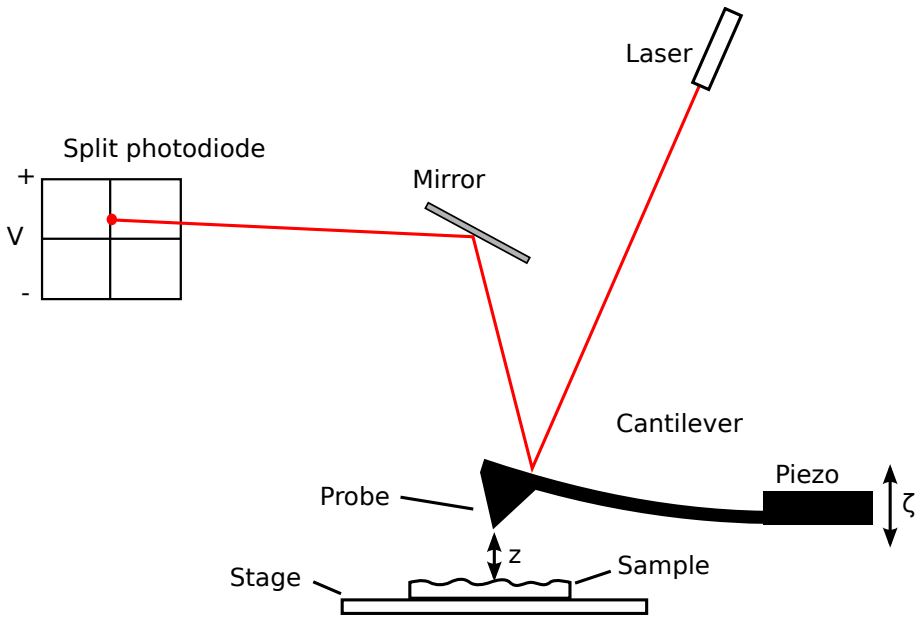


**Figure 3.1:** Standard atomic force microscope (AFM) imaging setup. A laser is used to detect the deflection of the cantilever by reflection onto a split photodiode. A feedback loop drives the piezoelectric element (piezo) holding the cantilever to maintain a constant probe-sample separation, while the probe is raster scanned in the $xy$-plane. The movement of the piezo required to maintain constant deflection corresponds to the topography of the sample. Note that, strictly, the movement of the piezo $\zeta$ is *not* equal to the probe-sample separation $z$. However, during imaging the feedback loop endeavours to maintain a constant deflection which *is* proportional to $z$, thus $\zeta$ provides the topography, unless the nature of the probe-sample interaction changes.

A popular alternative feedback mode is known as *tapping mode*. In this mode, the cantilever is oscillated at its resonance frequency, usually by a piezoelectric crystal mounted on the holder near the cantilever chip. As the probe is raster scanned over the surface, the feedback loop is used to maintain a constant oscillation amplitude. Whenever the probe to surface distance is reduced the oscillations are damped, again allowing the topography of the surface to be mapped. The key advantage of tapping mode over contact mode is that lateral forces are vastly reduced which allows imaging of soft samples, such as biological samples, without excessive damage.

Using very sharp probes can allow atomic resolution images to be captured [126]. However, the real advantage of the AFM comes from the flexibility allowed in environmental conditions, as it can operate in solutions [127], in vacuum [128], or at raised or cooled temperatures. Moreover, specialised cantilevers and probes allow the use of a wide range of properties as the feedback parameter including, but not limited to, magnetic force [129], electric force [130], electrochemical current [131], conductivity [132, 133] and temperature [134], enabling high spatial resolution images of these properties. Furthermore, the probe can be functionalised with ligands to 'image' the distribution of receptors on the sample [135].

## 3.2 Force measurements

In addition to raster scanning for imaging, the motion of the cantilever can be restricted to the $z$-axis, and the probe repeatedly brought into contact with the surface and then retracted again. The deflection, which is proportional to the force exerted by the cantilever by Hooke's law (see §3.2.1), is monitored throughout the cycle tracing out a *force curve*. Using a sample fixed to a surface it is possible to measure the $z$-axis component of a sample's elastic modulus from the force curves.

To measure forces in biological systems using an AFM it is necessary to establish the sample as the weakest link between the cantilever and a surface. A hard flat surface (e.g, mica or glass) is chosen as the support for the system to avoid coupling the stiffnesses of the surface and the system of interest. Furthermore, the stiffness of the cantilever must be chosen to be comparable to that of the system of interest, in order that useful measurements can be made.

In this mode it is also possible to perform force measurements on single molecules to measure, e.g. binding properties. For example, the probe may be functionalised at ultra-low density with a ligand and brought into close proximity with a layer of receptors on a surface, allowing the ligand and receptor bind. Upon retraction the deflection of the cantilever measures the force response of the

bond. Molecules may be fixed simply by van der Waals or electrostatic forces, or by, e.g., gold-thiol chemistry, streptavidin-biotin linking or PEG (polyethylene glycol) spacers. Analysis is complicated because the bond breaking 'reaction' is a non-equilibrium process due to the finite velocity of the probe. To fully probe the response of a bond to force in a single-molecule system it is necessary to vary the force loading rate, in a procedure called *dynamic force spectroscopy* [136]. This data can reveal the energy landscapes involved in dissociation and association [137, 138].

A similar experimental setup has been used to measure the energy landscapes of protein unfolding. Either by simple adsorption[1], or using flexible linking molecules, the protein is anchored between the surface and the probe. Retraction force curves generally show an elastic response, followed by a rapid drop in force as a domain of the protein loses integrity. From this point, the force-extension relationship is similar to that observed for polymeric molecules. Large multi-domain proteins, such as titin, display repeated occurrences of this pattern at surface-probe separations precise enough to identify the number of amino acids per domain [140]. Using the Jarzynski non-equilibrium fluctuation-dissipation relation [141], it is possible to relate the irreversible work done during the protein-unfolding pull to the equilibrium thermodynamic free-energy of unfolding [142, 143].

### 3.2.1 Hooke's law for cantilevers

The deflection $y$ of the end of a cantilever is proportional to the force $f$ applied at the same end, for small deflections. This can be shown by considering the equation of equilibrium for a beam for small deflections [144]

$$EI\frac{d^4y}{dx^4} = 0, \tag{3.1}$$

where $E$ is the Young's modulus of the beam material and $I$ is the area moment of inertia (the product $EI$ is called the flexural rigidity). The coordinate $x$ goes along the length of the beam between $x = 0$ and $x = L$. A cantilever is a beam held fast at one end ($x = 0$) and free at the other ($x = L$). Clearly at $x = 0$, the deflection $y$ is fixed at zero and the slope $dy/dx$ must also be zero. The bending moment is given by [144]

$$M = -EI\frac{d^2y}{dx^2}, \tag{3.2}$$

[1]Due to the very small contact area of the AFM probe, the pressure exerted by probe during compression is extremely large, on the order of several tens of gigapascals. It is thought that the pressure is sufficient to form covalent bonds between the probe and the sample [139].

and because the free end is not clamped the bending moment at $x = L$ must be zero. The shear force (the force applied to the beam in the $y$-direction) is [144]

$$f(x) = -EI\frac{d^3y}{dx^3}. \tag{3.3}$$

We are interested in the case where a shear force $+f$ (that is, directed upwards) is applied at the free end of the cantilever $x = L$. Therefore, the following boundary conditions apply

$$y\Big|_{x=0} = 0 \tag{3.4a}$$

$$\frac{dy}{dx}\Big|_{x=0} = 0 \tag{3.4b}$$

$$\frac{d^2y}{dx^2}\Big|_{x=L} = 0 \tag{3.4c}$$

$$\frac{d^3y}{dx^3}\Big|_{x=L} = -\frac{f}{EI}. \tag{3.4d}$$

After, integrating (3.1) four times we have

$$y(x) = c_1x^3 + c_2x^2 + c_3x + c_4, \tag{3.5}$$

where the $c_i$ are constants of integration. The boundary conditions (3.4) imply $c_3 = c_4 = 0$, $c_1 = -f/6EI$ and $c_2 = fL/2EI$. Putting these into (3.5) gives the equation of the deflection of the cantilever

$$y(x) = \frac{f}{6EI}(3Lx^2 - x^3). \tag{3.6}$$

In a typical AFM, the deflection is detected by a laser focused at the free end of the cantilever and we are interested in measuring the force $f$, hence the following equation is more useful

$$f = \frac{3EI}{L^3}z = kz, \tag{3.7}$$

where $k$ is the *spring constant*.

For a cantilever with rectangular cross-section of width $w$ and thickness $t$, the area moment $I$ is

$$I = 2w\int_0^{t/2} t'^2\,dt' = \frac{wt^3}{12}, \tag{3.8}$$

so the spring constant can be inferred from the cantilever geometry

$$k = \frac{Ewt^3}{4L^3}. \tag{3.9}$$

In practise, however it difficult to accurately measure the dimensions of AFM cantilevers and this derivation only applies to rectangular cantilevers, while soft, biologically-suitable cantilevers are often triangular, so spring constants are determined by other methods. The method used in this thesis, the thermal noise method, is described in §6.1.

## 3.3 Atomic force microscopy of surface-supported lipid bilayers

The experimental results reported in Chapter 7 were obtained on one of the following AFMs: Veeco Enviroscope with Nanoscope IV, Veeco Multimode V with Nanoscope V, or Veeco Catalyst with Nanoscope V (Veeco, Santa Barbara, CA, USA). Cantilever spring constants $k$ were measured using the thermal noise method [145] and the deflection sensitivity $\delta$ determined against a clean mica surface. The use of these parameters is discussed in §6.1.

### 3.3.1 Modification of AFM probe geometry

Standard AFM probes are generally designed to be as sharp as possible, i.e. having the smallest radius of curvature of the probe as possible. This allows high-resolution imaging where resolution is limited by the size of the probe. In force measurements a sharp probe is not always useful or desirable. In the case of pulling lipid tubes larger radii of probe curvature results in emphasised jumps in force magnitudes during tube formation (see Chapter 5). Therefore, a simple procedure was used (based on the procedure described in [146]) to fabricate blunt probes from standard sharp probes so that changes in the pulling force during the tube formation would be more measurable.

Standard V-shaped-cantilever silicon nitride probes (model NP, Veeco Probes, Santa Barbara, CA, USA), with nominal radius of curvature 20 nm, were ground down to fabricate blunt probes by the following procedure. A clean, unpolished diamond surface was used as a substrate. The probe was brought into contact with the diamond, and then the pushed into the surface a further 10 μm, which corresponds to a force of over 1 μN. The surface was scanned in contact mode over an area 40 μm by 40 μm at a line scan rate of 60 Hz for 15 min.

The degree of blunting was monitored by imaging a test grating containing an array of sharp spikes of ≤ 10 nm radius of curvature and spike angle of 30° (TGT1, NT-MDT Co., Moscow, Russia) before and after grinding. The test grating spikes have radius of curvature significantly less than the AFM probe; therefore

the image shows the 3D shape of the probe. These images are shown in Figure 7.4, and clearly demonstrate the efficacy of the procedure in generating blunt probes from standard sharp probes.

## 3.4 Solid-supported lipid bilayer preparation

All lipids used in this work were supplied by Avanti Polar Lipids Inc., Alabaster AL, USA. Lipids were supplied in powder form or dissolved in chloroform. If in powder, lipid was dissolved to 10 mg/ml in chloroform, aliquoted and stored at −20 °C.

A solid-supported lipid bilayer is a two-dimensional sheet of membrane that is formed, and supported by, a planar solid surface, and have numerous practical applications including immobilisation of proteins, acting as phantom cells, electrooptical biosensors [147]. Three methods are generally used to prepare a smooth bilayer on a surface. The Langmuir-Blodgett technique involves the use of a trough with a movable barrier to compress a dispersion of lipid molecules on the surface of a liquid. The surface requiring coating is then dipped in and out of the liquid, acquiring a bilayer in the process. The casting method simply requires the evaporation of a lipid-isopropanol solution directly on the surface, followed by hydration [148]. Finally, the lipid vesicles – closed, hollow spheres of bilayer, see Figure 1.4 – deposition method involves depositing a solution of vesicles onto the surface. Under favourable conditions, a fusion and rupture process causes the vesicles to spread across the surface forming a smooth bilayer [149]. The following results use vesicle deposition exclusively because the method is straightforward and reliable. The vesicle deposition protocol is followed from [150].

### 3.4.1 Preparation of unilamellar vesicles

The required quantity of lipid in chloroform was aliquoted into a glass vial, thoroughly dried under $N_2$ and left in a vacuum desiccator overnight. The lipid residue was resuspended in buffer and vortexed to dissolve. The lipids form multilamellar vesicles at this stage. The suspension was then subjected to a cycle of freezing in dry $CO_2$ supercooled with ethanol and thawing five times. To form unilamellar vesicles, the multilamellar vesicles were forced through a polycarbonate membrane of defined pore size. In the present experiments, vesicles were produced using a Liposofast Basic (Avestin Europe GmbH, Mannheim, Germany) which consists of a metal housing for a rubber gasket holding a polycarbonate membrane with screw threads at both ends for fitting syringes for forcing the suspension through the membrane. Membranes with 100 nm pore size were used.

The suspension was forced through 11 times resulting in a distribution of vesicle sizes close to the membrane pore size.

The buffer used for resuspension of lipids, referred to hereafter as HEPES buffer, was 150 mM NaCl, 3 mM $NaN_3$, 10 mM HEPES, 2 mM $CaCl_2$, and adjusted to pH 7.4. The $CaCl_2$ catalyses the rupture and fusion process [151].

### 3.4.2 Deposition of vesicles on surface

Immediately after preparation, approximately 30 μl of the unilamellar vesicle solution was deposited onto a freshly cleaved, clean mica surface. The sample is covered to ensure the droplet does not evaporate for 30 min; after this time a bilayer covering large areas of the surface has formed. Any excess vesicles were washed away by cycles of exchanging HEPES buffer solution. The sample is then ready for imaging and force measurements.

### 3.4.3 Force curve protocol

Prior to force measurements, the proper formation of the bilayer was checked by contact mode imaging. Only if a uniform and smooth bilayer of at least 3 μm by 3 μm was found, were force measurements taken. Poor formation of bilayer could be attributed to an unclean surface, solvents on the surface prior to deposition or old vesicle preparations.

The parameters defining the force curve cycles were as follows: the $z$-axis ramping velocity was set to 250 nm/s or 500 nm/s; the ramp size (the distance between fully retracted and fully extended) was typically 500 nm, or 1–2 μm when checking for very long tubes; the force trigger (during the extension phase, the ramp is halted when the force exceeds this threshold) was set to 20 nN – when using sharp probes, forces between 6–7 nN tended to penetrate the bilayer and contact the mica underneath; this was not observed at all up to 20 nN with blunt probes; once the force threshold was reached, the probe was held in contact with the surface for one second – this delay tended to increase the repeatability of the features observed in the force curve. During each cycle, at least 16384 data points were recorded, with 16-bit voltage resolution. For each given experiment and set of parameters, the cycle was repeated on the order of about 400 times.

Data was also obtained at ramp velocities of 5–100 nm/s and ≥ 1 μm/s. However, thermal drift[2] at the slow velocities made it difficult to discern genuine features, while at the higher velocities hydrodynamic drag on the cantilever was present, as well as exacerbated dissipation effects in the tube formation.

[2]Each component of the AFM, e.g., the laser, the mirrors, and the sample, tends to move slowly relative to each other at rates of 0.1–10 nm/s.

The experiments were also performed several times with standard sharp probes. However, the resulting data proved to be highly variable when compared to the data obtained with ground down, blunt probes. Presumably, this was because the curvature of the sharp probe was too high for stable bilayer attachment.

# 4

# Force transduction by the Dam1 ring

In §2.1 the models for mitotic microtubule (MT) force generation, in the context of anaphase, currently described in the literature were discussed. Most recent models include a combination of the following physical features:

1. the intrinsic diffusion of the Dam1 ring,
2. an effective powerstroke due to curling protofilaments (PFs),
3. steric confinement of the Dam1 ring by splayed out PFs at the MT tip,
4. an attractive potential between the Dam1 complex and the MT.

While experimental evidence for the diffusivity of a Dam1 ring on a MT is clear [39], it is difficult, based on current models, to discriminate the effects of a powerstroke or a potential. Dam1 rings have been shown to sustain tension on depolymerising MTs; velocity and runtime statistics are available [48, 49]. However, quantitative comparison of model predictions with this data is lacking for previous models. In this chapter two models are presented, both containing the common features #1 and #2, but each only incorporating either #3 or #4. The model provides predictions, using parameters obtained from experimental data, to determine which of #3 and #4, if any, is the dominant effect in vivo.

It is known that models of diffusion with broken symmetry require no powerstroke *per se* to generate motion. Rather, purely diffusive Brownian motion can be rectified if obstacles block diffusion in one direction after they have been crossed in the other direction. No instantaneous *physical* force is required; symmetry is

broken by the by unidirectional obstacles. The resultant rectified Brownian motion gives rise to a force in the thermodynamic sense. These models are often known as 'burnt bridge' models [152, 153], where the burning of a bridge activates an obstacle (included in the wider class of Brownian motors, see §B.2). For comparison with these models, 'bridge' units may be associated with MT subunits; they are 'burnt' by depolymerisation. It is therefore not necessarily true that #1 and #2 both must be present in a model of Dam1 force transduction, and the relative contribution of #2 is determined by fit to data.

In the following two distinct minimal models shall be described, both of which describe a functional Dam1-mediated force transduction system. Starting with a generalised model of how the Dam1 ring, moving diffusively, interacts with the MT depolymerisation process, different mechanisms determining the release of the ring are incorporated. In the *protofilament* model the splaying PFs at the depolymerising end physically prevent the ring from sliding off (Figure 4.5). In the *binding* model an attraction between the ring and MT provides an energy barrier preventing detachment (Figure 4.5). The two models are not necessarily mutually exclusive – a hybrid model, incorporating both contributions, may also apply although one of the constituent mechanisms will typically dominate. While it is straightforward to modify the analysis to include such hybrid models, their discussion has been postponed until §4.2.3 for clarity, since the goal is to differentiate the contributions of these two features. In common with previous models, other molecular components, e.g., microtubule-associated proteins (MAPs) and kinases [154, 155], that certainly play important additional roles *in vivo*, are also neglected. Nevertheless, some effects due to MAPs, e.g. increased depolymerisation rate, are automatically modelled by a parameter change.

## 4.1 Generalised depolymerisation model

The generally accepted mechanism of MT depolymerisation involves first the splaying of PFs, breaking open the MT lattice structure, referred to here as 'unzipping'. Secondly, curled PFs depolymermise by dissociation of tubulin subunits. In developing a general model of ring motion on a depolymerising microtubule (dMT), both a diffusive burnt bridge mechanism and a powerstroke must be included, such that their relative contributions may be determined. In this context, powerstroke is taken to mean a spontaneous energetic process causing an unzipping event. In this model, unzipping results in all PFs splaying and moves on the position of the last unbroken section of the MT lattice; a new section takes on the identity of last unbroken section when the previous one unzips (becoming separated, splayed PFs) (see Figure 4.1). It is assumed that cooperativity between

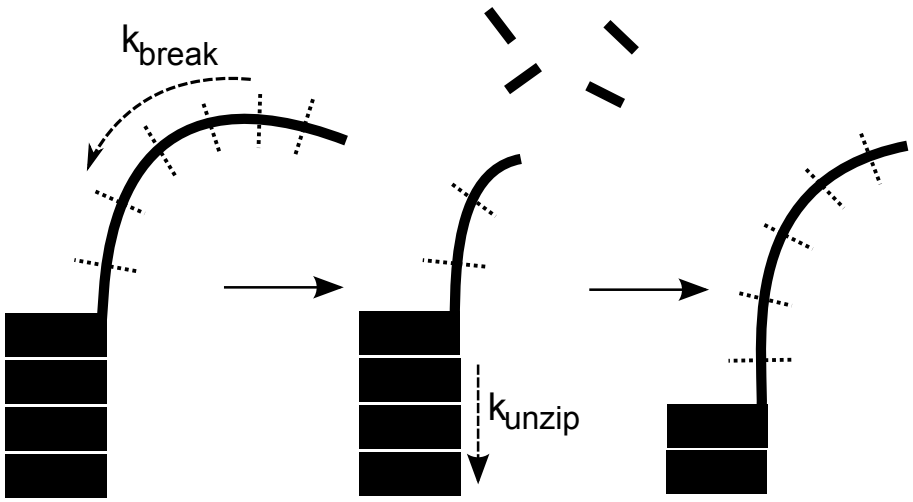


**Figure 4.1:** Two-rate microtubule (MT) depolymerisation process. Tubulin dimers depolymerise with rate $k_{\text{break}}$, while simultaneously the microtubule unzips with rate $k_{\text{unzip}}$.

adjacent PFs causes the MT to unzip by one full turn per unzipping event. The sequence of microscopic PF unzipping events (either by powerstroke or otherwise) gives rise to a well defined average velocity $v$ for the last fully intact MT section, irrespective of the sequence in which the neighboring PFs unzip, and the precise MT helicity. The powerstroke is assumed to occur even when the ring is very close to the MT end, and moves the ring the distance corresponding to one unzipping event. In this case, due to necessity of overcoming the opposing force due to the ring, the energy barrier present in the unzipping process is enlarged (see §4.1.2). Correspondingly, the powerstroke gives rise to a reduced depolymerisation velocity $v_{\text{ps}}$, whenever the ring has diffused to within a distance $\delta$ from the end. When the ring is further than $\delta$ from the end, it is assumed that there is no interaction between the ring and the tip PFs. In this case the depolymerisation velocity is denoted $v_{\text{bb}}$, and corresponds to the depolymerisation velocity of a bare MT where there is no Dam1 ring anywhere on the MT. No prior assumptions are made as to which contribution dominates, rather this is determined by fitting the parameters $v_{\text{bb}}$, $v_{\text{ps}}$ and $\delta$ to data for the variation of the Dam1 velocity with load [49].

The model involves a clear distinction between only two mechanisms and represents the simplest possible model capable of explaining this data. It can be biophysically motivated on the grounds that the Dam1 ring interacts with neighbouring tubulin and so the rate of PF unzippering at the MT end should depend on how close the Dam1 ring is to the end. This mechanism is discussed in the next section in terms of a putative energy landscape for the depolymerisation (unzipping) reaction. It would be unjustified to postulate the existence of any features

on this energy landscape beyond the minimum required to explain the data. This amounts to a model involving two (distinct) depolymerisation mechanisms.

### 4.1.1 Motion of Dam1 ring

The Dam1 ring complex is reported to be capable of axial movement with respect to the MT [39]. Therefore, the Dam1 ring is treated as a particle undergoing one-dimensional Brownian motion in a potential $V(x)$ (shown for two different models in Figure 4.5). The fully intact MT extends away from the depolymerising end for $x > 0$ and the point at which the MT lattice unravels is $x = 0$ (see Figure 4.5A). The following Fokker-Plank equation determines evolution of the probability density $\phi(x, t)$ for the ring's position relative to the (moving) end, as described in §B.3,

$$\frac{\partial \phi(x,t)}{\partial t} = D\frac{\partial}{\partial x}\left(\frac{\partial \phi(x,t)}{\partial x} + \frac{1}{k_B T}\frac{\partial V}{\partial x}\phi(x,t)\right), \tag{4.1}$$

where $D$ is the diffusion constant of the ring. This approach is appropriate providing the depolymerisation velocity $v$ of the MT is not too fast, otherwise we must instead treat this as a full moving boundary problem. Since the MT depolymerisation is here quasistatically slow with respect to the diffusive relaxation of the ring, we can neglect viscous drag force on the ring, except as discussed in §4.1.3.

In the following we assume the Dam1 ring is sufficiently stable that it can only dissociate by slipping off the tip, not by dismantling. For simplicity the analysis is restricted to continuous depolymerisation processes only and discounts the possibility of rescue and polymerization, although these may be important for the in vivo mechanism. Although it would be straightforward to include such processes by accounting for an extended runtime due to a stochastically-timed growth of the MT, they would distract from the central results of this chapter.

A force $-\partial V/\partial x$ appears in (4.1). This is the applied force $-f$ on the Dam1 ring on the MT ($x > 0$) since the ring must do work to move against this force. If $f$ is constant, or slowly varying, a steady state solution to (4.1) is established. Setting for the steady state

$$\frac{\partial \phi(x,t)}{\partial t} = 0 \tag{4.2}$$

we have from (4.1)

$$\frac{d\phi(x)}{dx} + \frac{f}{k_B T}\phi(x) = \text{constant}. \tag{4.3}$$

It is clear that as $x \to \infty$ we must have $\phi(x) \to 0$, therefore the constant is zero. Solving the simple differential equation (4.3) we find the probability distribution

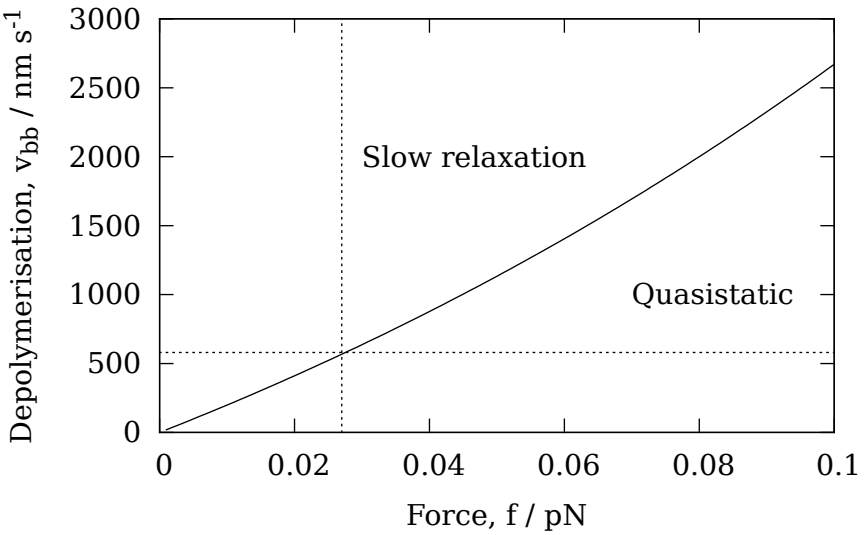


**Figure 4.2:** Range of load force $f$ and bare MT depolymerisation velocity $v_{bb}$ for which the quasistatic distribution assumption of (4.4) holds. The quasistatic assumption holds for parameter values below the line; above the line relaxation of the distribution $\phi$ is too slow. The horizontal dotted line is at $v_{bb} = 580$ nm/s, the value used in §4.3, for which $f_{min} \approx 0.03$ pN. Calulated for $T = 37$ °C and $D = 0.083 \pm 0.001$ μm$^2$/s [39].

$\phi(x)$ is of Boltzmann form

$$\phi(x) = \frac{f}{k_B T} \exp\left(-\frac{fx}{k_B T}\right), \tag{4.4}$$

where the ring typically explores a characteristic diffusion length $\lambda = k_B T/f$ from the MT end and positive values of $f$ here indicate loads pulling in the negative $x$ direction (towards the MT end). The necessary assumption for the establishment of a steady state is that the depolymerisation is *quasistatically slow*. This is appropriate provided the time for the MT to depolymerize the distance $\lambda$ is much larger than the relaxation time for a ring to diffuse this distance. This in turn requires $\lambda/v(f) \gg \lambda^2/D$. Substituting the characteristic diffusion length into this expression the yields the condition

$$\frac{f}{v(f)} \gg \frac{k_B T}{D}. \tag{4.5}$$

When this condition holds the distribution of the ring position is always close to the equilibrium probability distribution that it would have on an MT that was not depolymerising. This sets an upper bound on the depolymerisation velocity, or equivalently a lower bound on the load force, beyond which the theory is at best semiquantitative; for $v_{bb} = 580$ nm/s, the parameter value used in §4.3,

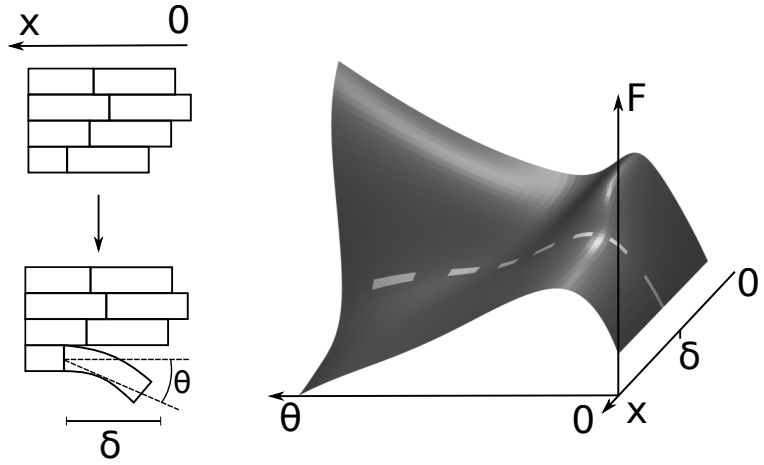


**Figure 4.3:** Schematic energy landscape underlying protofilament (PF) unzipping. The proposed free energy $F$ landscape of a tubulin dimer and Dam1 ring at the end of the microtubule (MT) is shown (right) as a function of the distance of the Dam1 ring from the MT end, $x$, and a reaction coordinate for the unzippering, the angle $\theta$ moved by the tubulin dimer (see diagram at left). The diagram is shown for illustrative purposes only and is not quantified in this work. Here $\theta = 0$ represents a dimer in a linear PF incorporated into a stable MT. During unzippering $\theta$ increases and the dimer moves out, ultimately forming the base of a splayed PF. The unzippering is an activated process with an energy barrier (the height of the ridge on the right) that is *different* for a powerstroke ($x < \delta$) and a burnt bridges reaction ($x > \delta$), leading to velocities $v_{\mathrm{ps}}$ and $v_{\mathrm{bb}}$ respectively. The energy landscape must have at least these basic features in order to give rise to the two depolymerisation rates consistent with the data.

the minimum force is approximately $f_{\mathrm{min}} \approx 0.03$ pN (see Figure 4.2). Under these conditions the average ring velocity is equivalent to the depolymerisation velocity of the MT; in the following $v$ will be referred to interchangeably thus.

### 4.1.2 Force dependent depolymerisation velocity

The powerstroke and burnt-bridge reactions can be thought of as arising from transitions over an energy barrier of the form shown in Figure 4.3, where the free energy $F$ of PF curling is shown as varying with protofilament angle $\theta$ and the distance of the Dam1 ring from the MT tip $x$. The figure shows only a putative schematic of the free energy of PF curling reaction, and should not be confused with the potential $V(x)$ within which the Dam1 ring diffuses.

PFs may produce a power stroke that pushes the ring with force $f_{\mathrm{pf}}$, estimated from experimental evidence to be $30 - 65$ pN [32]. This is the slope down the descending valley, diagonally right to left, in Figure 4.3. Provided that the load force $f \ll f_{\mathrm{pf}}$ the powerstroke will give rise to a depolymerisation velocity $v_{\mathrm{ps}}$ that is the rate at which the last intact dimer on the MT crosses the *highest* part of

the ridge-like energy barrier in Figure 4.3 ($x < \delta$). Since the estimate for $f_{\mathrm{pf}}$ is so much larger than any force considered here, it is reasonable to make the limited assumption that $v_{\mathrm{ps}}$ is constant for all experimentally measurable load forces of a few pN or less.

In addition the MT can also depolymerise when the Dam1 ring is further than a critical distance $\delta$ from the end of the MT; obviously the MT can depolymermise in the absence of Dam1. In this case the burnt-bridge reaction gives rise to a depolymerisation velocity $v_{\mathrm{bb}}$ that is the rate at which the last intact dimer on the MT crosses the *lower* part of the ridge-like energy barrier in Figure 4.3 ($x > \delta$). That the rate of MT unzippering is *retarded* when the Dam1 ring is near the MT end is a result of the fact that the velocity decreases as the load force is increased and the ring is more often closer to the MT end. Although it is not *necessary* to interpret the model in terms of the Dam1 ring physically occluding the unzipping of the tubulin dimers, this interpretation may not be unreasonable, particularly in view of the fact, as discussed in §4.3 that $\delta$ is found to be comparable with the axial length of the last intact ring of tubulin dimers.

The resultant velocity due to both mechanisms is the sum of the probability that the ring is close to the MT end $x < \delta$, multiplied by the powerstroke velocity, and the probability that it is far $x > \delta$, multiplied by the burnt-bridge velocity,

$$\begin{aligned} v &= v_{\mathrm{ps}}\left(1 - \int_{\delta}^{\infty} \phi(x)\,dx\right) + v_{\mathrm{bb}} \int_{\delta}^{\infty} \phi(x)\,dx \\ &= \left(v_{\mathrm{bb}} - v_{\mathrm{ps}}\right) \int_{\delta}^{\infty} \phi(x)\,dx + v_{\mathrm{ps}} \end{aligned} \tag{4.6}$$

The velocity follows from Eqs. (4.6) and (4.4)

$$v = (v_{\mathrm{bb}} - v_{\mathrm{ps}})e^{-f\delta/k_B T} + v_{\mathrm{ps}}, \tag{4.7}$$

The variation of this velocity with load is shown in Figure 4.9 for $v_{\mathrm{bb}} = 580$ nm/s [156], and the values $v_{\mathrm{ps}} = 55$ nm/s and $\delta = 14$ nm that correspond to the best fit to data [49]. Since a "burnt-bridges"-only model fails to fit the data sufficiently (i.e. $v_{\mathrm{ps}} > 0$) it suggests that a powerstroke plays a role in forced Dam1 motion. It should be noted that, although in the model $v \to v_{\mathrm{ps}}$ as $f \to \infty$ implying that depolymerisation is not stallable, it is not suggested that this is a physical feature of the system. Rather it is the consequence of the assumption that protofilaments are perfectly rigid and that the powerstroke reaction is asymptotically strong. The model would need modification for forces approaching $f_{\mathrm{pf}}$. As discussed later, PFs are estimated to require tens of pN to bend (for detailed calculations of PF rigidity estimates see [157]).

### 4.1.3 Drag

The effect of occlusion of the MT end by the Dam1 ring on depolymerisation velocity is given by (4.7). Although, for the parameters used later in this chapter, the effect is insignificant, it is possible to account for the viscous drag caused by moving a chromosome at constant velocity through the cytosol of a cell. In this case, the load force $f$ will have a component that is proportional to velocity

$$f(v) = \frac{1}{\mu}v + f_0, \tag{4.8}$$

where $f_0$ is the constant (external) load, and $f(v)$ is directed towards the chromosome. The constant $\mu$ is called the mobility, and is related to viscosity. For a sphere of radius $a$, Stokes' law may be used to derive $\mu$

$$\mu = \frac{1}{6\pi\eta a} \tag{4.9}$$

where $\eta$ is the viscosity and has units of dyn s cm$^{-2}$ or poise [158]. The mobility is also related to the diffusion constant $D$ by the Einstein relation $D = \mu k_B T$ (B.3). This relation is used here, resulting in the appearance of $D$ in the following equations.

To solve equations (4.7) and (4.8) self-consistently for $v$, consider the Dam1 ring to be diffusing on the MT, as in (4.1), with a reflecting (i.e. zero flux) boundary condition at the tip. At steady state, assuming the quasi-equilibrium condition $\lambda/v(f) \gg \lambda^2/D$ holds, we find the solution of (4.1) is as in (4.4), albeit with a velocity-dependent force

$$\phi(x) = \frac{f(v)}{k_B T} \exp\left(-\frac{f(v)}{k_B T}x\right). \tag{4.10}$$

Substituting (4.10) into (4.6)

$$\begin{aligned} v &= (v_{\text{bb}} - v_{\text{ps}}) \int_{\delta}^{\infty} \frac{f(v)}{k_B T} \exp\left(-\frac{f(v)}{k_B T}x\right) dx + v_{\text{ps}} \\ &= (v_{\text{bb}} - v_{\text{ps}}) \exp\left(-\frac{f(v)}{k_B T}\delta\right) + v_{\text{ps}}, \end{aligned} \tag{4.11}$$

and putting in (4.8)

$$\begin{aligned} v &= (v_{\text{bb}} - v_{\text{ps}}) \exp\left\{-\left(\frac{v}{\mu k_B T} + \frac{f_0}{k_B T}\right)\delta\right\} + v_{\text{ps}} \\ &= (v_{\text{bb}} - v_{\text{ps}}) \exp\left\{-\left(\frac{v}{D} + \frac{f_0}{k_B T}\right)\delta\right\} + v_{\text{ps}}. \end{aligned} \tag{4.12}$$

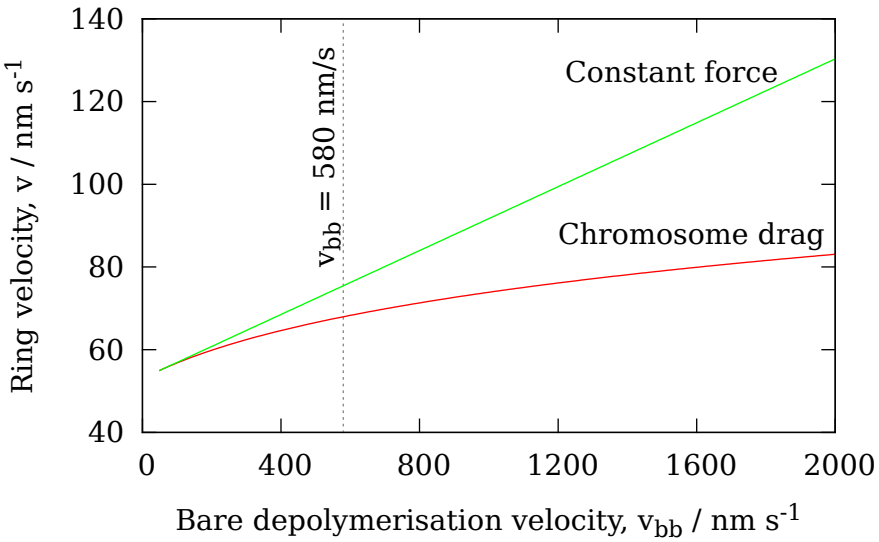


**Figure 4.4:** Ring velocity $v$ dependence on bare depolymerization velocity $v_{bb}$ of both models with constant load $f_0 = 1$ pN compared to velocity dependent chromosome drag $f(v) = v \cdot (k_B T/D_c) + f_0$. Under constant load, velocity increases linearly. With an additional chromosome drag ($D_c = 0.0004\ \mu m^2/s$ [13]) the total load increases proportionally to $v$ and consequently $v$ follows the form of the Lambert-$W$ function. The dotted line is at $v_{bb} = 580$ nm/s, the value used in §4.3. For this value, the drop in $v$ is only on the order of 10 nm/s.

Rearranging to collect $v$'s on left-hand side

$$(v - v_{ps}) \exp\left\{\frac{\delta}{D}(v - v_{ps})\right\} = \frac{\delta}{D}(v_{bb} - v_{ps}) \exp\left\{-\left(\frac{v_{ps}}{D} + \frac{f_0}{k_B T}\right)\delta\right\}. \tag{4.13}$$

Solving for $v$ using the Lambert-$W$ function [159],

$$v = \frac{D}{\delta} W\left[\frac{(v_{bb} - v_{ps})\delta}{D} \exp\left\{-\left(\frac{v_{ps}}{D} + \frac{f_0}{k_B T}\right)\delta\right\}\right] + v_{ps}. \tag{4.14}$$

A comparison of (4.14) and (4.7) is shown in Figure 4.4.

## 4.2 Two models for Dam1 ring retention

Building upon the result for ring velocity from §4.1, the minimal models are completed by considering under what conditions the Dam1 will be released from the MT. The two possibilities considered are described below and are shown in the diagrams of Figure 4.5. Each model is then used to calculate the mean time $\langle \tau \rangle$ the Dam1 ring will remain on a MT and transduce force[1]. This time is called the

[1]Recently it has been discovered that Dam1 oligomers can track the tip of dMTs without forming a ring [46, 160]. It seems unlikely that a protofilament model could operate without a

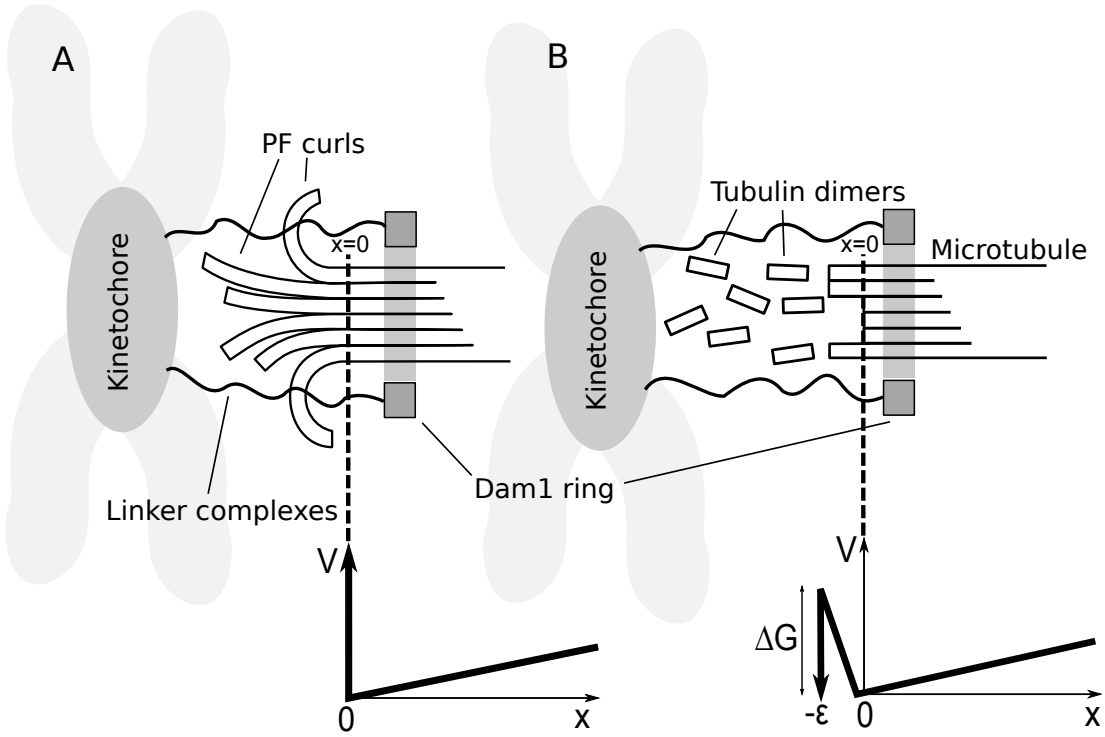


**Figure 4.5:** Two general classes of models of Dam1 ring-microtubule coupling. In both cases force is generated by rectifying Brownian motion, that is the ring diffuses to the right and the microtubule (MT) happens to unzip one segment or it is driven to the right by a powerstroke associated with unzipping. The dotted line denotes the point reached by MT unzipping ($x = 0$). ($A$) The ring is sterically confined to the MT by protofilaments (PFs) (protofilament model). The ring must be sufficiently tight that the PFs can confine it to the MT. ($B$) The ring is attractively bound to the MT surface with a free energy of binding $\Delta G_{\mathrm{Dam1}}$ (binding model). Below each model, the potential profile $V$ in which the ring diffuses is shown as a function of the distance $x$ of the ring from the MT end, and a dotted line indicates the connection between profile and model. The load force is the slope of $V(x)$ for $x > 0$. In ($A$) there is a large (infinite) energy barrier preventing the Dam1 ring moving to $x < 0$ whenever curled PFs are present. If the PFs completely depolymerize, leaving a 'blunt' end on the MT, this barrier disappears. In ($B$) the ring maintains only partial contact as it slides off the end of the MT ($-\epsilon < x < 0$), which results in a rise in energy until it finally loses contact and is lost forever for $x < -\epsilon$. The linker complexes are not modelled here but may be the Ndc80 complex [50]. See text for details.

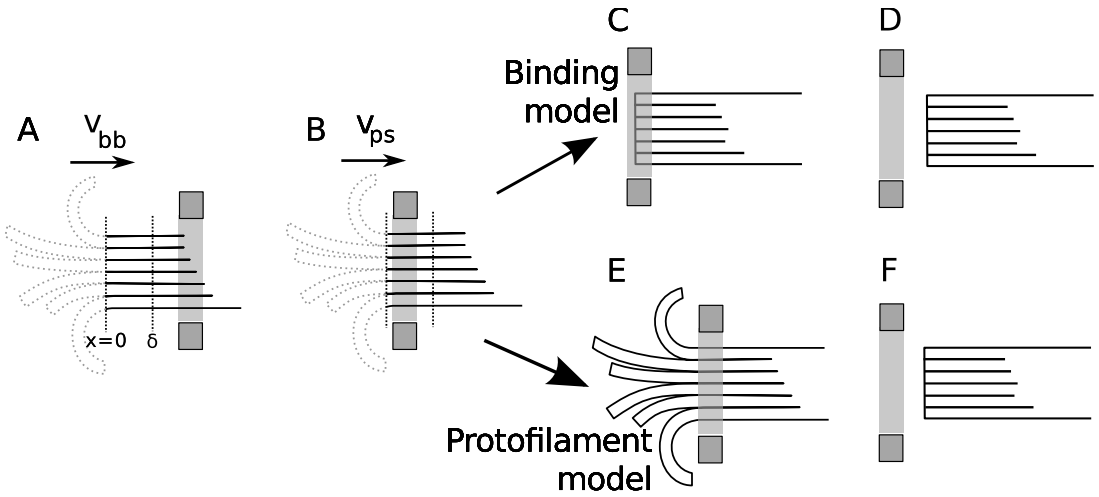


**Figure 4.6:** Various sketches of a ring on a microtubule (MT). (*A*) In this configuration the ring is further than $\delta$ from the tip of the MT, so the MT depolymerizes with velocity $v_{\mathrm{bb}}$. Unzipped protofilaments (PFs) are shown dotted as they do not affect depolymerization. (*B*) In some other configuration, the ring is closer to the tip than $\delta$, so the MT depolymerizes with velocity $v_{\mathrm{ps}}$. In (*C-F*) the detachment mechanisms are shown. This is either insensitive to protofilaments (PFs) (*C-D*; binding model) or sensitive to PFs (*E-F*; protofilament model). In (*C*) and (*E*) the ring has not yet escaped. In (*D*) and (*F*) the ring has escaped from the MT.

*runtime*. The connection between these models and the velocity model, previously described in §4.1.2, is sketched in Figure 4.6.

### 4.2.1 Binding model runtime

The binding model involves a ring diffusing on a MT according to (4.1), leading to a ring velocity as given in (4.7). However, in order to detach from the MT end the ring must overcome a linear potential imposed by the Dam1-MT binding energy $\Delta G_{\mathrm{Dam1}}$ as it slides off the end of the ring. In this respect it is similar to Hill's model [75]. Previous models invoked a $\Delta G_{\mathrm{Dam1}}$ that also determined the roughness of the energy landscape through "linkers" [79] whose existence is supported by binding studies [162]. Here we shall not make this assumption, rather $\Delta G_{\mathrm{Dam1}}$ could be due to less specific interactions without significant energy barriers between neighboring sites [38] but, importantly, can vary independently of the diffusion constant $D$. This, in turn, is fixed by the smoothness of the underlying energy landscape experienced by the ring as it diffuses along the MT (distinct from the energy landscape experienced by an unzippering PF shown in

full ring, however, it is not known to what extent, if at all, small oligomers contribute to force production, or whether the oligomeric form is dominant in vivo. Furthermore, it has been shown that 16-20 Dam1 complexes are present at the kinetochore during metaphase [161], enough to form the ring.

Figure 4.3). This model assumes that the splayed PFs play no role, either because they are transient (rapidly breaking) or otherwise interact negligibly with the ring as it slides off the end of the MT. Although clearly an extreme approximation it forms the natural opposite limit to the protofilament model discussed in the next section. Under a load force the ring is in the well of a tick-shaped potential with two linear domains (inset Figure 4.5). To move to the left it must partially unbind from the MT, to move to the right it must do work against the applied force. The potential gradients experienced by the Dam1 ring determine the forces $f$ (on the MT) and $-f_\epsilon$ (detaching from the MT)

$$-\frac{\partial V}{\partial x} = \begin{cases} f & x \geq 0 \\ -f_\epsilon = \dfrac{\Delta G_{\text{Dam1}}}{\epsilon} - f & -\epsilon \leq x \leq 0 \end{cases} \tag{4.15}$$

where $\epsilon$ is the unbinding region. If the ring is in the region $x < -\epsilon$ then it is lost, and if lost we assume it never returns, hence we have $V \to -\infty$ for $x < -\epsilon$.

Symmetry from electron microscopy [39] and copy number [161] experiments suggest 16 complexes are required to form the Dam1 ring. Cosedimentation assays of Dam1 complex binding to MTs suggest a dissociation constant $k_D \sim 0.2\,\mu\text{M}$ [36]. By a simple thermodynamic argument, we can use $k_D$ to estimate the binding energy of a Dam1 complex $\Delta G_{\text{Dam1}}$

$$\begin{aligned} k_D &= \frac{[\text{Dam1}][\text{MT}]}{[\text{MT-Dam1}]} \quad \text{(at equilibrium)} \\ &= e^{-\Delta G_{\text{Dam1}}/RT} \end{aligned} \tag{4.16}$$

under the common assumption that the activity coefficients of the molecules are close to unity [163] ($R = 8.314\,\text{J}\,\text{K}^{-1}\,\text{mol}^{-1}$ is the ideal gas constant). For the reported $k_D$, we find $\Delta G_{\text{Dam1}} = 15\,k_B T$. However, the total bond energy may not be additive and therefore thermodynamic free energies based on single complex Dam1-MT binding assays may not apply to the Dam1 ring.

The detachment of the ring can be cast as a classical Kramers escape problem [164], that is, the problem of calculating the mean escape time of a particle trapped in a metastable potential well (see §B.4). To solve (4.1) with the potential given by (4.15) we followed the method of Agudov and Malakhov [165, 166] for the exact solution of the escape time. Often one can use the approximations put forth by Kramers that amount to modelling the particle diffusing in a harmonic well at $x = a$ and escaping over a harmonic barrier of height $W$ at $x = b$. The escape time is then shown to be [164]

$$\langle \tau \rangle_{\text{Kramers}} \propto [V''(a)V''(b)]^{-\frac{1}{2}}\, e^{-W/k_B T} \tag{4.17}$$

where prime denotes differentiation with respect to $x$. Although, in the current model the potential barrier could be well modelled by a harmonic potential, the linear slope due to $f$ has only a small gradient. For this reason, the exact method of Agudov and Malakhov was employed.

Our goal is to find a time for the escape of the ring. In the Fokker-Planck equation formulation used here we cannot speak in terms of escape times for single rings; equation (4.1) describes the probability distribution of ring positions in an infinite ensemble of systems. Thus we shall calculate the mean time of escape of an ensemble of such rings. Let $Q(t)$ be the mass of escaped probability density $\phi$ at time $t$

$$Q(t) = \int_{-\infty}^{-\epsilon} \phi(x,t)\,dx. \tag{4.18}$$

Clearly, $Q(0) = 0$ by the initial condition and $Q(\infty) = 1$ as the potential is lowest for $x \ll -\epsilon$, i.e. the ring eventually crosses $x = -\epsilon$.

The relaxation time $\langle\tau\rangle$ of $Q$, a characteristic time involved in the establishment of the stationary distribution $\phi(x,\infty)$, and the mean time to release for the Dam1 ring, is defined as

$$\langle\tau\rangle = \frac{\int_0^\infty Q(\infty) - Q(t)\,dt}{Q(\infty) - Q(0)} \tag{4.19}$$

Unfortunately, equation (4.1) is difficult to solve for $\phi(x,t)$, and thus (4.19) cannot be evaluated. By using the Laplace transform, (4.1) is transformed into an ordinary differential equation that can be solved readily. Provided (4.19) can be rewritten in terms of the Laplace transform we will obtain $\langle\tau\rangle$.

Denoting the Laplace transform operation by $\mathcal{L}\{\cdot\}$, equation (4.18) can be re-written in the following manner. First, note that

$$\begin{aligned}\mathcal{L}\left\{\frac{Q(\infty) - Q(t)}{Q(\infty) - Q(0)}\right\} &= \int_0^\infty e^{-pt}\frac{Q(\infty) - Q(t)}{Q(\infty) - Q(0)}\,dt \\ &= \frac{Q(\infty)/p - \hat{Q}(p)}{Q(\infty) - Q(0)},\end{aligned} \tag{4.20}$$

where $\hat{Q}(p) = \mathcal{L}\{Q(t)\}$. Now, taking the limit as $p \to 0$

$$\begin{aligned}\lim_{p\to 0}\mathcal{L}\left\{\frac{Q(\infty) - Q(t)}{Q(\infty) - Q(0)}\right\} &= \frac{\int_0^\infty Q(\infty) - Q(t)\,dt}{Q(\infty) - Q(0)} \\ &= \lim_{p\to 0}\frac{Q(\infty)/p - \hat{Q}(p)}{Q(\infty) - Q(0)},\end{aligned} \tag{4.21}$$

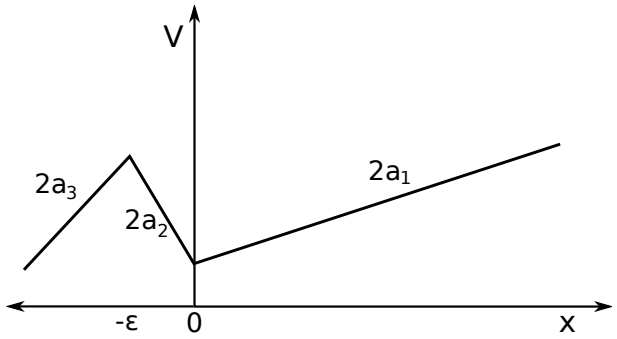


**Figure 4.7:** Sawtooth piecewise linear potential. The potential (4.15) corresponds to this potential for $x > -\epsilon$. The portion for $x < -\epsilon$ is set to be finite merely for analytical purposes; correspondence with (4.15) for all $x$ is recovered by taking the limit $a_3 \to -\infty$.

we regain (4.19). As previously noted, $Q(\infty) = 1$ and $Q(0) = 0$, thus

$$\langle \tau \rangle = \lim_{p \to 0} \frac{1 - p\hat{Q}(p)}{p}. \tag{4.22}$$

With the goal of solving (4.22) established, we begin by taking the Laplace transform in $t$ of (4.1) with conditions $\phi(x, 0) = \delta(x)$, although the precise form of this initial condition is unimportant, and $\phi(\pm\infty, t) = 0$

$$p\hat{\phi}(x, p) - \phi(x, 0) = D\frac{d}{dx}\left[\frac{d\hat{\phi}(x, p)}{dx} + \frac{1}{k_B T}\frac{dV(x)}{dx}\hat{\phi}(x, p)\right] \tag{4.23}$$

where constant $p$ is real and positive, $\delta(x)$ is the Dirac delta function and [167]

$$\hat{\phi}(x, p) = \int_0^\infty e^{-pt}\phi(x, t)\, dt. \tag{4.24}$$

At this point it is convenient to rescale the variables in order to simplify the manipulation: $C = 1/D$, $\rho = pC$, $u(x) = V(x)/k_B T$. Substituting the new variables and the initial condition into (4.23)

$$\frac{d^2\hat{\phi}(x)}{dx^2} + \frac{d}{dx}\left[\frac{du(x)}{dx}\hat{\phi}(x)\right] - \rho\hat{\phi}(x) = -C\delta(x), \tag{4.25}$$

where the argument $p$ has been dropped for clarity.

In order to find the solution to (4.22) for the model, we first must consider the

solution for a sawtooth potential (Figure 4.7) defined piecewise in three parts

$$u(x) = \begin{cases} -2a_1 x, & x \geq 0 \\ +2a_2 x, & -\epsilon \leq x \leq 0 \\ -2a_3 x, & x \leq -\epsilon. \end{cases} \tag{4.26}$$

The Laplace transformed equation (4.25) is an ordinary differential equation, and has the general piecewise solution

$$\hat{\phi}_1(x) = A_1 e^{\lambda_+ x} + B_1 e^{\lambda_- x}, \qquad x \geq 0 \tag{4.27a}$$

$$\hat{\phi}_2(x) = A_2 e^{\mu_+ x} + B_2 e^{\mu_- x}, \qquad -\epsilon \leq x \leq 0 \tag{4.27b}$$

$$\hat{\phi}_3(x) = A_3 e^{\gamma_+ x} + B_3 e^{\gamma_- x}, \qquad x \leq -\epsilon, \tag{4.27c}$$

with

$$\lambda_\pm = +a_1 \pm \sqrt{a_1^2 + \rho} \tag{4.28a}$$

$$\mu_\pm = -a_2 \pm \sqrt{a_2^2 + \rho} \tag{4.28b}$$

$$\gamma_\pm = +a_3 \pm \sqrt{a_3^2 + \rho}. \tag{4.28c}$$

After solving for this potential, we will be able to take the limit $a_3 \to -\infty$ and we will have the solution of (4.22) for the binding model potential shown in Figure 4.5.

We now specify sufficient conditions to determine the constants $A_1$, $A_2$, $A_3$, $B_1$, $B_2$, and $B_3$. To ensure finite total density we require that $\hat{\phi}_1(-\infty) = 0$ and $\phi_3(\infty) = 0$. This implies that $B_1 = A_3 = 0$ since $\lambda_- < 0$ and $\gamma_+ > 0$. Continuity between the three domains requires that

$$\hat{\phi}_1(0) = \hat{\phi}_2(0) \tag{4.29}$$

$$\hat{\phi}_2(\epsilon) = \hat{\phi}_3(\epsilon). \tag{4.30}$$

Integrating through the $\delta$ function initial condition at $x = 0$

$$\left.\frac{d\hat{\phi}_2}{dx}\right|_{x=0} + 2a_2\hat{\phi}_2(0) - \left.\frac{d\hat{\phi}_1}{dx}\right|_{x=0} + 2a_1\hat{\phi}_1(0) = C,$$

or

$$\left.\frac{d\hat{\phi}_2}{dx}\right|_{x=0} - \left.\frac{d\hat{\phi}_1}{dx}\right|_{x=0} = -2\hat{\phi}_1(0)(a_1 + a_2) + C, \tag{4.31}$$

and through $x = -\epsilon$

$$\left.\frac{d\hat{\phi}_3}{dx}\right|_{x=-\epsilon} - 2a_3\hat{\phi}_3(-\epsilon) - \left.\frac{d\hat{\phi}_2}{dx}\right|_{x=-\epsilon} - 2a_2\hat{\phi}_2(-\epsilon) = 0,$$

or

$$\left.\frac{d\hat{\phi}_3}{dx}\right|_{x=-\epsilon} - \left.\frac{d\hat{\phi}_2}{dx}\right|_{x=-\epsilon} = 2\hat{\phi}_2(-\epsilon)(a_2 + a_3). \tag{4.32}$$

Substituting (4.27) into (4.29)-(4.32) yields the following conditions

$$A_1 = A_2 + B_2 \tag{4.33a}$$
$$A_2 e^{-\mu_+\epsilon} + B_2 e^{-\mu_-\epsilon} = B_3 e^{-\gamma_-\epsilon} \tag{4.33b}$$
$$\mu_+ A_2 + \mu_- B_2 - \lambda_+ A_1 = -2A_1(a_1 + a_2) + C \tag{4.33c}$$
$$\gamma_- B_3 e^{-\gamma_-\epsilon} - \mu_+ A_2 e^{-\mu_+\epsilon} - \mu_- B_2 e^{-\mu_-\epsilon} = 2B_3 e^{-\gamma_-\epsilon}(a_2 + a_3). \tag{4.33d}$$

Solving the conditions (4.33) for the coefficients $A_1$, $A_2$, $B_2$, and $B_3$ is straightforward, but tedious, algebra. Substituting (4.33a) into (4.33c) eliminates $A_1$

$$A_2 = \frac{B_2(\mu_+ - \lambda_-) + C}{\lambda_- - \mu_-}, \tag{4.34}$$

and then substituting (4.34) into (4.33b) eliminates $A_2$

$$B_3 e^{-\gamma_-\epsilon} = \frac{B_2(\mu_+ - \lambda_-) + C}{\lambda_- - \mu_-} e^{-\mu_+\epsilon} + B_2 e^{-\mu_-\epsilon}. \tag{4.35}$$

Finally, substituting (4.35) and (4.34) into (4.33d) yields an expression for $B_2$

$$B_2\left[(\mu_- - \gamma_+)(\mu_+ - \lambda_-)e^{-\mu_+\epsilon} + (\mu_+ - \gamma_+)(\lambda_- - \mu_-)e^{-\mu_-\epsilon}\right] = C(\gamma_+ - \mu_-)e^{-\mu_+\epsilon}. \tag{4.36}$$

To find the mean escape time $\langle\tau\rangle$ for the ring we need to evaluate (4.22). Firstly

$$\begin{aligned} p\hat{Q} &= \int_{-\infty}^{-\epsilon} \hat{\phi}_3(x,p)ds \\ &= \frac{B_3 e^{-\gamma_-\epsilon}}{\gamma_-} && \text{by integrating (4.27c)} \\ &= \frac{1}{\gamma_-}\left[\frac{B_2(\mu_+ - \lambda_-) + C}{\lambda_- - \mu_-} e^{-\mu_+\epsilon} + B_2 e^{-\mu_-\epsilon}\right] && \text{using (4.35)} \\ &= \frac{2\gamma_+\sqrt{a_2^2 + \rho}}{(\gamma_+ - \mu_-)(\mu_+ - \lambda_-)e^{\mu_+\epsilon} + (\gamma_+ - \mu_+)(\lambda_- - \mu_-)e^{\mu_-\epsilon}} && (4.37) \end{aligned}$$

Then, noting that

$$\lim_{p\to 0} \rho = \lim_{p\to 0} pC = 0,$$

whence

$$\begin{aligned} \lim_{p\to 0} \lambda_+ &= 2a_1 & \lim_{p\to 0} \lambda_- &= 0 \\ \lim_{p\to 0} \mu_+ &= 0 & \lim_{p\to 0} \mu_- &= -2a_2 \\ \lim_{p\to 0} \gamma_+ &= 2a_3 & \lim_{p\to 0} \gamma_- &= 0, \end{aligned}$$

we can take the limit

$$\lim_{p\to 0} p\hat{Q} = \frac{4a_2a_3}{0 + 4a_2a_3} = 1. \tag{4.38}$$

Inspection of (4.22) with this result shows the expression is indeterminate. Therefore we must use L'Hôpital's rule in evaluating (4.22). Thus

$$\begin{aligned} \langle \tau \rangle &= \lim_{p\to 0} \frac{1 - p\hat{Q}}{p} \\ &= \lim_{p\to 0} \frac{d(1 - p\hat{Q})/dp}{d(p)/dp} \\ &= -\lim_{p\to 0} \frac{d(p\hat{Q})}{dp}. \end{aligned} \tag{4.39}$$

We use the quotient rule to evaluate the derivative

$$\begin{aligned} \frac{d(p\hat{Q})}{dp} &= \frac{d}{dp}\left(\frac{u}{v}\right) \\ &= \frac{v(du/dp) - u(dv/dp)}{v^2}, \end{aligned} \tag{4.40}$$

where

$$u = 2b_2\gamma_+ \tag{4.41}$$

$$v = (\gamma_+ - \mu_-)(\mu_+ - \lambda_-)e^{-\mu_-\epsilon} + (\gamma_+ - \mu_+)(\lambda_- - \mu_-)e^{-\mu_+\epsilon}, \tag{4.42}$$

and

$$\frac{du}{dp} = C\left(\frac{a_3 + b_3 + b_2}{b_3}\right) \tag{4.43}$$

$$\begin{aligned}\frac{dv}{dp} = \frac{C}{2}\Big\{&e^{-\mu_- \epsilon}\left[\left(\frac{1}{b_3} + \frac{1}{b_2}\right)(\mu_+ - \lambda_-) + (\gamma_+ - \mu_-)\left(\frac{1}{b_2} + \frac{1}{b_1}\right) + \frac{\epsilon}{b_2}(\gamma_+ - \mu_-)(\mu_+ - \lambda_-)\right] \\ &+e^{-\mu_+ \epsilon}\left[\left(\frac{1}{b_3} - \frac{1}{b_2}\right)(\lambda_- - \mu_-) + (\gamma_+ - \mu_+)\left(\frac{1}{b_2} - \frac{1}{b_1}\right) - \frac{\epsilon}{b_2}(\gamma_+ - \mu_+)(\lambda_- - \mu_-)\right]\Big\}.\end{aligned} \tag{4.44}$$

Finally, taking the limit as $p \to 0$ of (4.40)

$$\begin{aligned}\langle \tau \rangle &= C\left(\frac{1 - e^{2a_2\epsilon}}{4a_2^2} + \frac{1 - e^{2a_2\epsilon} + 2a_2\epsilon}{4a_2^2} + \frac{1 - e^{2a_2\epsilon}}{4a_1a_2} - \frac{e^{2a_2\epsilon}}{4a_1a_3}\right) \\ &= \frac{\epsilon^2}{D}\left(\frac{e^{2a_2\epsilon} - 1}{4a_2^2\epsilon^2} + \frac{e^{2a_2\epsilon} - 2a_2\epsilon - 1}{4a_2^2\epsilon^2} + \frac{e^{2a_2\epsilon} - 1}{4a_1a_2\epsilon^2} + \frac{e^{2a_2\epsilon}}{4a_1a_3\epsilon^2}\right)\end{aligned} \tag{4.45}$$

where the prefactor $\epsilon^2/D$ is introduced as a characteristic diffusion timescale. Finally, by taking $a_3 \to -\infty$ to introduce an absorbing boundary at $x = -\epsilon$ we have the desired mean time

$$\langle \tau \rangle = \frac{\epsilon^2}{D}\left(\frac{e^{2a_2\epsilon} - 2a_2\epsilon - 1}{4a_2^2\epsilon} + \frac{e^{2a_2\epsilon} - 1}{4a_1a_2\epsilon^2}\right) \tag{4.46}$$

After replacing $a_1$ and $a_2$ with the potentials defined in (4.15), the mean time the ring remains on the MT is

$$\langle \tau \rangle_{\text{binding}} = \frac{(k_BT)^2}{Df_\epsilon}\left(\frac{1 - \frac{f_\epsilon\epsilon}{k_BT} - e^{\frac{f_\epsilon\epsilon}{k_BT}}}{f_\epsilon} - \frac{1 - e^{\frac{f_\epsilon\epsilon}{k_BT}}}{f}\right). \tag{4.47}$$

### 4.2.2 Protofilament model runtime

The protofilament model involves a ring diffusing on a MT according to (4.1), leading to a depolymerisation velocity $v$ (4.7), identically to the binding model. In this model, however, the mechanism of ring detachment under load is different. To detach from the MT end the ring has to wait until all $n$ protofilaments have depolymerised, leaving a sufficiently blunt end to the MT for the ring to simply slide off (see Figure 4.5). In this case, the Dam1 ring is not required to overcome a Dam1-MT binding energy. Electron microscopy reveals that short, separated PFs splay outwards at the dMT end [25, 26] and it is quite plausible that these block the escape of the ring; the elastic energy required to straighten a curled PF [144] follows from measurements of their rigidity [7, 168] and is of the order of tens

of $k_BT$ per subunit, i.e. very large (see [157] for explicit calculations). Moreover, an estimate of the mean radius of curvature of the splayed PFs, from the electron micrographs [25, 26], is $\approx$ 18 nm. Given that the diameter of a straight MT is 25 nm, the frayed end of the MT might reasonably be expected to have a diameter of $\approx$ 60 nm. The outer diameter of the Dam1 ring is about 54 nm, the inner about 32 nm [36]; sufficiently long PFs may plausibly constrain a ring of this size on the MT.

The splayed PFs near the end of the MT are curved and, clearly, laterally separate. The depolymerisation, referred to here as unzipping, of the MT lattice (see Figure 4.5) is most accurately described as a process which transfers length from the polymerised MT into separated PFs. The unzipping is thought to be driven by the stored elastic energy in the $\alpha\beta$-tubulin units in the lattice [31]. Indeed, almost all of the free energy of hydrolysis of tubulin-bound GTP is stored in the lattice [70]. PFs possess a non-zero intrinsic curvature and when not constrained by lateral bonds they relax into a curved state.

In the protofilament model unzipping is modelled as a Poisson process with rate $k_{\text{unzip}}$. Each unzipping event extends every PF curl by a length $b$, leading to a depolymerisation velocity $v = bk_{\text{unzip}}$. In other words, the time between successive unzipping events $t_{\text{unzip}}$ is an exponential random variable, with probability density function

$$p_{\text{unzip}}(t) = k_{\text{unzip}} e^{-k_{\text{unzip}} t}, \tag{4.48}$$

and mean

$$\left\langle t_{\text{unzip}} \right\rangle = \frac{1}{k_{\text{unzip}}} = \frac{b}{v}. \tag{4.49}$$

The length $b$ might be the 8 nm of a tubulin dimer, if during each unzipping event the MT unzips by a complete turn of the MT helix. The results are nevertheless general for a different $b$.

The motion of the ring in this model follows (4.4). When the ring is within a short length $\delta$ of the MT end unzipping is inhibited – this gives rise to the two different rates for depolymerisation $v_{\text{bb}}$ and $v_{\text{ps}}$. The resultant velocity $v$ is a decreasing function for increasing load force $f$, according to (4.7). As a consequence $\left\langle t_{\text{unzip}} \right\rangle$ increases under load. Detachment occurs when all PF curl lengths reach zero[2]. From (4.4), the characteristic distance of the ring from the tip is $\lambda = k_BT/f$. The characteristic time for the ring to diffuse this length and escape is $t_{\text{fp}} = \lambda^2/D$ which is much less than $\left\langle t_{\text{unzip}} \right\rangle$ for typical parameters whenever $f > 0.15$ pN (see §4.2.2.1). Thus we make the reasonable assumption that the ring

[2]Extensions of the model to the case of loosely-fitting rings is straightforward, involving attachment whenever the PF curls exceed some finite length $L$. The results are qualitatively insensitive to this modification, provided the ring rarely detaches at low force. Furthermore, for such rings the molecular length $b$ becomes irrelevant as the characteristic timescale is $L/v$.

disengages from the MT extremely rapidly as soon as all curled PFs reach zero length.

Tubulin subunits on the splayed PFs are assumed to break independently according to a Poisson process with rate $k_{\text{break}}$. The depolymerisation of PFs then follows from the loss of all PF material beyond the break, as in previous computational models [169]. A PF curl reaches zero length if the axial bond nearest to the unzipping point breaks, see Figure 4.5. Under the assumption that the ring may only detach whenever PF curls are zero length, only this bond is actually relevant. Since breaking is a Poisson process with rate $k_{\text{break}}$, the waiting time $t_{\text{pf,i}}$ for PF curl $i$ to break off completely is an exponential random variable with distribution

$$P_{pf,i}(t) = 1 - e^{-k_{\text{break}}t}. \tag{4.50}$$

The waiting time for all $n$ PF curls breaking $t_{\text{pf}}$ is equal to that for the PF curl which takes the longest time to break. In other words,

$$t_{\text{pf}} = \max_i t_{\text{pf,i}}. \tag{4.51}$$

The probability distribution function for this time is the probability that $n$ identically distributed PFs break in a time less than $t$,

$$P_{\text{pf}}(t) = (1 - e^{-k_{\text{break}}t})^n, \tag{4.52}$$

and the mean wait time can be obtained by considering the order statistics [170, 171] (see §A.3)

$$\left\langle t_{\text{pf}} \right\rangle = \sum_{i=1}^{n} \frac{\left\langle t_{\text{pf,i}} \right\rangle}{n - i + 1} = \frac{H_n}{k_{\text{break}}}, \tag{4.53}$$

where $H_n = \sum_{i=1}^{n} i^{-1}$ is the $n^{\text{th}}$ harmonic number [172], roughly $\log n$ for $n \gg 1$, and $\langle \cdot \rangle$ denotes the ensemble average. Provided that no unzipping events take place during the time $t_{\text{pf}}$, all the PFs lengths go to zero, the Dam1 ring will no longer be secured to the MT end and will detach. If, on the other hand, the MT unzips during this waiting time then the PFs extend (from their base), effectively restarting the waiting process[3]

In this model, the mean runtime $\langle \tau \rangle$ is the time taken for the curled PFs to all depolymerise completely, thus freeing the ring, while the MT is simultaneously undergoing stochastic unzipping events. The runtime $\langle \tau \rangle$ can be found by counting the number of unzipping events $N$ that occur before the PFs all successfully break and the Dam1 ring can disengage. If we let $P_{\text{detach}}$ be the probability that

[3]Successive waiting times are Markovian so it does not matter at precisely what time unzipping occurs because the subsequent waiting time will have exactly the same distribution [173].

the MT unzips in a time $t_{\text{unzip}} > t_{\text{pf}}$, i.e. the ring detaches, then the probability of $N$ unzippings occurring before ring release is clearly

$$P_{\text{unzip}}(N) = (P_{\text{detach}})^N (1 - P_{\text{detach}}). \tag{4.54}$$

Therefore, $N$ is geometrically distributed and hence has mean $\langle N \rangle = 1/P_{\text{detach}}$ [173] with $P_{\text{detach}}$ the probability that the curled PFs depolymerize completely before the next unzipping event. Thus

$$\langle \tau \rangle = \left\langle t_{\text{unzip}} \right\rangle \langle N \rangle = \frac{\left\langle t_{\text{unzip}} \right\rangle}{P_{\text{detach}}} = \frac{1}{k_{\text{unzip}} P_{\text{detach}}}. \tag{4.55}$$

We may calculate the probability the ring detaches $P_{\text{detach}}$ as the probability that $t_{\text{pf}} < t_{\text{unzip}}$, using the probability density functions (4.48) and $p_{\text{pf}}(t) = dP_{\text{pf}}/dt$

$$P_{\text{detach}} = \int_0^\infty \int_0^t p_{\text{unzip}}(t)\, p_{\text{pf}}(t')\, dt'\, dt. \tag{4.56}$$

Evaluating firstly the integral in $t'$, and then substituting (4.48) and (4.52)

$$\begin{aligned} P_{\text{detach}} &= \int_0^\infty P_{\text{pf}}(t)\, p_{\text{unzip}}(t)\, dt \\ &= \int_0^\infty \left(1 - e^{-k_{\text{break}} t}\right)^n k_{\text{unzip}} e^{-k_{\text{unzip}} t}\, dt. \end{aligned} \tag{4.57}$$

Binomially expanding the integrand

$$\begin{aligned} P_{\text{detach}} &= \int_0^\infty \sum_{j=0}^{n} \left[ \binom{n}{j} (-1)^j e^{-j k_{\text{break}} t} \right] k_{\text{unzip}} e^{-k_{\text{unzip}} t}\, dt \\ &= k_{\text{unzip}} \int_0^\infty \sum_{j=0}^{n} \binom{n}{j} (-1)^j e^{-(j k_{\text{break}} + k_{\text{unzip}}) t}\, dt, \end{aligned} \tag{4.58}$$

where the binonmial coefficient is defined as

$$\binom{n}{j} = \frac{n!}{j!(n-j)!}. \tag{4.59}$$

Swapping the order of summation and integration

$$\begin{aligned} P_{\text{detach}} &= k_{\text{unzip}} \sum_{j=0}^{n} \binom{n}{j} (-1)^j \int_0^\infty e^{-(j k_{\text{break}} + k_{\text{unzip}}) t}\, dt \\ &= k_{\text{unzip}} \sum_{j=0}^{n} \binom{j-n+1}{j} \int_0^\infty e^{-(j k_{\text{break}} + k_{\text{unzip}}) t}\, dt, \end{aligned} \tag{4.60}$$

where an identity from Appendix A.2 has been used in the last line. Integrating (4.60) term-by-term we find the probability of ring detachment before the next unzipping event

$$P_{\text{detach}} = k_{\text{unzip}} \sum_{j=0}^{n} \binom{j-n+1}{j} \left(jk_{\text{break}} + k_{\text{unzip}}\right)^{-1}. \tag{4.61}$$

After substituting back into (4.55) we obtain the mean runtime of the ring

$$\langle \tau \rangle_{\text{PF}} = \frac{1}{(k_{\text{unzip}})^2} \left[ \sum_{j=0}^{n} \binom{j-n+1}{j} \frac{1}{jk_{\text{break}} + k_{\text{unzip}}} \right]^{-1}. \tag{4.62}$$

#### 4.2.2.1 First passage time

As noted in §4.2.2, (4.55) holds on condition that the ring diffuses to the MT end before the next unzipping event. This amounts to an assumption that the distribution of ring position is quasi-static, that is, it reaches an equilibrium well before the next unzipping event. The average distance of the ring from the tip is

$$\lambda = \frac{k_B T}{f}$$

and the characteristic time to diffuse this length is $t_D = \lambda^2/D$. For the assumption that the distribution of the ring position is quasi-static to hold we require $t_D \ll t_{\text{unzip}}$, or equivalently

$$f \gg k_B T \sqrt{\frac{k_{\text{unzip}}}{D}} = f_{\text{min}} \tag{4.63}$$

If this condition is met then the probability that the ring does *not* reach the tip before further unzipping takes place is negligible (for $v_{\text{bb}} = 580$ nm/s the condition is $f \geq 0.15$ pN). Otherwise, we must include the probability that the time it takes the ring to first reach the tip $t_{\text{fp}}$ satisfies the condition $t_{\text{fp}} < t_{\text{unzip}}$, for which detachment will occur. This probability can be calculated using the concept of first passage processes [174]. The probability distribution $p_\infty$ of the position of a particle (e.g., a Dam1 ring) after diffusing freely for a time $t$ on a one-dimensional track extending to infinity in both directions, is Gaussian

$$p_\infty = \frac{1}{\sqrt{4\pi D t}} e^{-(x-x_0)^2/4Dt}. \tag{4.64}$$

where $x_0$ is the initial position of the particle. Here, we are interested in the motion of a particle near the end of a MT, which we can consider as semi-infinite, i.e. $x \in [0, \infty]$. To account for the absorbing boundary at $x = 0$, we use the method

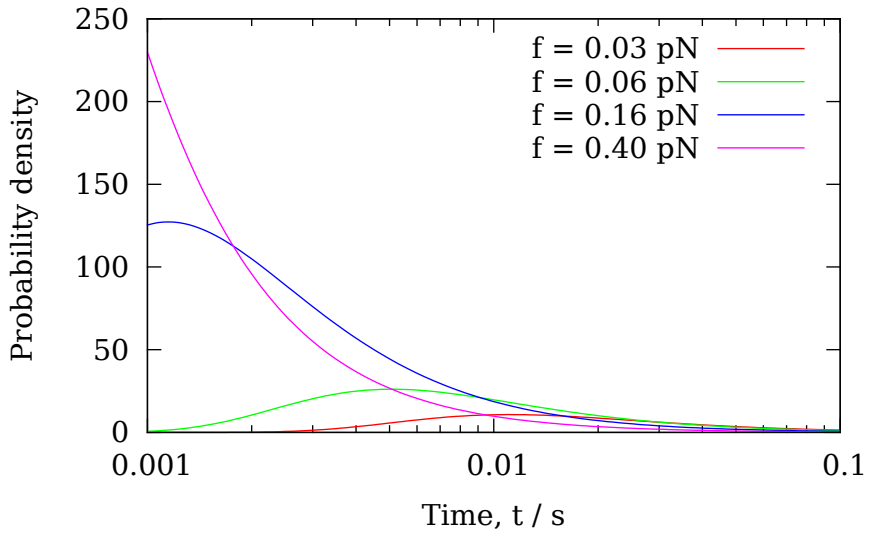


**Figure 4.8:** Probability distribution of the first passage time for the ring to escape when protofilaments have fully depolymerised for a range of forces. For $f > 0.15$ pN the time becomes negligible.

of images, by subtracting a Gaussian distribution for a mirror particle, initially at $x = -x_0$

$$p_0 = \frac{1}{\sqrt{4\pi Dt}}\left[e^{-(x-x_0)^2/4Dt} - e^{-(x+x_0)^2/4Dt}\right] \tag{4.65}$$

The first passage probability to the absorbing boundary $x = 0$ is the flux of probabilty distribution across that point

$$t_{\text{fp}} = D\frac{\partial p_0}{\partial x}\bigg|_{x=0} \tag{4.66}$$

Hence, for a particle initially at $\lambda$, the probability distribution of the first passage time is [174]

$$\begin{aligned} t_{\text{fp}}(t) &= D\frac{\partial}{\partial x}\left\{\frac{1}{\sqrt{4\pi Dt}}\left[e^{-(x-\lambda)^2/4Dt} - e^{-(x+\lambda)^2/4Dt}\right]\right\} \\ &= \frac{\lambda}{\sqrt{4\pi Dt^3}}e^{-\lambda^2/4Dt} \qquad \text{for } t \text{ large} \end{aligned} \tag{4.67}$$

The probability distribution of first passage time is shown in Figure 4.8 for a range of forces.

The probability the particle reaches the end before the protofilaments grow is

then [174]

$$P_{\mathrm{fp}}(t_{\mathrm{unzip}}) = \int_0^{t_{\mathrm{unzip}}} t_{\mathrm{fp}}(t)\,dt$$
$$= 1 - \mathrm{erf}\left(\frac{\lambda}{\sqrt{4Dt_{\mathrm{unzip}}}}\right). \tag{4.68}$$

Dividing (4.55) by (4.68), we have the mean residence time of a ring on a shrinking MT

$$\langle\tau\rangle = \frac{\left\langle t_{\mathrm{unzip}}\right\rangle}{P_{\mathrm{detach}}P_{\mathrm{fp}}(\left\langle t_{\mathrm{unzip}}\right\rangle)}, \tag{4.69}$$

where $P_{\mathrm{detach}}$ is the probability of detachment during a step as in (4.57).

### 4.2.3 Hybrid models

The protofilament and binding models present the two extremes of a minimal model of Dam1-ring force transduction. The protofilament model incorporates a steric confinement of the ring by splayed PFs (feature #3) but no attractive binding of the Dam1 complex to the MT (feature #4), while on the other hand the binding model contains only binding and ignores PFs altogether. The purpose of expounding such extreme models is to emphasise the differences between these features and aid in the development of discriminatory protocols. Nevertheless, if the features #1 through #4 described at the beginning of this chapter are indeed accurate, it is probably true that in vivo all features play some role to a lesser or greater degree. Therefore, it is worthwhile briefly considering a model that is a hybrid of the protofilament and binding models. Here two possible hybrid models are proposed, and briefly compared with the minimal models.

#### 4.2.3.1 Protofilament model with binding

The protofilament model may be very simply extended by including a binding attraction between the Dam1 ring and the MT, instead of allowing the ring to detach freely. Once all PFs have broken to zero[4] – taking, on average, $\langle\tau\rangle_{\mathrm{PF}}$, exactly as in (4.62) – a further time is incurred while waiting for the ring to escape the binding potential barrier. This additional time is exactly that of (4.47), which we denote $\langle\tau\rangle_{\mathrm{binding}}$. However, the ring can only escape in this scenario if the MT

[4]Or, indeed, some finite length $l$. See §4.2.2

does not unzip during $\langle\tau\rangle_{\text{binding}}$. Thus, the solution for this hybrid model is

$$\begin{aligned}\langle\tau\rangle^{(1)}_{\text{hybrid}} &= \langle\tau\rangle_{\text{binding}} + \frac{\langle\tau\rangle_{\text{PF}}}{N} \\ &= \langle\tau\rangle_{\text{binding}} + \langle\tau\rangle_{\text{PF}} \Big/ \int_0^{\langle\tau\rangle_{\text{binding}}} p_{\text{unzip}}(t)\,dt \\ &= \langle\tau\rangle_{\text{binding}} + \langle\tau\rangle_{\text{PF}}(1 - e^{-k_{\text{unzip}}\langle\tau\rangle_{\text{binding}}})^{-1},\end{aligned} \tag{4.70}$$

where $N^{-1}$ is the mean number of times that $t_{\text{unzip}} < \langle\tau\rangle_{\text{binding}}$; the number being geometrically distributed. Clearly, if the binding attraction is strong, a force transduction system operating in this manner would be extremely resilient to ring escape.

#### 4.2.3.2 Flexible protofilaments

Alternatively, the energy barrier the ring must overcome to escape the MT might be considered as originating in some compliance of the PFs. Although, it was previously mentioned that PFs are thought to be rigid on the tens of pN scale (§4.2.2), the rigidity of a PF has not been measured directly, but instead inferred from measurements of MT lattice as a whole. Using the theory of elasticity [144] and a rigidity measurement of a specific structure – e.g., a MT – it is possible to obtain the Young's modulus of the material of the structure [157]. The modulus may then be used to calculate the rigidity of any other structure, e.g., a PF. However, implicit in these calculations is the assumption that the material is homogeneous and isotropic, which may not be the case for MTs. It may be that certain interactions between neighbouring tubulin subunits in adjacent PFs result in a disproportionate increase in the rigidity of the MT, causing an overestimate of the rigidity of individual PFs.

If PFs are less rigid than previously thought then the load force $f$, by pulling the Dam1 ring against the splayed PFs, will cause a deformation of the PFs. This deformation would likely manifest as a harmonic potential (due to Hooke's law of elastic deformation).

For this model $\langle\tau\rangle_{\text{binding}}$ determines the residence time, with $\Delta G_{\text{bend}}(x) = \Delta G_{\text{Dam1}} + \frac{1}{2}kx^2$ including the contribution from the rigidity of the PFs, but with the caveat that if the PF lengths go to zero then $\Delta G$ reverts to $\Delta G_{\text{Dam1}}$. Clearly, $\langle\tau\rangle_{\text{bend}}$, the time to escape a potential barrier $\Delta G_{\text{bend}}$ is as the function (4.47) but with an appropriately modified potential $V$. However, because the residence time $\langle\tau\rangle^{(2)}_{\text{hybrid}}$ of this hybrid model will depend on the probability distributions of $\langle\tau\rangle_{\text{PF}}$ and $\langle\tau\rangle_{\text{binding}}$, of which only the means are known, it is presently not possible to state a closed form solution of this time. Stochastic simulations will be necessary

to estimate $\langle\tau\rangle^{(2)}_{\text{hybrid}}$, taking into account switching between potentials based on $\Delta G_{\text{bend}}$ and $\Delta G_{\text{Dam1}}$ as PFs break and grow.

### 4.2.4 Time varying applied forces

Consider an oscillating applied force of the form

$$f(t) = f_0 \sin \omega t + f_1 \tag{4.71}$$

where $f_1 \geq f_0$. A force of this form could easily be applied using current experimental techniques, for example an optical trap, provided $\omega \ll \omega_0$, where $\omega_0$ is the resonance of the trap. Provided the period is sufficiently long $\omega^{-1} \gg \lambda^2/D$ the quasi-static approximation for the ring position should give an accurate estimate for its probability density $\phi(x,t)$. The depolymerisation velocity will be retarded according to (4.7), relating $v$ to $f(t)$.

#### 4.2.4.1 Protofilament model under oscillating force

We seek to solve the model described in §4.2.2 with a time varying $v(t)$ due to $f(t)$ in (4.71). Whereas previously it did not matter to us at what time the previous unzipping event occurred – the waiting time distribution was insensitive to this – here $v(t)$, and consequently $t_{\text{unzip}}$, over the course of the waiting time will depend on the time when the waiting period began $t_0$. Denoting complementary probabilities with a hat, the probability that the MT does *not* unzip in a time $t$ after the time the last unzipping occurred $t_0$ is

$$\hat{P}_{\text{unzip}}(t;t_0) = 1 - P_{\text{unzip}}(t;t_0) = \exp\left(-\int_{t_0}^{t_0+t} \frac{v(t')}{b}\, dt'\right). \tag{4.72}$$

where $v(t)/b = k_{\text{unzip}}(t)$ is the instantaneous rate of unzipping.

Equation (4.72) depends explicitly on $t_0$, which is itself an unknown random variable. To remove this dependence we perform an average over $t_0$, appropriately weighted, to give the probability distribution of times for which the MT does not unzip

$$\begin{aligned}\hat{P}_{\text{unzip}}(t) &= \int_0^{2\pi/\omega} \frac{v(t_0)}{\mathcal{N} b} \hat{P}_{\text{unzip}}(t;t_0)\, dt_0 \\ &= \int_0^{2\pi/\omega} \frac{v(t_0)}{\mathcal{N} b} \exp\left(-\int_{t_0}^{t_0+t} \frac{v(t')}{b}\, dt'\right) dt_0\end{aligned} \tag{4.73}$$

involving a normalization constant $\mathcal{N} = \int_0^{2\pi/\omega} \frac{v(t_0)}{b}\, dt_0$.

To calculate the runtime as in (4.55), we need to first determine the probability the time to unzip $t_{\text{unzip}}$ exceeds the breaking time of the $n$ PFs $t_{\text{pf}}$, that is, the probability $t_{\text{pf}} < t_{\text{unzip}}$

$$\begin{aligned} P_{\text{detach}} &= \int_0^\infty \int_0^t p_{\text{unzip}}(t)\, p_{\text{pf}}(t')\, dt'\, dt \\ &= \int_0^\infty \int_{t'}^\infty p_{\text{unzip}}(t)\, p_{\text{pf}}(t')\, dt\, dt' \\ &= \int_0^\infty \hat{P}_{\text{unzip}}(t')\, p_{\text{pf}}(t')\, dt'. \end{aligned} \tag{4.74}$$

The probability distribution of $t_{\text{pf}}$ was previously stated in (4.52). From the definition of probability density functions, the probability density of $t_{\text{pf}}$ is

$$\begin{aligned} p_{\text{pf}}(t) &= \frac{d}{dt} P_{\text{pf}}(t) = \frac{d}{dt}\left(1 - e^{-k_{\text{break}} t}\right)^n \\ &= n k_{\text{break}} e^{-k_{\text{break}} t}\left(1 - e^{-k_{\text{break}} t}\right)^{n-1}. \end{aligned} \tag{4.75}$$

Putting (4.73) and (4.75) into (4.74)

$$P_{\text{detach}} = \int_0^\infty \int_0^{2\pi/\omega} n k_{\text{break}} e^{-k_{\text{break}} t}\left(1 - e^{-k_{\text{break}} t}\right)^{n-1} \frac{v(t_0)}{\mathcal{N} b} \exp\left(-\int_{t_0}^{t_0+t} \frac{v(t')}{b}\, dt'\right) dt_0\, dt. \tag{4.76}$$

Finally, to obtain the runtime we use (4.55) with the mean unzipping rate

$$\begin{aligned} \langle \tau \rangle &= \frac{1}{P_{\text{detach}} \left\langle k_{\text{unzip}} \right\rangle} \\ &= \frac{1}{P_{\text{detach}}} \frac{\omega}{2\pi} \int_0^{2\pi/\omega} \frac{b}{v(t)}\, dt, \end{aligned} \tag{4.77}$$

where $1/P_{\text{detach}}$ is the mean number of steps before detachment. Note that (4.76) is not analytically tractable but may be solved by numerical quadrature. Numerical solutions to (4.77) are discussed in the results section.

#### 4.2.4.2 Binding model under oscillating force

Provided $\omega^{-1} \gg \lambda^2/D$, the generalisation of (4.47) to the case of time-varying force (4.71) is straightforward, taking an average over the period

$$\langle \tau \rangle = \frac{\omega}{2\pi} \int_0^{2\pi/\omega} \frac{(k_B T)^2}{D f_\epsilon} \left( \frac{1 - f_\epsilon \epsilon / k_B T - e^{f_\epsilon \epsilon / k_B T}}{f_\epsilon} - \frac{1 - e^{f_\epsilon \epsilon / k_B T}}{f} \right) dt, \tag{4.78}$$

| Force $f$ (pN) | $0.5 \pm 0.2$ | $2.0 \pm 0.2$ |
|---|---|---|
| # measurements | 44 | 28 |
| Total depolymerisation time (h) | $0.212 \pm 0.036$ | $0.068 \pm 0.013$ |
| # detachments | 32 | 20 |
| Detachment frequency ($h^{-1}$) | $150 \pm 30$ | $290 \pm 70$ |
| Velocity $v$ (nm/s) | $158 \pm 26$ | $56 \pm 10$ |
| Runtime $\langle\tau\rangle$ (s) [a] | $23.9 \pm 6.2$ | $12.2 \pm 4.1$ |
| Runlength $y$ ($\mu$m) [b] | $3.8 \pm 1.0$ | $0.7 \pm 0.2$ |

[a] Calculated by dividing total depolymerization time by # detachments.
[b] Calculated by multiplying runtime by velocity.

**Table 4.1:** Velocity of ring during microtubule (MT) disassembly under various loads during experiments where load has been applied to a Dam ring attached to a dMT by way of an optical trap. Data obtained from Table 1 of Franck et al. [49]. Runtime and runlength are defined as the time and distance, respectively, between switching to depolymerisation and detachment. The models are constrained by fitting parameters to this data. The nature of MT depolymerisation and ring motion is highly stochastic.

where $f$ and $-f_\epsilon$ are now *time-dependent* potential gradients, according to (4.15) and (4.71).

## 4.3 Results

The following parameters were identified using data reported in the experimental literature; $v_{\text{bb}} = 580$ nm/s [156], $D = 0.083 \pm 0.001$ $\mu$m$^2$/s [160]; for the protofilament model $b = 8$ nm and $n = 13$ are assumed to be typical.

Table 4.1 lists velocities at $f = 0.5$ pN and 2.0 pN. Fitting the velocity model (independently of the protofilament and binding models) to the data produces $\delta = 14.0 \pm 1.4$ nm and $v_{\text{ps}} = 55.0 \pm 9.3$ nm/s.

Combining the available data for velocity and detachment frequency, on average, $\langle\tau\rangle = 23.9$ s and 12.2 s, for $f = 0.5$ pN and 2.0 pN respectively. To fit the binding model for $\langle\tau\rangle$, $\epsilon = 1$ nm was chosen as a reasonable distance over which an attraction might act[5], and for this $\epsilon$ we find $\Delta G_{\text{Dam1}} = 15.24 \pm 0.26$ $k_B$T. This corresponds to a force of about 60 pN acting over 1 nm at room temperature. Note that this does not imply that it would require a 60 pN force to remove the Dam1 ring from the MT; rather, it simply gives an indication that the binding between Dam1 and MT is quite strong.

Independently, a fit for $k_{\text{break}}$ can be made for the protofilament model and for these data $k_{\text{break}} = 7.12 \pm 0.63$ s$^{-1}$. An MT depolyermising with $v_{\text{bb}} = 580$ nm/s must be losing subunits with a rate $v_{\text{bb}}/b = 72.5$ subunits/s per PF, approximately

[5] The Debye length in biological electrolyte solution is on the order of 1 nm

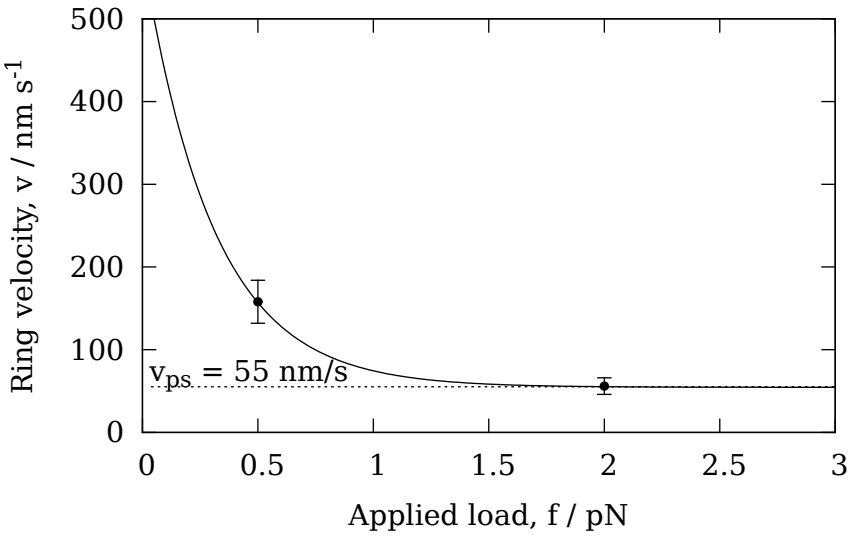


**Figure 4.9:** The variation of velocity of the Dam1 ring with applied load. The velocity falls as the force increases because the motion must increasingly rely on the energetic powerstroke. Note that, although the graph appears to suggest an absence of a stalling force, at significantly higher forces the assumption of constant $v_{ps}$ would fail and the ring would stall. The curve is produced from the best fit of $\delta$ and $v_{ps}$ in (4.7) and data from [49].

ten-fold higher than the fitted $k_{break}$. However, snapshots of depolymerising MTs in cryo-EM [25] show the PF curls having a mean length of $L \approx 10$ subunits. Therefore, as the subunit closest to the MT lattice unzipping point depolymermises with rate $k_{break}$, the total subunit loss is $Lk_{break}$ as losing that subunit takes the entire PF curl with it, reconciling $v_{bb}$ and $k_{break}$.

Fitting these parameters to just two data points naturally does not provide strong evidence for these particular values, and it is not argued as such. However, uncertainty in the exact parameter values should not detract from the main value of the work presented here; to provide a model that explains the Dam1 force sensitivity and to distinguish between binding and protofilament models. Indeed, the striking differences in qualitative behaviour between the models under parameter variations does not depend on the precise parameter values. Comparison of the fits for velocity $v$ and mean runtime $\langle\tau\rangle$ with data are shown in Figure 4.9 and Figure 4.10, respectively.

An alternative means of comparison between the protofilament and binding models is to determine the parameters required to make them agree on $\langle\tau\rangle$. Figure 4.11 shows the value of $\Delta G_{Dam1}$ required to make the binding model agree with the protofilament model. A variation of only $\approx 1\ k_BT$ in $\Delta G_{Dam1}$ is required. However, for simplicity of comparison when varying parameters, the above, independently derived, fit parameters are used in the following.

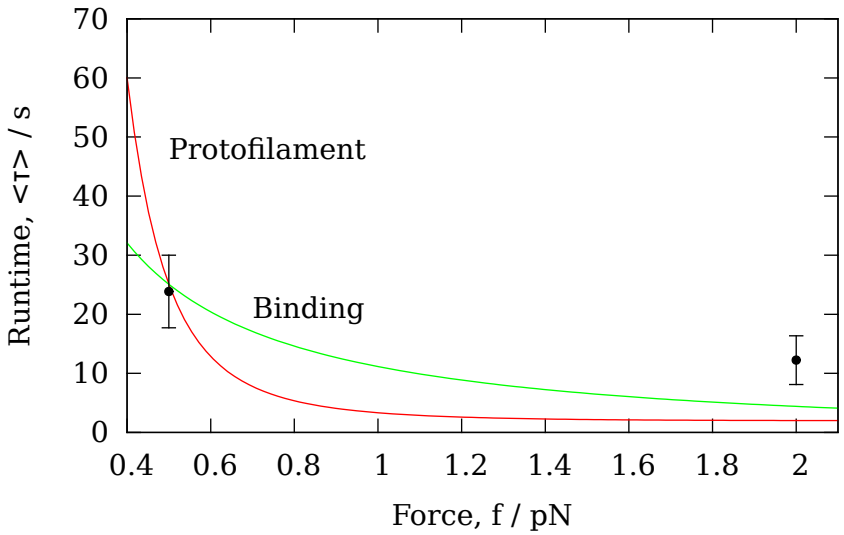


**Figure 4.10:** Runtime of the protofilament and binding models. The runtime $\langle\tau\rangle$ of each model is calculated using the parameters fitted as described in the Results section. Although, it may seem that distinguishing the models by varying force is possible due to the difference between their predicted behaviour, as shown here, the difference is close to experimental error (±6.15 s) and both models present similar functional form. Only two data points with sufficient statistics were available to perform this fitting [49] making it difficult to draw any conclusions from this approach. The fit provides values for $\Delta G_{\text{Dam1}}$ for the binding model and $k_{\text{break}}$ for the protofilament model.

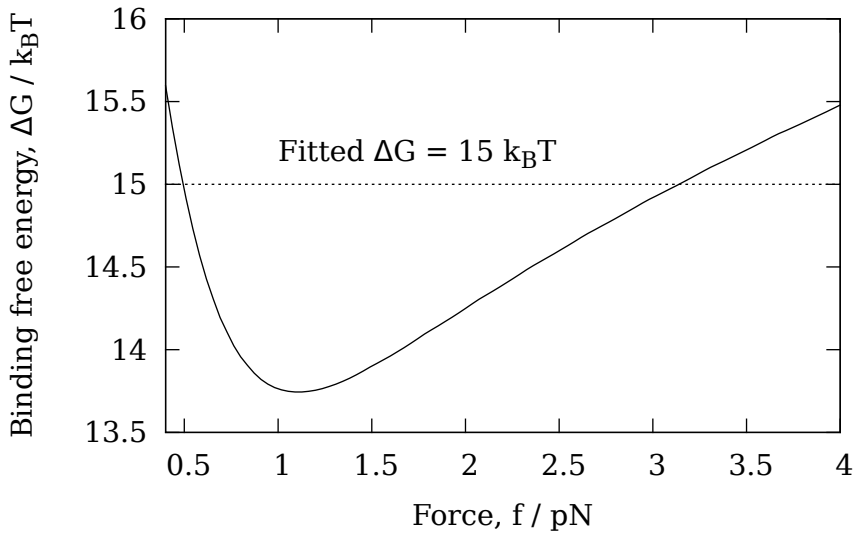


**Figure 4.11:** The strength of Dam1 ring to microtubule (MT) binding, in terms of free energy change, required for the runtimes of the binding and protofilament models to match, as a function of load force. The dotted line indicates the value obtained from the fit to data from [49].

### 4.3.1 Direct comparison by variation of force

As discussed above, in order to constrain parameter values, the protofilament and binding models are independently fit for $\langle\tau\rangle$ against data. The quality of the fit is not high for the data point at $f = 2$ pN. This is because the runtimes are exponentially sensitive to $f$, and therefore tighter fitting to the point at $f = 0.5$ pN results in the lowest residuals. Although, there is no *a priori* reason to expect that the performance (in terms of runtime) of each model should be comparable across the range of force considered, Figure 4.10 shows both model predict reasonably similar runtimes. The maximium deviation of $\approx 10$ s is at around $f = 0.8$ pN. Outside the range of the data, $f < 0.5$ pN, the deviation between the models becomes greater.

Due to the range of experimental error, and furthermore, approximations inherent to the model, $\tau$ as a function of load force, although the only data currently available, does not present a suitable method for the discrimination of protofilament and binding type models. Therefore, the variation of other parameters must be examined.

### 4.3.2 Variation of intrinsic depolymerisation velocity

The protofilament model exhibits the most sensitivity to the intrinsic (bare) MT depolymerisation velocity $v_{\mathrm{bb}}$, as is shown in Figure 4.12. For the protofilament

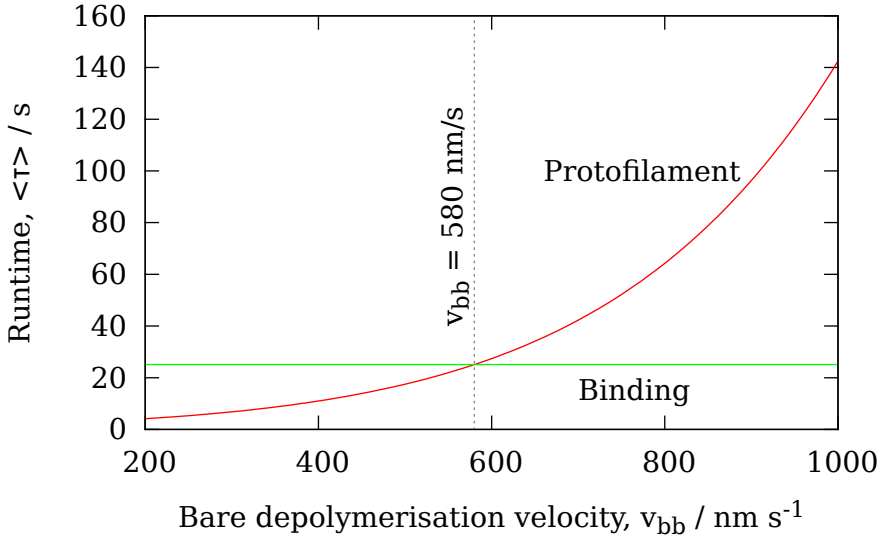


**Figure 4.12:** Variation of runtime $\langle\tau\rangle$ with bare microtubule (MT) depolymerisation velocity $v_{bb}$. The load is $f = 0.45\,\text{pN}$. The runtime $\langle\tau\rangle$ increases exponentially with $v_{bb}$ for the protofilament model, whilst the binding model is insensitive. This is because the protofilament model directly depends on $v$, but the binding model does not.

model, $\langle\tau\rangle$ is strongly dependent on $\left\langle t_{unzip}\right\rangle$ and consequently $v_{bb}$. The binding model, on the other hand, is only weakly dependent on $v$ (due to the effect of viscous drag; see §4.1.3). On this range of $v_{bb}$ it can be assumed that depolymerisation is quasistatically slow with respect to ring diffusion. The result can be understood physically by realising that as $v_{bb}$ increases, the rate of PF unzipping $k_{unzip}$ also increases, while $k_{break}$ remains constant making it less likely that the PFs will break off sufficiently quickly to release the ring.

An experimental test that might be able to distinguish which model operates could be achieved, e.g., by addition of a depolymerisation inducing agent, such as $Ca^{2+}$ [175], or MCAK [176], while applying a load. Alternatively, low concentrations of a MT stabiliser, such as taxol [177], could be used to reduce $v_{bb}$ and provide discrimination.

### 4.3.3 Changing of diffusion coefficient

The diffusion constant $D$ of the ring is determined by the ring's dimensions and the roughness of the binding energy landscape along the MT, rather than the magnitude of the binding energy itself. For example, even a tightly bound ring will diffuse freely on a MT if the binding potential does not vary greatly with position. A rougher landscape reduces the mobility of the ring by providing a sequence of energy barriers, microscopically separated along the MT. Figure 4.13 shows the

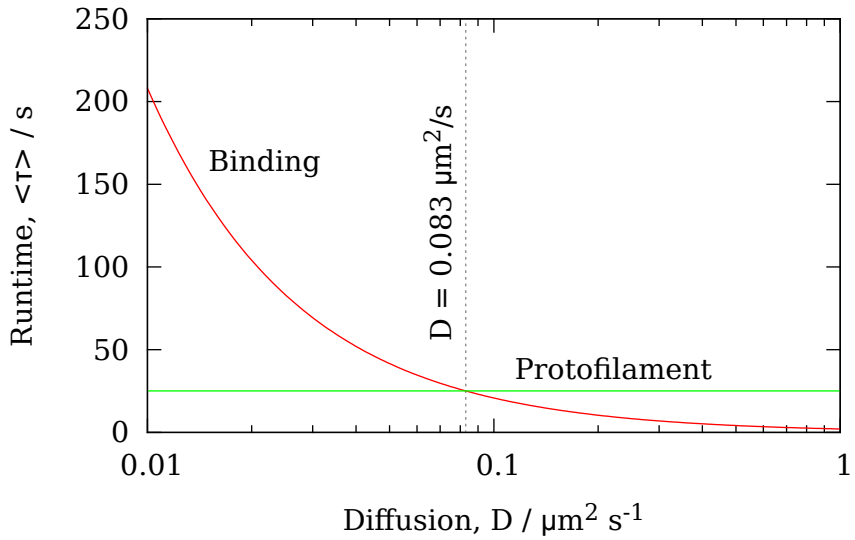


**Figure 4.13:** Variation of runtime $\langle\tau\rangle$ with diffusion coefficient $D$. The load is $f = 0.45$ pN. Restricted diffusion suppresses detachment for the binding model because $\langle\tau\rangle$ is inversely related to $D$, due to the reduced impetus to escape the potential barrier. The protofilament model, on the other hand, is not affected by $D$ since $t_{\text{unzip}}$ is independent of $D$. Distinguishing between models will be easiest by experimental reduction of $D$, for example by attachment of a long polymer.

effect of the diffusion constant on the runtime for both models. Provided, the assumption of negligible first-passage time for the ring from equilibrium to escape holds good (§4.2.2.1), only the binding model is sensitive to change in $D$, having reduced runtime with faster diffusion. This is because the increased mobility of ring increases the chance it is able to scale the potential barrier constraining it to the MT. Over the range of $D$ shown in Figure 4.13, the first-passage assumption is valid.

Although it may be possible to alter $D$ biochemically, for example by phosphorylation [160], it is difficult to do so independently of $\Delta G_{\text{Dam1}}$, as this amounts to modifying the binding potential landscape. Decreasing $D$ may be better accomplished by attaching a long inert polymer to the complex to increase viscous drag. The Kirkwoord formula provides an upper bound (which is quite accurate for flexible polymers [178]) on the diffusion constant of a polymer $D_P$ [179]

$$D_P = \frac{k_B T}{6\pi\eta N^2} \sum \left\langle \frac{1}{|R_n - R_m|} \right\rangle_{\text{eq}} \tag{4.79}$$

where $\eta$ is the viscosity of the solvent, $N$ is the number of segments in the polymer and the sum is over the reciprocal of mean distance between polymer segments at equilibrium. Clearly, longer and more spread out polymers have significantly lower $D_P$.

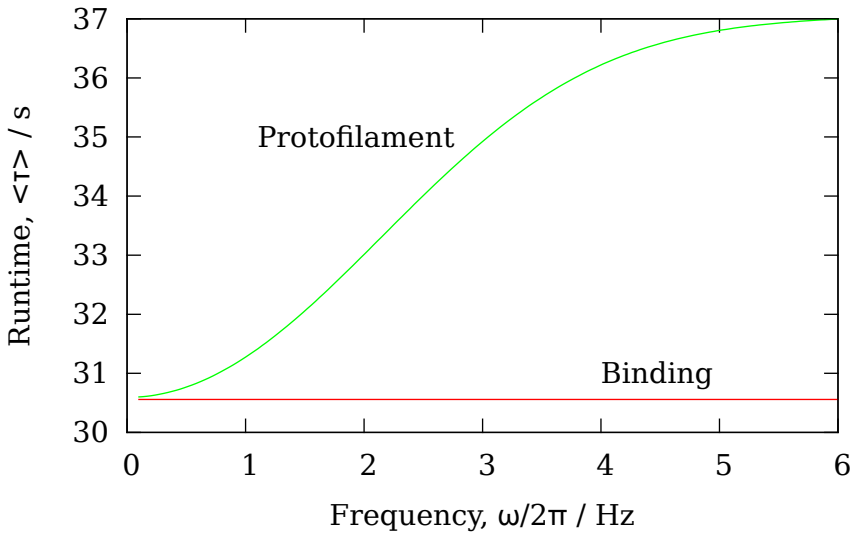


**Figure 4.14:** Variation of runtime $\langle\tau\rangle$ with frequency of applied force $\omega/2\pi$. The binding model is sensitive only to the amplitudes $f_0$ (here 0.1 pN) and $f_1$ (here 0.43 pN), not the frequency $\omega$. The rate of detachment for the protofilament model instead strongly depends on the frequency: roughly speaking the ring is lost more quickly when the high force part of the cycle persists for long enough for the protofilaments (PFs) to completely depolymerize in this time, i.e. when the period is long and the frequency short.

### 4.3.4 Effect of time-varying loading force

A time-varying force provides another simple method of model discrimination, one which likely requires very little modification of current experimental protocol. As shown in §4.2.4, the runtime in the binding model is sensitive only to the instantaneous force provided $2\pi/\omega \gg \lambda^2/D$. For such a frequency, the force oscillation is averaged out over times much shorter than the escape time $\langle\tau\rangle$, and therefore $\langle\tau\rangle$ only depends in an averaged sense on $f(t)$. If $f_1 = 1\,\text{pN}$, for example, then $2\pi\omega_{\text{max}}$ is on the order of 1 kHz. The runtime in the protofilament model is sensitive to the time over which changes in $v$ persist. If the force is oscillating with a long period then the rate of detachment will be greater in the high force part of the cycle than if the period is short. This is because the Dam1 ring takes some time to detach if it needs to first wait for the PF curls to break (see Figure 4.14). In experiments employing oscillating forces, a sigmoidal increase of $\langle\tau\rangle$ with $\omega$ would be a signature of a system that depends on a second independent time ($1/k_{\text{break}}$), like the protofilament model; insensitivity of $\langle\tau\rangle$ to frequency would imply a direct binding-style coupling.

## 4.4 Summary

In this chapter two different models for Dam1 ring retention on a depolymerising MT, based on either a Dam1 ring-MT binding attraction or steric confinement by PFs, were developed and solved. Fundamental to both is a common model for how the Dam1 ring affects depolymerisation. Fitting this model to data indicated that a MT depolymerisation powerstroke takes effect at forces > 2 pN.

The two retention models are not identifiable when varying force. Therefore new experimental protocols were suggested that would allow discrimination between the models. These involve varying the MT depolymerisation rate, the Dam1 ring diffusion coefficient, or the frequency of an oscillating applied load.

# 5

# Theoretical analysis of tube-pulling from solid-supported lipid bilayers

In this chapter, solid-supported bilayer lipid tube pulling experiments are investigated theoretically. An equation representing the shape of a lipid bilayer attached with finite radius to a probe and to the surface is derived. This equation is used to calculate free energy profiles for pulling experiments and hence, theoretical force curves.

## 5.1 Equilibrium shape equation

A relaxed solid-supported lipid bilayer is a flat membrane resting on a surface. In an atomic force microscope (AFM) pulling experiment a flat probe of radius $r_p$ is attached to the membrane and pulled back a specified distance $z_1$ at a specified velocity $v_p$. To model this experiment, assume that the shape formed by the membrane is axisymmetric, i.e. symmetrical on rotation about the pulling axis $r = 0$, and has zero thickness. The membrane is therefore representable as a line (see Figure 5.1). The surface support is the line $z = 0$. When the membrane is pulled to non-zero height $z_p$, the membrane must leave the surface at some radius $r_f$.

A bilayer membrane is an elastic structure and hence has an free energy associated with bending. The most common free energy used in membrane modelling is the spontaneous curvature model proposed by Helfrich for red blood cells [95]. The membrane is assumed to have a natural, or spontaneous, curvature $C_0$;

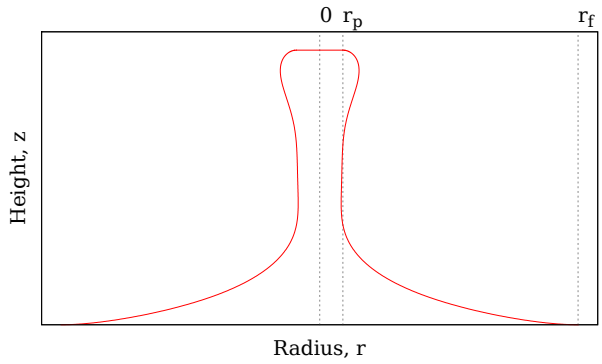


**Figure 5.1:** Coordinate system of membrane segment. The solid support is the line $z = 0$. Due to axisymmetry, the contour for $r < 0$ is the mirror image of the contour for $r > 0$. At height $z_p$, the probe height, the contour is fixed at radius $r_p$, the probe radius. The radius at which the contour leaves the surface is $r_f$.

deviations from $C_0$ cost energy

$$F_{\text{bending}} = \frac{\kappa}{2} \int (2H - C_0)^2 \, dA \tag{5.1}$$

where $\kappa$ is the bending rigidity[1], $H$ is the mean curvature and $dA$ is an area element. The area of and volume enclosed by the membrane segment also contribute to the free energy due to surface tension $\sigma$ and pressure $P$, so the total free energy is

$$F = \frac{\kappa}{2} \int (2H - C_0)^2 \, dA - P \int dV + \sigma \int dA. \tag{5.2}$$

where $H$ is the mean curvature of the surface, $dV$ and $dA$ are volume and area elements, respectively.

The model can be simplified by rescaling the parameters. Here, the parameters are scaled by $\kappa$

$$\bar{\sigma} = \sigma/\kappa \quad \bar{P} = P/\kappa. \tag{5.3}$$

### 5.1.1 Equilibrium tube

Equation (5.2) is easy to calculate for a tubular membrane segment of length $h$, with $P = 0$ and $C_0 = 0$ [105]. Explicitly including the free energy due to the force applied to the tube

$$F_{\text{tube}} = \frac{\kappa}{2r^2} h + 2\pi r \sigma h - fh. \tag{5.4}$$

The equilibrium radius $r_0$ and force $f_0$ can be calculated by taking derivatives

[1]The bending rigidity $\kappa$ is the product of the Young's modulus and the area moment of inertia of the membrane $EI$.

of $F_{\text{tube}}$ equal to zero. Firstly, for $r$

$$\frac{\partial F_{\text{tube}}}{\partial r} = 0 = 2\pi\sigma h - \frac{\kappa}{r^2}\pi h, \tag{5.5}$$

therefore

$$r_0 = \sqrt{\frac{\kappa}{2\sigma}}. \tag{5.6}$$

For $f$

$$\frac{\partial F_{\text{tube}}}{\partial f} = 0 = 2\pi r\sigma + \frac{\kappa\pi}{r} - f \tag{5.7}$$

therefore

$$\begin{aligned} f_0 &= \pi(2\sigma r_0 + \frac{\kappa}{r_0}) \\ &= 2\pi\sqrt{2\sigma\kappa}. \end{aligned} \tag{5.8}$$

### 5.1.2 Derivation of shape equation

The derivation of the shape equation follows the method described in Seifert et al. [98] and Jülicher and Seifert [100] for pulling tubes from vesicles, a analogous experiment to pulling tubes from a surface, with the exception that the membrane contour cannot pass through the line $z = 0$. This additional constraint will be discussed in §5.2. To avoid singularities in the derivatives $dr/dx$ and $dz/dx$, a coordinate system is adopted based on the arc length $s$ along the one-dimensional (1D) curve segment (see Figure 5.1). In this system

$$z'(s) = -\sin\psi(s) \tag{5.9a}$$

$$r'(s) = \cos\psi(s), \tag{5.9b}$$

where $r(s)$ and $z(s)$ are the radius and height of the membrane at $s$, respectively, $\psi(s)$ is the angle of the surface against the horizontal at $s$. Here, and for the rest of this chapter, each prime denotes differentiation with respect to $s$. In these coordinates, the mean curvature of the surface is the mean of the curvature along the 1D segment and the curvature of the circumference of the surface

$$H = \frac{1}{2}\left(\psi' + \frac{\sin\psi}{r}\right). \tag{5.10}$$

Taking advantage of axisymmetry, assuming zero spontaneous curvature $c_0$ (since both leaflets of the bilayer are identical), and the parameter rescalings (5.3),

we can transform (5.2) into an integral over the arc length $s$

$$F(r,z,\psi) = 2\pi\kappa \int_{s_a}^{s_b} r\left[\frac{1}{2}\left(\psi' + \frac{\sin\psi}{r}\right)^2 + \bar{\sigma} - \frac{\bar{P}}{2} r\sin\psi\right] ds. \tag{5.11}$$

In order to find the equilibrium shape of the membrane, we look for the minimum of the free energy (5.11), subject to the constraints (5.9a) and (5.9b). We therefore apply calculus of variations to minimise the functional

$$F = 2\pi\kappa \int_{s_a}^{s_b} L\, ds, \tag{5.12}$$

with

$$L = \frac{r}{2}\left(\psi' + \frac{\sin\psi}{r}\right)^2 + \bar{\sigma} r - \frac{\bar{P}}{2} r^2 \sin\psi + \gamma(r' - \cos\psi) + \eta(z' + \sin\psi) \tag{5.13}$$

where we have added Lagrange multipliers $\eta$ and $\gamma$ to enforce (5.9a) and (5.9b), respectively.

In the function $F$, $\psi$, $r$, $z$, $\gamma$ and $\eta$ are functions of $s$. Suppose that $\psi_0(s)$, $r_0(s)$, $z_0(s)$, $\gamma_0(s)$ and $\eta_0(s)$ are functions that minimise $F$, then the following functions increase $F$

$$\begin{aligned}
\psi(s) &= \psi_0(s) + \delta\psi(s) \\
r(s) &= r_0(s) + \delta r(s) \\
z(s) &= z_0(s) + \delta z(s) \\
\gamma(s) &= \gamma_0(s) + \delta\gamma(s) \\
\eta(s) &= \eta_0(s) + \delta\eta(s),
\end{aligned}$$

where the notation $\delta$ indicates the variation of the function, a small, smooth function that is zero at the boundaries. For $F$ to have a minimum it is necessary for the variation of $F$ to be zero

$$\delta F = \delta \int_{s_a}^{s_b} L(\psi, \psi', r, r', z, z', \eta, \eta', \gamma, \gamma', s)\, ds = 0. \tag{5.14}$$

Effecting the variation,

$$\begin{aligned}
\int_{s_a}^{s_b} \Bigg(&\frac{\partial L}{\partial \psi}\delta\psi + \frac{\partial L}{\partial \psi'}\delta\psi' + \frac{\partial L}{\partial r}\delta r + \frac{\partial L}{\partial r'}\delta r' + \frac{\partial L}{\partial z}\delta z \\
&+ \frac{\partial L}{\partial z'}\delta z' + \frac{\partial L}{\partial \eta}\delta\eta + \frac{\partial L}{\partial \eta'}\delta\eta' + \frac{\partial L}{\partial \gamma}\delta\gamma + \frac{\partial L}{\partial \gamma'}\delta\gamma'\Bigg) ds = 0,
\end{aligned} \tag{5.15}$$

where $\delta r' = d\delta r/dt$, etc.. Integrating by parts the terms containing first derivatives of the variations

$$\delta F = \left[\frac{\partial L}{\partial \psi'}\delta\psi\right]_{s_a}^{s_b} + \left[\frac{\partial L}{\partial r'}\delta r\right]_{s_a}^{s_b} + \left[\frac{\partial L}{\partial z'}\delta z\right]_{s_a}^{s_b} + \left[\frac{\partial L}{\partial \eta'}\delta\eta\right]_{s_a}^{s_b} + \left[\frac{\partial L}{\partial \gamma'}\delta\gamma\right]_{s_a}^{s_b} + \int_{s_a}^{s_b}\left(\frac{\partial L}{\partial \psi} - \frac{d}{ds}\frac{\partial L}{\partial \psi'}\right)\delta\psi + \left(\frac{\partial L}{\partial r} - \frac{d}{ds}\frac{\partial L}{\partial r'}\right)\delta r + \left(\frac{\partial L}{\partial z} - \frac{d}{ds}\frac{\partial L}{\partial z'}\right)\delta z + \left(\frac{\partial L}{\partial \eta} - \frac{d}{ds}\frac{\partial L}{\partial \eta'}\right)\delta\eta + \left(\frac{\partial L}{\partial \gamma} - \frac{d}{ds}\frac{\partial L}{\partial \gamma'}\right)\delta\gamma\, dt = 0. \quad (5.16)$$

At the boundaries $s_a$ and $s_b$ the variations are zero, hence the integrated terms are zero. The integral vanishes for arbitrary variations if, and only if, the bracketed terms are identically zero. Thus

$$\frac{\partial L}{\partial \psi} - \frac{d}{ds}\frac{\partial L}{\partial \psi'} = 0 \quad (5.17)$$

$$\frac{\partial L}{\partial r} - \frac{d}{ds}\frac{\partial L}{\partial r'} = 0 \quad (5.18)$$

$$\frac{\partial L}{\partial z} - \frac{d}{ds}\frac{\partial L}{\partial z'} = 0 \quad (5.19)$$

$$\frac{\partial L}{\partial \eta} - \frac{d}{ds}\frac{\partial L}{\partial \eta'} = 0 \quad (5.20)$$

$$\frac{\partial L}{\partial \gamma} - \frac{d}{ds}\frac{\partial L}{\partial \gamma'} = 0, \quad (5.21)$$

for a minimum of $F$. These equations are called the Euler-Lagrange equations for (5.12). Evaluating the equation for $\psi$

$$\frac{\partial L}{\partial \psi} - \frac{d}{ds}\frac{\partial L}{\partial \psi'} = \left[\psi' \cos\psi + \frac{\cos\psi\, \sin\psi}{r} - \frac{\bar{P}}{2}r^2\cos\psi + \gamma\sin\psi + \eta\cos\psi\right] - \frac{d}{ds}\left[r\psi' + \sin\psi\right] \quad (5.22)$$

$$= \psi'\cos\psi + \frac{\cos\psi\sin\psi}{r} - \frac{\bar{P}}{2}r^2\cos\psi + \gamma\sin\psi + \eta\cos\psi - r'\psi' - r\psi'' - \psi'\cos\psi \quad (5.23)$$

$$= 0. \quad (5.24)$$

After rearrangement, we have the following differential equation

$$\psi'' = \frac{\cos\psi\sin\psi}{r^2} - \frac{\psi'\cos\psi}{r} - \frac{\bar{P}}{2}r\cos\psi + \frac{\gamma\sin\psi}{r} + \frac{\eta\cos\psi}{r}. \quad (5.25)$$

For $r$ we have

$$\frac{\partial L}{\partial r} - \frac{d}{ds}\frac{\partial L}{\partial r'} = \left[\frac{\psi'^2}{2} - \frac{\sin^2\psi}{2r} + \bar{\sigma} - \bar{P}r\sin\psi\right] - \frac{d\gamma}{ds} = 0, \tag{5.26}$$

and rearranging

$$\gamma' = \frac{\psi'^2}{2} - \frac{\sin^2\psi}{2r} + \bar{\sigma} - \bar{P}r\sin\psi. \tag{5.27}$$

The Euler-Lagrange equation for $z$ is trivial

$$\frac{\partial L}{\partial z} - \frac{d}{ds}\frac{\partial L}{\partial z'} = \eta' = 0. \tag{5.28}$$

The Euler-Lagrange equations for $\eta$ and $\gamma$ are both equivalent to the constraints (5.9a) and (5.9b) that we wished to impose in the first place.

The Hamiltonian $\mathcal{H}$ is defined as the Legendre transform of the Lagrangian $L$

$$\mathcal{H} = \sum_i q_i' p_i - L, \tag{5.29}$$

where $q_i$ and $p_i$ are generalised position and momentum coordinates, respectively. In the coordinate system defined by (5.9), the Hamiltonian is

$$\mathcal{H} = \psi'\frac{\partial L}{\partial \psi'} + z'\frac{\partial L}{\partial z'} + r'\frac{\partial L}{\partial r'} - L, \tag{5.30}$$

where

$$\begin{aligned}\frac{\partial L}{\partial \psi'} &= r\psi' + \sin\psi \\ \frac{\partial L}{\partial z'} &= \eta \\ \frac{\partial L}{\partial r'} &= \gamma.\end{aligned}$$

Moreover, since $L$ does not depend on $s$, the Hamiltonian $\mathcal{H}$ is conserved along

the membrane segment[2], providing an additional equation. Thus

$$\mathcal{H} = -\frac{r}{2}\left(\psi' + \frac{\sin\psi}{r}\right)^2 - \bar{\sigma}r + \frac{\bar{P}}{2}r^2\sin\psi + \gamma(r' - \cos\psi) - \eta(z' + \sin\psi) \tag{5.31}$$

$$+ \psi' r\left(\psi' + \frac{\sin\psi}{r}\right) + z'\eta + r'\gamma$$

$$= \frac{r\psi'^2}{2} - \frac{\sin^2\psi}{2r} - \bar{\sigma}r + \frac{\bar{P}}{2}r^2\sin\psi + \gamma\cos\psi - \eta\sin\psi + r\psi'^2$$

$$= 0. \tag{5.32}$$

Rearranging (5.32)

$$\eta = \frac{r\psi'^2}{2\sin\psi} - \frac{\sin\psi}{2r} - \frac{\bar{\sigma}r}{\sin\psi} + \frac{\bar{P}}{2}r^2 + \gamma\frac{\cos\psi}{\sin\psi} \tag{5.33}$$

substituting into (5.25)

$$\psi'' = \frac{\cos\psi\sin\psi}{r^2} - \frac{\cos\psi\,\psi'}{r} - \frac{\bar{P}}{2}r\cos\psi + \gamma\frac{\sin\psi}{r} + \frac{\cos\psi}{r}\left[\frac{r\psi'^2}{2\sin\psi} - \frac{\sin\psi}{2r}\right.$$

$$\left. - \frac{\bar{\sigma}r}{\sin\psi} + \frac{\bar{P}r^2}{2} + \gamma\frac{\cos\psi}{\sin\psi}\right], \tag{5.34}$$

and rearranging again

$$\gamma = \psi'' r\sin\psi - \frac{\cos\psi\sin^2\psi}{r} + \psi'\sin\psi\cos\psi - \frac{r}{2}\psi'^2\cos\psi + \frac{\cos\psi\sin^2\psi}{2r} + \bar{\sigma}r\cos\psi. \tag{5.35}$$

Differentiating with respect to $s$

$$\gamma' = \psi'''r\sin\psi + \psi''r'\sin\psi + \psi''\psi r\cos\psi + \frac{r'\cos\psi\sin^2\psi}{r^2} + \frac{\psi'\sin^3\psi}{r} - \frac{2\psi'\cos^2\psi\sin\psi}{r}$$

$$+ \psi''\sin\psi\cos\psi + \psi'^2\cos^2\psi - \psi'^2\sin^2\psi - \psi''\psi' r\cos\psi - \frac{r'}{2}\psi'^2\cos\psi + \frac{r}{2}\psi'^3\sin\psi$$

$$- \frac{r'\cos\psi\sin^2\psi}{2r^2} - \frac{\psi'\sin^3\psi}{2r} + \frac{\psi'\cos^2\psi\sin\psi}{r} + \bar{\sigma}r'\cos\psi - \bar{\sigma}r\psi'\sin\psi. \tag{5.36}$$

[2]Noether's theorem: Lagrangian invariant under transformations in $s$ implies $\mathcal{H} = \sum_i p_i q_i' - L$ is conserved.

Inserting (5.36) into (5.27) and factorising

$$\frac{\psi'^2}{2} - \frac{\sin^2\psi}{2r^2} + \bar{\sigma} - \bar{P}r\sin\psi = \psi'''r\sin\psi + \psi''\psi'\left[r\cos\psi - r\cos\psi\right] + 2\psi''\cos\psi\sin\psi$$
$$+ \psi'\left[\frac{\sin^3\psi}{r} - \frac{2\cos^2\psi\sin\psi}{r} - \frac{\sin^3\psi}{2r} + \frac{\cos^2\psi\sin\psi}{r} - \bar{\sigma}r\sin\psi\right]$$
$$+ \psi'^2\left[\cos^2\psi - \sin^2\psi - \frac{1}{2}\cos^2\psi\right] + \frac{r}{2}\psi'^3\sin\psi +$$
$$\frac{\cos^2\psi\sin^2\psi}{r^2} - \frac{\cos^2\psi\sin^2\psi}{2r^2} + \bar{\sigma}\cos^2\psi. \quad (5.37)$$

Finally, after rearranging for the highest derivative of $\psi$, we have the differential equation defining the membrane shape

$$\psi''' = -\frac{1}{2}\psi'^3 - \frac{2\cos\psi}{r}\psi'' + \frac{3\sin\psi}{2r}\psi'^2 + \frac{3\cos^2\psi - 1}{2r^2}\psi' + \psi'\bar{\sigma}$$
$$- \frac{(\cos^2\psi + 1)\sin\psi}{2r^3} + \frac{\bar{\sigma}\sin\psi}{r} - \bar{P}. \quad (5.38)$$

To numerically solve this third-order ordinary differential equation (ODE), it is convenient to recast it as three coupled first-order ODEs. Let

$$\phi_1 = \psi \quad (5.39a)$$
$$\phi_2 = \psi' \quad (5.39b)$$
$$\phi_3 = \psi'' \quad (5.39c)$$

After making the appropriate substitutions and adding the constraints of the coordinate system we have the following first-order ODE system

$$\phi_1' = \phi_2 \quad (5.40a)$$
$$\phi_2' = \phi_3 \quad (5.40b)$$
$$\phi_3' = -\frac{1}{2}\phi_2^3 - \frac{2\phi_3\cos\phi_1}{r} + \frac{3\sin\phi_1}{2r}\phi_2^2 + \frac{3\cos^2\phi_1 - 1}{2r^2}\phi_2 + \phi_2\bar{\sigma} \quad (5.40c)$$
$$- \frac{(\cos^2\phi_1 + 1)\sin\phi_1}{2r^3} + \frac{\bar{\sigma}\sin\phi_1}{r} - \bar{P} \quad (5.40d)$$
$$r' = \cos\phi_1 \quad (5.40e)$$
$$z' = -\sin\phi_1, \quad (5.40f)$$

defined over the arc interval $[s_a, s_b]$.

To (5.40) we add the following boundary conditions that impose the attach-

ments to the surface and probe described earlier

$$\phi_1(s_a) \equiv \psi(s_a) = \Psi \qquad \phi_1(s_b) \equiv \psi(s_b) = 0 \tag{5.41a}$$

$$r(s_a) = r_p \qquad r(s_b) = r_f \tag{5.41b}$$

$$z(s_a) = z_p \qquad z(s_b) = 0 \tag{5.41c}$$

where $\Psi \in [0, \pi/2]$.

The ODE (5.40) is known as a boundary value problem because conditions are imposed on both ends of the domain. To be well-posed we require as many boundary conditions as there are differential equations. In principle, we can solve this system over the arc-length interval $[s_a, s_b]$. However, we do not *a priori* know $s_a$ or $s_b$. We can set, without loss of generality, $s_a = 0$. To solve over an interval of unknown length we can scale the independent variable by letting $x = s/s_b$ and introducing a sixth equation

$$\frac{ds_b}{dx} = 0. \tag{5.42}$$

We then redefine as derivatives with respect to $x$, multiplying the right-hand side of each ODE by $s_b$. We can then solve over the interval $x = [0, 1]$ and let the solution of (5.42) determine $s_b$ [180]. As (5.40) is highly nonlinear, it is necessary to employ numerical methods to find the solution.

## 5.2 Imposing the surface constraint

As it stands, the shape equation (5.40) admits solutions with $z(s) < 0$ for a portion of the membrane contour, which is unacceptable for modelling lipid tube pulling from a solid impenetrable surface. In such an experiment the following constraint must be imposed

$$z(s) > 0. \tag{5.43}$$

For $P = 0$ this does not generally pose a problem as when parameters are varied to find free energy minima, the solution with minimum free energy satisfies the constraint, as long as the parameters are not in any way 'extreme'. This is as expected because extending the contour beneath $z = 0$ only increases the area of the membrane segment and curvature energy. In an AFM tube pulling experiment, however, it is almost certain that $P \neq 0$. This is because the volume contained by the membrane can only be filled with fluid at a finite rate. When $P \neq 0$, the solution to (5.40) almost invariably violates (5.43).

To impose constraint (5.43) we use the penalty function method [181]. The idea is to add a penalty function $\Pi$ to the quantity to be minimised - the objective function, here $F$ - and multiply it by a constant factor $\mu$. Setting initially $\mu = 0$, we

solve the unconstrained problem. The factor $\mu$ is then increased iteratively until the constraint is satisfied. There are several possibilities for the form of $\Pi$; the following two were tried here: a) $\Pi_1 = z^2$ and b) $\Pi_2 = [\min(0, z)]^2$, proposed by Courant [182] and Zangwill [183], respectively.

Equation (5.13) with $\Pi_1$ becomes

$$L = \frac{r}{2}\left(\psi' + \frac{\sin\psi}{r}\right)^2 + \bar{\sigma}r - \frac{\bar{P}}{2}r^2\sin\psi + \gamma(r' - \cos\psi) + \eta(z' + \sin\psi) + \mu z^2. \quad (5.44)$$

After following an analogous derivation as in §5.1, the shape equation incorporating $\Pi_1$ is

$$\psi''' = -\frac{1}{2}\psi'^3 - \frac{2\cos\psi}{r}\psi'' + \frac{3\sin\psi}{2r}\psi'^2 + \frac{3\cos^2\psi - 1}{2r^2}\psi' + \psi'\bar{\sigma} - \frac{(\cos^2\psi + 1)\sin\psi}{2r^3} + \frac{\bar{\sigma}\sin\psi}{r} - \bar{P} + 2\mu z\frac{\cos\psi\sin\psi}{R} + \psi'\mu z^2\frac{(2\sin^2\psi - 1)}{R\sin\psi}. \quad (5.45)$$

With $\Pi_2$ becomes

$$L = \frac{r}{2}\left(\psi' + \frac{\sin\psi}{r}\right)^2 + \bar{\sigma}r - \frac{\bar{P}}{2}r^2\sin\psi + \gamma(r' - \cos\psi) + \eta(z' + \sin\psi) + \mu\min(0, z), \quad (5.46)$$

and again following the derivation above

$$\psi''' = -\frac{1}{2}\psi'^3 - \frac{2\cos\psi}{r}\psi'' + \frac{3\sin\psi}{2r}\psi'^2 + \frac{3\cos^2\psi - 1}{2r^2}\psi' + \psi'\bar{\sigma} - \frac{(\cos^2\psi + 1)\sin\psi}{2r^3} + \frac{\bar{\sigma}\sin\psi}{r} - \bar{P} - 2\mu\min(0, z)M(z)\frac{\cos\psi}{r} + \psi'\mu[\min(0, z)]^2\frac{(2\sin^2\psi - 1)}{r\sin\psi}. \quad (5.47)$$

where

$$M(z) = \begin{cases} 0 & z \geq 0 \\ -\sin\psi & z < 0. \end{cases}$$

## 5.3 Numerical solution of the shape equation

An initial attempt at solving (5.40) included implementing a shooting method (see §C.1) using the `ode45` initial value problem (IVP) solver in `MATLAB`, but it was not possible to extend the solutions using continuation beyond small $z_p$. Continuation also failed using the collocation finite-difference (see §C.2) solver `COLSYS` [184]. For finite $r_p$ the membrane undergoes a shape transition during the pulling experiment and has two stable solutions for each $z_p$ within a small range. This appears as a turning point in the continuation arc, and therefore normal continuation fails (see §C.3.1).

The AUTO package [185] is a sophisticated code for numerical bifurcation analysis of algebraic and ODE systems. The package makes use of pseudo-arclength continuation to solve systems of a range of parameters. Furthermore, turning point and bifurcation test functions are evaluated during iteration and upon finding a zero of these functions, Newton iteration is used to precisely locate the critical point. Computation can then be restarted at this point to switch branch or, in two-parameter continuation mode, follow the locus of the turning point. The package also includes a plotting interface. Version 2007p-0.7.3 was used to obtain the solutions presented here.

The numerical solutions of (5.40) used in this chapter were all performed using AUTO driven by Python programs to allow for automated parameter space exploration. Data was exported to facilitate further processing by Python programs.

Imposing the inequality constraint (5.43) using either penalty function proved to be numerically unstable and, for many parameter values, it was not possible to make $\mu$ sufficiently large to satisfy (5.43). Penalty function $\Pi_2$ was found to be generally more useful in obtaining satisfactory solutions. Only solutions satisfying (5.43) to within a tolerance of $10^{-3}$ are shown.

## 5.4 Calculation of free energy

The free energy $F$ associated with a particular membrane shape was defined earlier in (5.2). Using the membrane shapes obtained numerically, numerical integration of (5.2) is used to calculate the membrane free energy. By individually varying the parameters in (5.41) we can explore the free energy profiles of membrane pulling. Consider an experiment where the membrane is clamped by a surface ring at radius $r_f$, and then pulled to a height of $z_p$ by a probe of radius $r_p$. Let $F = F(z_p; r_f, r_p)$ be the free energy of the shape solving (5.12). The function $F$ defines the free energy profile of this pulling experiment as a function of $z_p$.

A more experimentally realistic situation is for the clamping ring at $r_f$ to *not* be fixed. This corresponds to a solid surface-supported lipid bilayer being pulled away from the surface by a probe. The radius $r_f$ is free to vary, governed by a dewetting process at the surface that balances the force applied by the probe. Since $r_f$ can vary, we would expect the force at $r_f$ to ultimately balance the force at $z_p$, at equilibrium. The free energy during of a pulling experiment is a function these boundary conditions, $F = F(z_p, r_f; r_p)$. At equilibrium the membrane shape adopted will minimise free energy, the radius that minimises the free energy $r_f(z_p)$

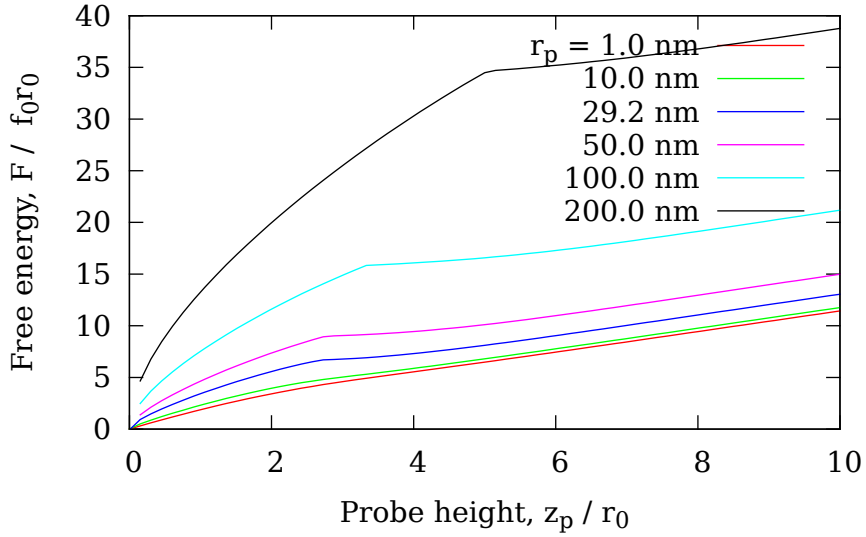


**Figure 5.2:** Minimum of free energy $F(z_p)$ during probe retraction, for various probe radii $r_p$. Represents the equilibrium free energy profile as the membrane is pulled up from the surface. For probe radii larger than the tube radius, that is $r_p \geq r_0$, a first-order transition takes place where the gradient decreases discontinuously. This corresponds to the transformation between a tent-like shape and a shape with a tube. It costs less free energy to increase the tube length than to increase the tent height, and therefore the force of tube elongation is lower.

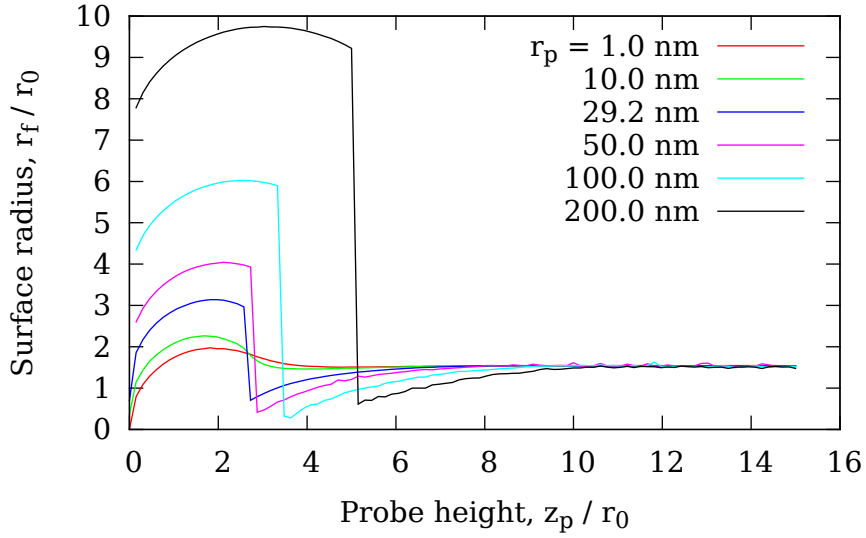


**Figure 5.3:** Surface radius $r_f^*$ of membrane detachment of minimum free energy as $z_p$ is increased, for various probe radii $r_p$. The radius initially increases to accommodate formation of a tent. For $r_p \geq r_0$, the radius makes a dramatic jump down as the tube is formed, but then increases to an asymptotic value $r_f^\infty$. Note that, in $r_0$ units, $\sigma/\kappa = 0.5 r_0$ so $r_f^\infty$ is universal relative to $r_0$.

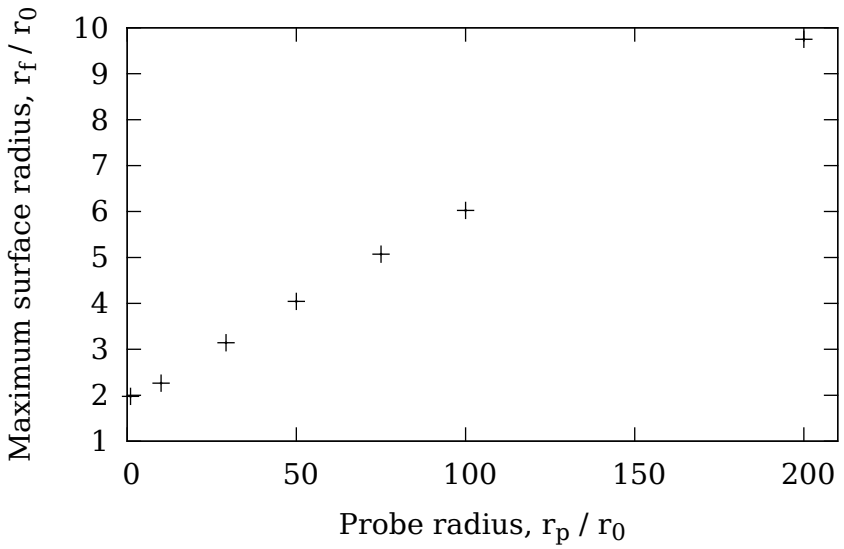


**Figure 5.4:** The maximum surface radius of membrane detachment during the course of pull scales linearly as a function of probe radius.

can be determined by solving

$$\frac{\partial F}{\partial r_f} = 0 \quad \text{and} \quad \frac{\partial^2 F}{\partial r_f^2} > 0. \tag{5.48}$$

Since, $r_f$ is now a function of $z_p$, the free energy during the pulling experiment is a function of $z_p$ only; $F = F(z_p)$. $F$ is shown in Figure 5.2, and the function $r_f(z_p)$ is shown in Figure 5.3, for various probe radii $r_p$.

During the course of the pull, $r_f^*$ increases to a maximum, shown in Figure 5.4 as a function of $r_p$. For probe radii of similar size to or larger than the tube radius $r_0$, a discontinuous drop in surface radius occurs. For all $r_p$, the surface radius approaches a universal value $1.57r_0$. This value most likely minimises the curvature energy in the surface attachment where the membrane must bend from the horizontal to the vertical.

## 5.5 Calculation of force-distance curve

A conservative force is the gradient of a scalar potential field. In general

$$f = -\nabla\phi \tag{5.49}$$

where $f$ is a vector and $\nabla$ is the gradient vector operator. The force required to pull up a membrane from a surface can therefore be calculated from the free

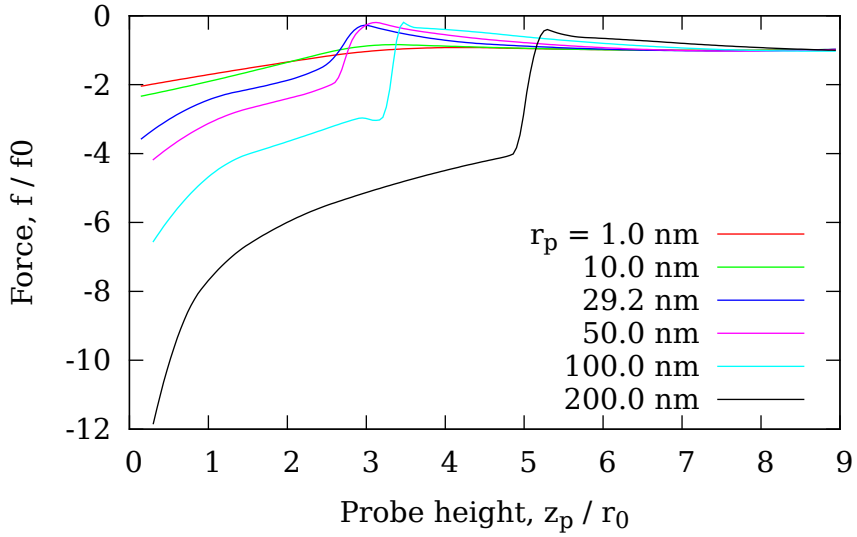


**Figure 5.5:** Force at probe as $z_p$ during pulling experiment, obtained by differentiating the free energy $F$ in Figure 5.2. For $r_p \geq r_0$, the tube formation is apparent as a rapid decrease in force.

energy profile $F(z_p, r_p)$

$$f_{z_p} = -\frac{\partial F(z_p, r_p)}{\partial z_p} \tag{5.50}$$

The force profile as $z_p$ is increased is shown in Figure 5.5 and is analogous to a force curve obtained using AFM. However, the theoretical curve here is based on a minimum free energy equilibrium principle, while the AFM experiment almost certainly is nonequilibrium due to the finite velocity of probe retraction. Consideration of velocity dependent effects is given in §5.8. A consequence of this is that inside parameter regions where two stable solutions exist, for the theoretical curve the solution with the lower energy is chosen. In the experiment it may be that, due to frictional forces (e.g. in lipid redistribution), the membrane maintains a stable configuration of higher energy, despite a minimal energy configuration existing.

## 5.6 Zero pressure solutions

Solutions of (5.40) for increasing probe height $z_p$ and various probe radii $r_p$ are shown in Figure 5.6. The surface radius $r_f$ is determined per solution by optimising for minimum free energy (see $r_f^*$ in §5.4). Each pull begins by forming a 'tent' like shape, where $z$ is a monotonic decreasing function of $r$. This is characterised by a large surface radius $r_f$ (Figure 5.3). After reaching a height particular to the probe radius, the surface radius drops and a tube begins to form with radius $r_0$. When $r_p \geq r_0$ this drop is discontinuous and manifests on the free energy diagram

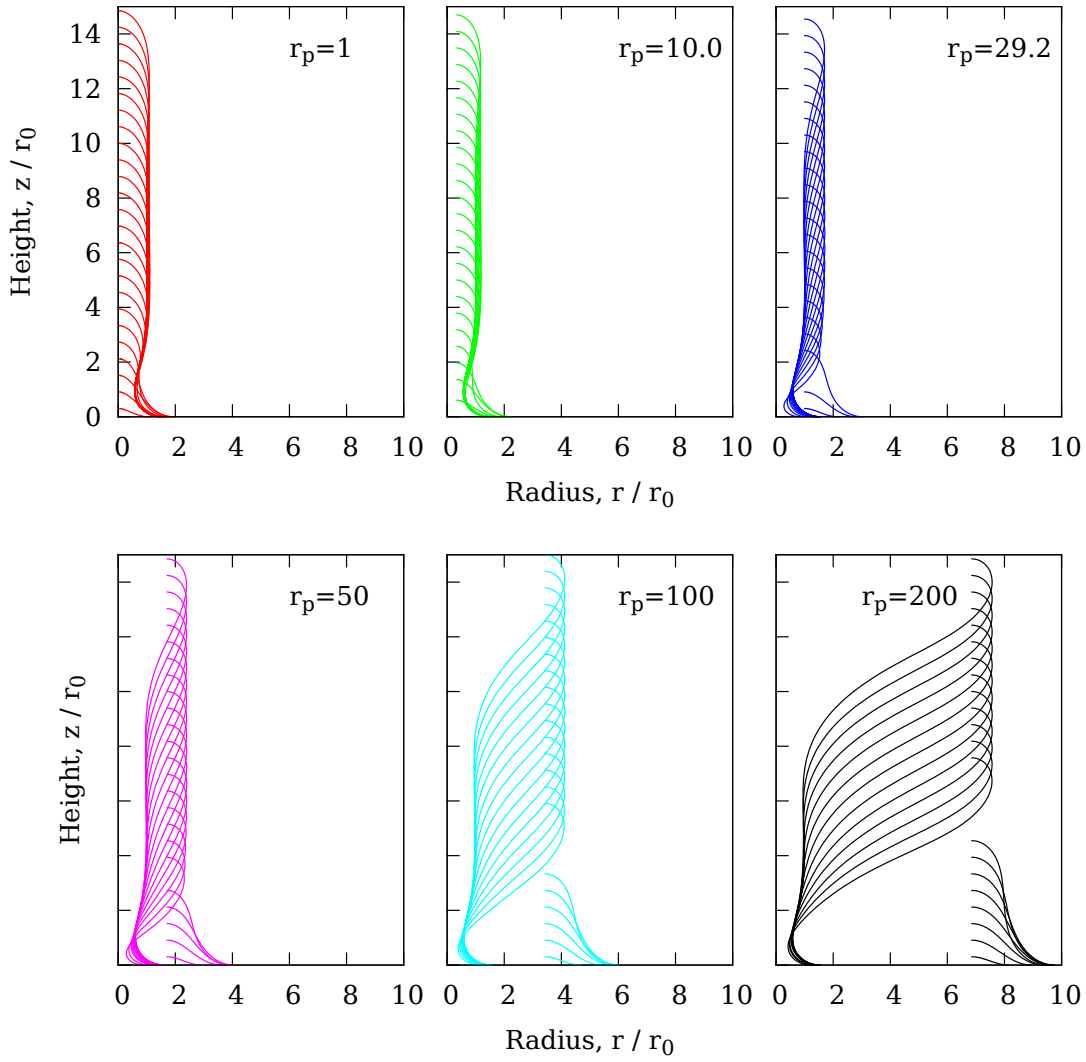


**Figure 5.6:** Membrane shape solutions during pulling experiment with $P = 0$, for various probe radii $r_p$ (in nm). For all $r_p$ the radius of the tube portion is $r_0$. Prior to forming a tube a tent-shaped structure is formed; for larger $r_p$ the tent formed is larger.

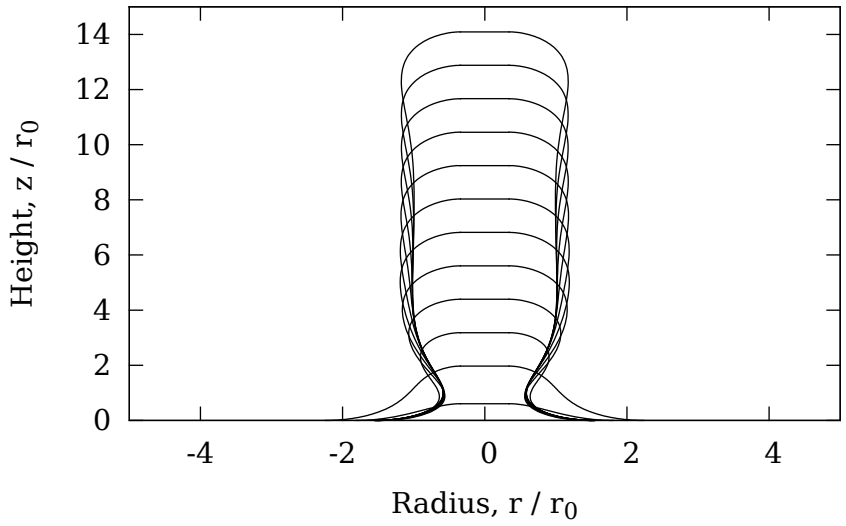


**Figure 5.7:** Membrane shape solutions during pulling experiment with $P = 0$ for $r_p = 10$ nm. In this figure the contour has been reflected about $r = 0$ to aid visualisation.

as a discontinuous change of gradient Figure 5.2. In the force curve this is clearly visible as a sharp step to lower attractive force.

Further increase in height extends the tube and no further shape changes take place. The force increases immediately after tube formation, reaching an asymptotic value $f^\infty = f_0$.

The maximum surface radius reached while in the tent configuration is proportional to $r_p$ (Figure 5.4). The tube length is shorter for larger $r_p$ due to the longer smooth excursion made by the contour between $r_0$ and $r_p$.

## 5.7 Finite pressure solutions

When a bilayer is formed on a surface, a thin layer of water, around 0.5–1.5 nm separates the bilayer and surface. This is thought to allow the bilayer to maintain fluidity [186]. It is also provides a means for fluid flow into and out of a volume $V$ enclosed by a membrane segment pulled up by an AFM probe. The other route for fluid flow is membrane permeation, but this is slow [187]. The rate of fluid flow into the membrane segment controls $V$. The solutions for $P = 0$ found in §5.6 effectively allow for unbounded and instantaneous fluid flow. Consequently, increase in $V$ has no cost and therefore it must be that $P = 0$. Contrarily, if the rate of fluid flow is limited then the $V$ containing term in the free energy $F$ becomes nonzero and a pressure $P \neq 0$ develops.

In solving (5.40), we can either fix $P$ at some predetermined value and calculate $V$, or impose some $V$ and solve for $P$. In the experiment under investigation here,

$P$ is an unknown quantity. This is unlike most vesicle tube pulling experiments where $P$ is held fixed by micropipette suction. We therefore introduce an approximation for the rate of fluid flow into the pulled membrane segment, and allow this to determine $V(t)$.

Solutions for $P \neq 0$ are shown in Figure 5.8 and Figure 5.9, but unfortunately it was not possible to minimise the free energy with respect to the parameter $r_f$, and so force curves were not obtained.

### 5.7.1 Plane Poiseuille flow

To attempt to calculate the rate of luid flow into the membrane segment, we consider the fluid flowing in the space between the surface bilayer and solid-support. A reasonable model for this situation is fluid flow between two parallel planes. Steady flow between two parallel planes with separation $h$, moving with constant relative velocity $u$ and with a pressure gradient parallel to the planes, is known as Hagen-Poiseuille flow. When the planes are both fixed, that is $u = 0$, it is known as plane Poiseuille flow. Following Landau and Lifshitz [188], the Navier-Stokes equations reduce to

$$\frac{\partial^2 v_f}{\partial y^2} = \frac{1}{\eta}\frac{\partial p}{\partial x}, \quad \frac{\partial P}{\partial y} = 0, \tag{5.51}$$

where the $x$-axis is chosen parallel to the planes, and the $y$-axis perpendicular, $\eta$ is the viscosity, $p$ is the pressure and $v_f$ is the fluid velocity in the $x$ direction. Since $p$ is independent of $y$, and $\partial^2 v_f/\partial y^2$ is a function of $y$ only, $dp/dx$ must be constant. Integrating (5.51)

$$v_f = \frac{1}{2\eta}\frac{dp}{dx}y^2 + ay + b. \tag{5.52}$$

After, imposing the boundary conditions for plane Poiseuille flow, $v = 0$ at $y = 0$ and $y = h$, we find the parabolic fluid velocity profile

$$v_f = -\frac{1}{2\eta}\frac{dp}{dx}y(y-h), \tag{5.53}$$

and taking the mean velocity

$$\left\langle v_f \right\rangle = \frac{1}{h}\int_0^h v_f\, dy = -\frac{h^2}{12\eta}\frac{dp}{dx}. \tag{5.54}$$

Plane Poiseuille flow could be used to model the inflow of fluid into a forming membrane tube from a surface bilayer, where the surface-supported bilayer and the solid support are the parallel planes. Although the bilayer is not fixed with

$u = 0$, the rate of area increase is small enough that it is fair to assume it to be so. In the tube phase, the rate of area increase is approximately

$$\frac{dA}{dt} \approx 2\pi r_0 v_p, \tag{5.55}$$

where $v_p$ is the velocity of probe retraction. The velocity of membrane flow at any point on a circle of radius $r$ is

$$v_m = \frac{1}{2\pi r_f}\frac{dA}{dt} = \frac{r_0 v_p}{r}. \tag{5.56}$$

At a radius of $r = 10r_0$ and a pulling speed of $v_p = 500\,\text{nm/s}$, $v_m = 50\,\text{nm/s}$. At smaller radii, the assumption becomes less valid, with $v_m$ maximum when $r = r_f$, the radius of membrane detachment from the surface. Nevertheless, plane Poiseuille flow provides a convenient approximation of the fluid flow into the membrane segment. However, the water layer trapped between bilayer and surface has a different viscosity to bulk water, and is difficult to measure directly. Therefore we choose to encapsulate the viscosity in an semi-arbitrarily selected prefactor.

### 5.7.2 Fluid flow

Assuming Poiseuille flow into the membrane segment detached from the surface, the fluid velocity depends on the pressure differential $P$. The rate of volume of increase is then

$$\begin{aligned}\dot{V} &= 2\pi\left\langle v_f \right\rangle rh \\ &= -\frac{\pi r h^3}{6\eta}\frac{dp}{dx} \\ &= -\frac{\pi r h^3}{6\eta}P.\end{aligned} \tag{5.57}$$

However, as noted in §5.7.1, the viscosity $\eta$ of the trapped water is difficult to measure, and furthermore $r$ is variable during the pull complicating the calculation. We therefore simply encapsulate these factors into a single prefactor

$$\dot{V} = -\alpha P. \tag{5.58}$$

When numerically solving (5.40), solutions are obtained at discrete $z_p$ points. Given $v_p$ is constant, this corresponds to discrete time points. For each time point $t$, (5.58) is solved by the Euler method to find $V(t)$. The pressure $P(t)$ is then found

by solving (5.40) and numerically minimising $|V - V(t)|$.

An order of magnitude range for $\alpha$ is estimated by calculating $\alpha^*$, the value of $\alpha$ that would be required to obtain the $V(t)$ resulting from the $P = 0$ solutions, if the pressure was $P = \sigma/r_f$.

## 5.8 Dissipation

In all of the above, equilibration is assumed to have occurred for the membrane and the fluid contained therein. However, the retraction of probe caused fluid to flow into the membrane space, as well as lipid flows within the membrane itself. These nonequilibrium effects increase the force required to deform the membrane.

We can make a crude estimate of force required to move the membrane through the fluid using Stoke's law, making the assumption that a tube of radius $r_0$ has a similar drag in the fluid as a sphere of the same radius

$$f_S = 6\pi\eta_f r_0 v_p. \tag{5.59}$$

For a typical $r_0 = 30$ nm, and using the viscosity of water for the containing fluid $\eta_f = 10^{-3}\,\mathrm{N\,s/m^2}$, we find $f_S = 3 \times 10^{-5}$ pN, which is completely negligible.

The two-dimensional viscosity of the membrane also causes energy dissipation. For an incompressible fluid of density $\rho$, the total kinetic energy is [188]

$$E_{\mathrm{kin}} = \frac{\rho}{2}\int v^2 dV. \tag{5.60}$$

The time derivative of $E_{\mathrm{kin}}$, the dissipation, is always negative

$$\dot{E}_{\mathrm{kin}} = -2\pi\eta_m \int_{r_f}^{\infty} \left(\frac{\partial v_m}{\partial r}\right)^2 r\, dr, \tag{5.61}$$

in axisymmetric coordinates, where $\eta_m$ is membrane two-dimensional shear viscosity. The force required to overcome this viscous energy dissipation is

$$f_m = \dot{E}_{\mathrm{kin}}/v_p \tag{5.62}$$

Taking for the membrane velocity $v_m$ from (5.56)

$$\dot{E}_{\mathrm{kin}} = -\pi\eta_m \frac{r_0^2 v_p^2}{r_f^2}, \tag{5.63}$$

and the dissipation force is $f_m \approx 0.001\,\mathrm{fN}$, using $\eta_m = 10^{-10}\mathrm{N\,s/m}$ for the membrane

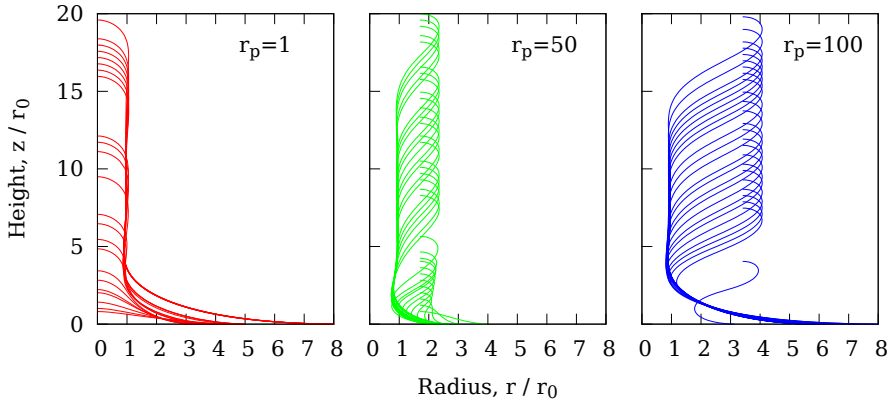


**(a)** $\alpha = 250$

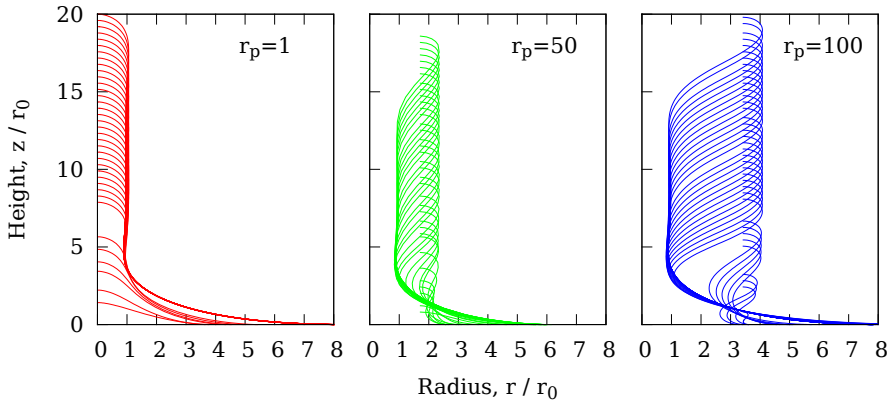


**(b)** $\alpha = 500$

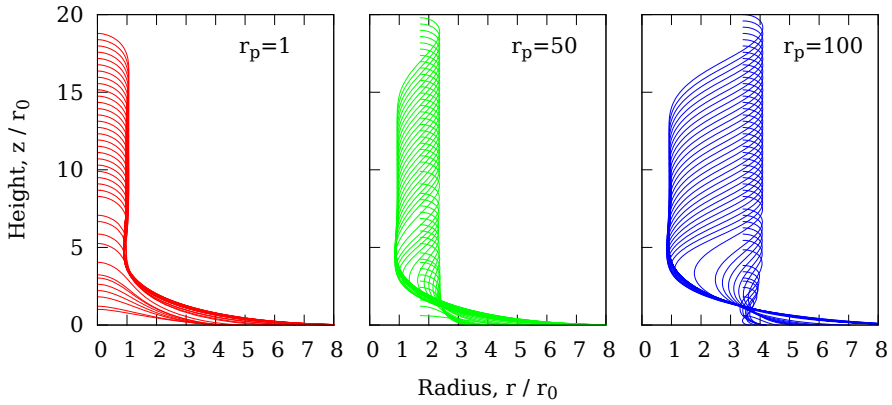


**(c)** $\alpha = 1000$

**Figure 5.8:** Caption on next page.

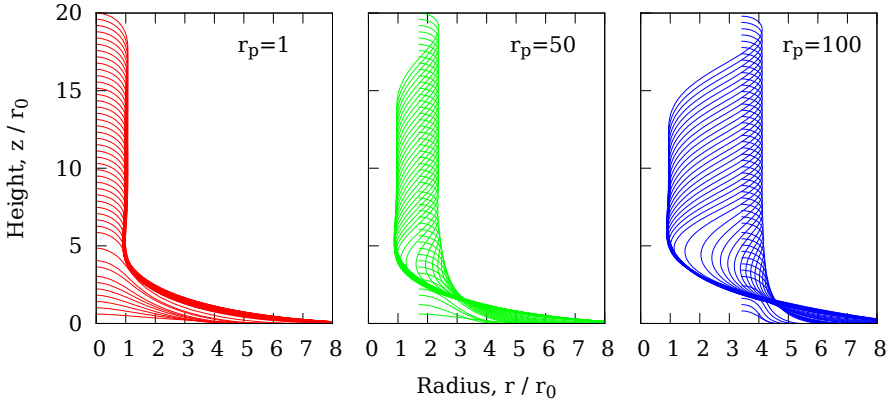


**(a)** $\alpha = 2000$

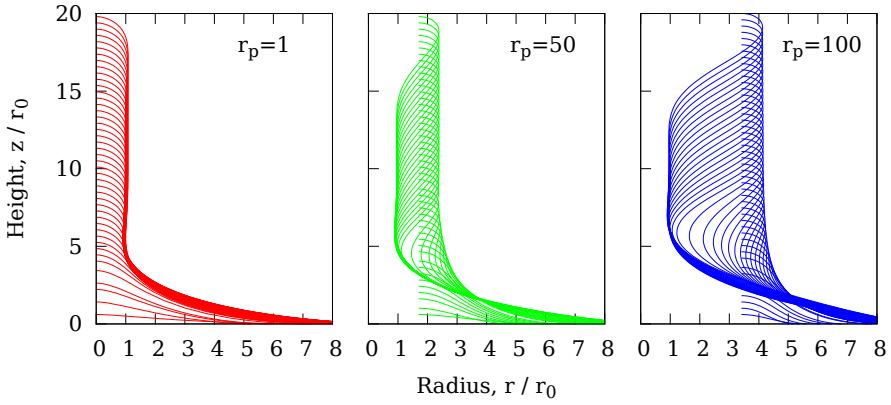


**(b)** $\alpha = 3000$

**Figure 5.9:** Shape of membrane during pulls with $\alpha = 250$, 500 and 1000, $r_p = 100$ nm and $r_f = 10r_0$. Only those solutions where it was possible to impose the inequality constraint (5.43) are shown here. The constant $\alpha$ controls the rate of volume increase for a given $P$. In all cases the tube radius remains fixed at $r_0$. The increased volume with larger $\alpha$ appears to be contained in the tent shape beneath the tube. Note that, due to numerical difficulties, $F$ has not been minimised with respect to $r_f$ for these solutions, and so these shapes cannot strictly be taken as a prediction of the equilibrium membrane shapes.

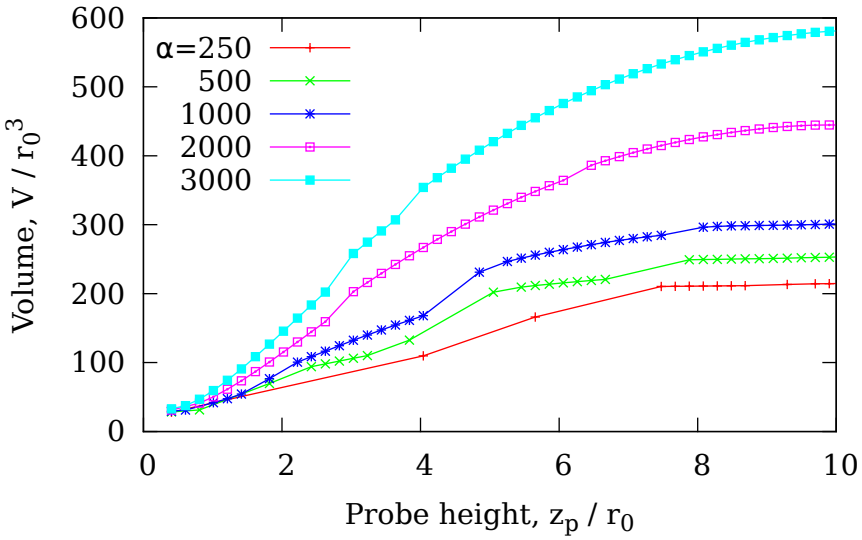


**Figure 5.10:** Volume $V$ of the segment of membrane detached from the surface as function of $z_p$, with $r_f = 10r_0$, $r_p = 100\,\text{nm}$ and $\alpha = 500$. As is expected $V$ increases more rapidly with larger $\alpha$, although not proportionally so. This indicates that the magnitude of $P$ is larger for smaller $\alpha$, which increases $\dot{V}$.

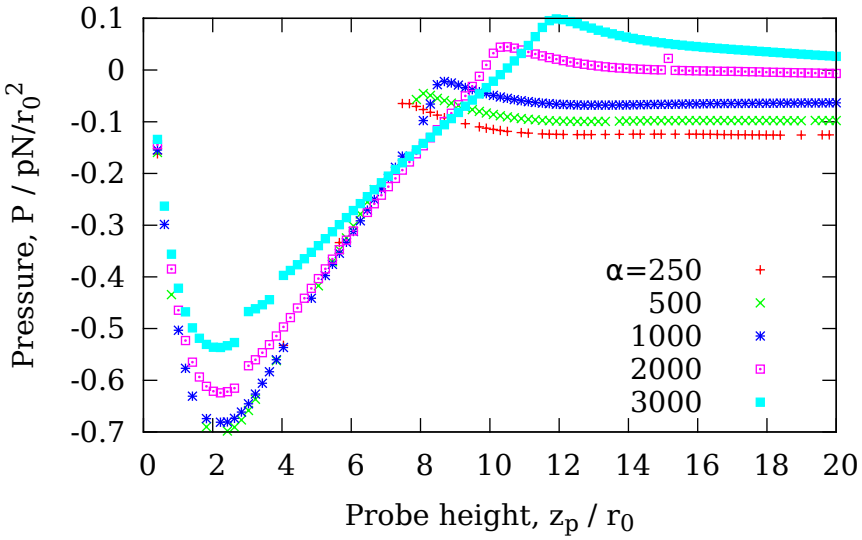


**Figure 5.11:** Pressure $P$ in the segment of membrane detached from the surface as function of $z_p$, with $r_f = 10r_0$, $r_p = 100\,\text{nm}$ and $\alpha = 500$. During the tent phase, at small $z_p$, $P$ drops rapidly. This is intuitively correct as the tent requires a large volume increase in a short time, which is not possible when the flow is restricted. At greater $z_p$, $V$ increases more slowly since only a tube of radius $r_0$ is extended. The asymptotic $P$ is smaller for larger $\alpha$ as expected due to the higher flow, and tends to a negative value, indicating that $\dot{V} < 2\pi r_0 v_p$.

shear viscosity [189]. This is entirely negligible, for the range of forces investigated here, and can be safely ignored.

The result that dissipation can be ignored is in agreement with the observation by Maeda et al. that the features on force curves are not velocity dependent over the range $v_p$ = 0.5–50 μm/s [2].

# 6

# Analysing atomic force microscopy force curve data

In this chapter the typical form and interpretation of atomic force microscope (AFM) force curve data are discussed, in addition to the analysis methods used to provide data for Chapter 7.

## 6.1 Preprocessing

Two probe position coordinates are in common usage in describing AFM data. In extension coordinates $\zeta$ is the distance travelled by the piezoelectric actuator towards the surface. In separation coordinates $z$ is the position of the probe relative to the initial point of contact with the surface. The AFM produces data in the form of voltage difference $V_d$ across the photo-diode detector indicating deflection of the cantilever and voltage difference $V_\zeta$ across the stage $\zeta$-piezo (see §3.1 for a discussion of AFM design and operation – the $z$-direction is normal to the sample surface). The distance $\zeta$ is trivially calculated from $V_\zeta$ as the extension of the piezo for a given voltage[1] and is found by imaging calibration samples of known height.

Converting $V_d$ to a force $f$ is more complex as it depends on the cantilever and the location of the laser spot focus on top of the cantilever, as well as the spring constant $k$ of the cantilever. It is necessary to know the change in $V_d$ for a given change in the deflection $d$ of the cantilever end. The ratio $\delta = d/V_d$ is called

[1]The piezo is assumed to extend linearly with voltage. This is a reasonable approximation for small extensions. During the calibration procedure, the range of the piezo is limited to exclude extensions for which the voltage relationship becomes nonlinear. Furthermore, the AFM electronics internally apply corrections to improve linearity.

the deflection sensitivity and has units nm/V. Once $\zeta$ is known, the deflection sensitivity may be determined by producing a force curve against a hard surface (that is, significantly stiffer than the cantilever), such as mica or glass. The gradient of the portion of the curve where the probe is in contact with the surface is $-1/\delta$, as the change in deflection of the cantilever is precisely the change in extension of the piezo.

The cantilever $k$ may be determined by a number of the methods, the simplest of which is the thermal noise method [145]. The cantilever is an elastic beam and, for small deflections $d$, the potential energy stored is

$$E = \frac{1}{2}kd^2. \tag{6.1}$$

The equipartition theorem [190] states that, at equilibrium

$$\frac{1}{2}k_BT = \frac{1}{2}k\left\langle d^2\right\rangle. \tag{6.2}$$

where $k_B$ is the Boltzmann constant and $T$ is the absolute temperature. Hence, knowing the mean-square deflection of the cantilever allows the spring constant to be calculated using

$$k = \frac{4}{3}\frac{k_BT}{\langle d^2\rangle} \tag{6.3}$$

where the prefactor 4/3 is introduced to account for the use of a laser reflection off the back of the cantilever to measure the deflection [191].

With the cantilever far from the surface, in air, thermal vibrations are measured for a short period of time[2]. A power spectrum plot will show sharp Lorentzian peaks at the resonance frequency (and also, the harmonic frequencies), and the integral of the power spectrum is the mean-squared fluctuation of the cantilever deflection [192]. This representation allows the easy exclusion of other resonances and background noise. If $P$ is the area under the resonance peak then the spring constant is given by [145]

$$k = k_BT/P. \tag{6.4}$$

Once $k$ is known, the force exerted by the cantilever is given by

$$f = V_d\delta k. \tag{6.5}$$

Due to the sensitivity of the instrument, the data is highly susceptible to the thermal drift of instrument components relative to each other. This results in a sequence of force curves having steadily increasing or decreasing absolute $V_d$

[2]Including enough samples to more-than satisfy the Nyquist theorem.

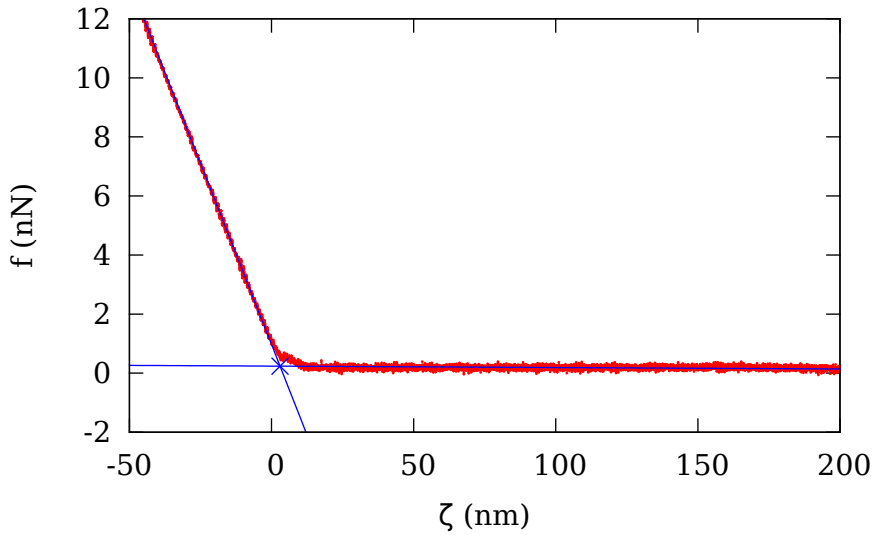


**Figure 6.1:** Estimation of contact point as if sample was irreversibly compressed. The trace shows the force exerted on the cantilever as the $z$-piezo is moved; positive force corresponds to an upward deflection of the cantilever. Lines fitted to the fully approached and fully extended parts meet at the contact point, marked with a cross.

and $V_\zeta$ offsets. This makes direct comparison of the curves problematic. It is therefore necessary to mutually align a force curve dataset. One method for curve alignment is to zero the probe-surface contact point on each curve. However, as is shown in Figure 6.2, soft samples, including lipid bilayers, are compliant when force is applied with the probe meaning the contact point is less well-defined than on a hard sample.

Fortunately, a contact point as if the sample was irreversibly fully compressed can still be inferred from the curve. Such a contact point is the intersection of a line extended from the high force, constant gradient portion of the curve and a line extending from the far from the surface baseline portion. Care must be taken to ensure nonlinear parts and features are excluded when fitting these lines. Subtracting the estimated contact points from each curve corrects for drift in $V_d$ and $V_\zeta$. An example of estimating a contact point is shown in Figure 6.1.

There is one further drift which occurs particularly noticeably when employing a delay between reaching maximum application of force to the surface and retracting. During this time the sample will often drift, mostly in the $z$-axis, relative to the probe, resulting in a difference between $V_d$ for the retract and approach curves. This may be corrected either by estimating the contact point as above for retract and approach curves independently, or by using the difference in $V_d$ at maximum approach to correct one or the other.

## 6.2 Force curve taxonomy

Several standard curves arise in force measurements and are shown in Figure 6.2. At standard temperature and pressure, and typical humidities, most surfaces exposed to the atmosphere are coated in a thin layer of water. This gives rise to attractive forces in the approximate range 0.5–5 nN, known as capillary forces, when two of these layers come together [193]. In the AFM environment, this force tends to be much larger than the forces of interest (e.g., unfolding of titin occurs at 150–300 pN [140]), and thus the majority of force measurement experiments take place in solution, in order to eradicate the capillary force. Moreover, most biological systems can only exist in native form in buffer solutions. Therefore, almost all force measurements on biological systems take place in liquids.

## 6.3 Viewer software

Force measurements of molecular interactions with the AFM generally involve the interaction of a few tens of – or even, single – molecules [140]. Consequently, the measured interactions tend to be highly variable as a result of collisions with molecules of the environment and thermal fluctuations. This is in marked contrast with more typical biochemical assays or instruments that provide results that are intrinsically averaged over $\sim 10^{23}$ or more molecules; such systems can be considered to approach the thermodynamic limit. As theoretical considerations invariably only provide predictions for mean averages or distributions, it is necessary to make hundreds of repeat force measurements in order that meaningful data can be extracted.

To facilitate the analysis of large numbers of force measurements a force curve viewing application was developed by the author, called `CurvesView`. A screenshot of the software is shown in Figure 6.3. The purpose of the application is to quickly display a sequence of force measurements, derived from the proprietary data format exported by the instrument. Data may be displayed in separation or extension mode (i.e., $z$ or $\zeta$) and in volts, deflection or force (i.e, $V_d$, $d$ or $f$). A facility is provided allowing the user to make a visual assessment as to the quality the data. Accepted data is flagged for further analysis.

The software is written in Python and uses the Qt toolkit for the graphical user interface (GUI).

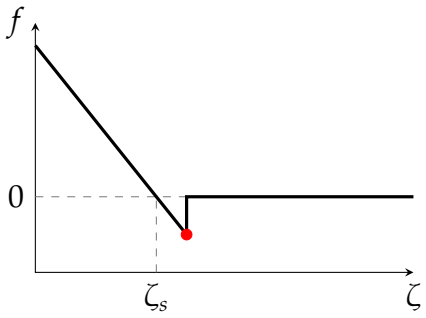


**(a)** Hard surface in air (force-extension). At the right the probe is far from the surface and experiences no deflection. At some small distance from the surface attractive forces are sufficiently strong to pull the probe down into contact (red dot). From that point on the deflection increases linearly.

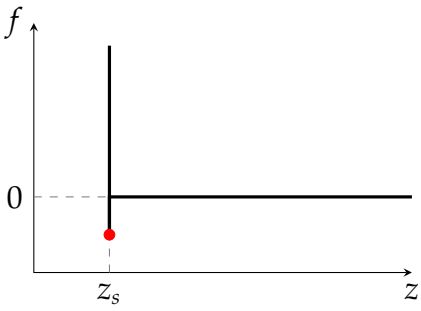


**(b)** Hard surface in air (force-separation). As in (a) but showing the distance between probe and surface.

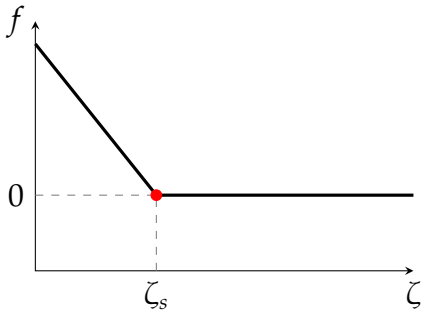


**(c)** Hard surface in liquid (force-extension). When the probe approaches the surface in liquid the capillary force is eliminated and consequently so is the jump into contact.

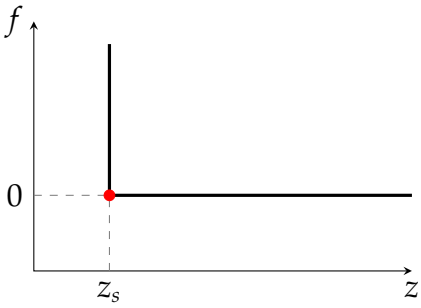


**(d)** Hard surface in liquid (force-separation). As in (c) but showing the distance between probe and surface.

**Figure 6.2:** Approach forces curves in various circumstances. On the left side, the distance coordinate $\zeta$ is the distance the piezo moves. On the right size, $\zeta$ has been converted to the separation between probe and surface $z$. In each case, the red dot indicates the point where the probe first makes/leaves contact with the surface. (Figure continues next page).

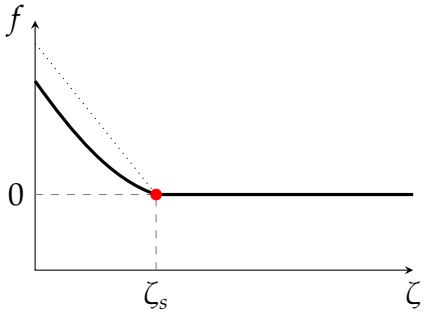


**(e)** Soft surface in solution (force-extension). When the probe is pushed against a soft surface, the force is shared between the compliant surface and the cantilever. Hence, the force shown on the curve is less than that for a hard surface.

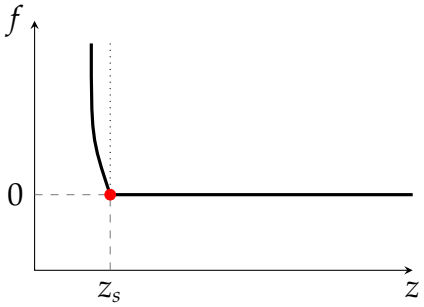


**(f)** Soft surface in solution (force-separation). As in (e) but showing the distance between probe and surface. Strictly, the graph does not show separation, and in fact shows the probe position relative to the initial contact point. In the standard nomenclature, such coordinates are called separation.

**Figure 6.2:** Figure continued from previous page.

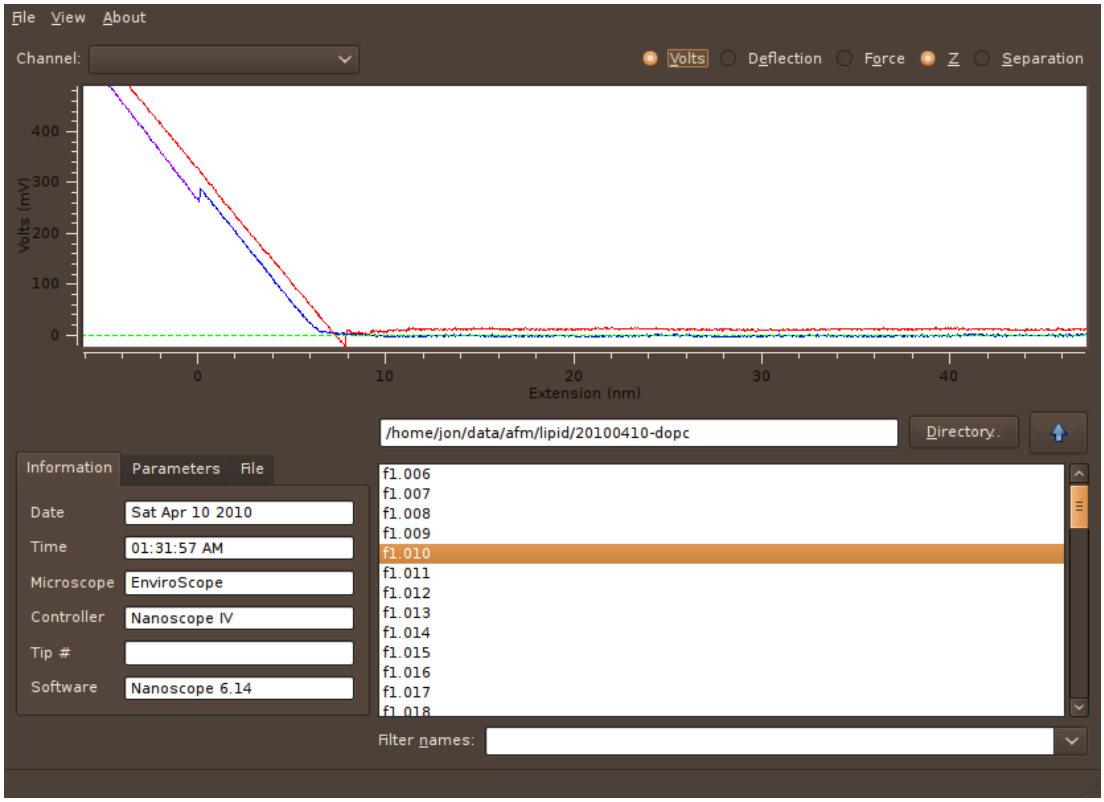


**Figure 6.3:** Screenshot showing the interface of `CurvesView`. The software allows rapid visualisation of force curve measurements in proprietary format. It allows visual assessment of the quality and flagging for further analysis. Here an approach (blue) and retract (red) force curve against a surface-supported lipid bilayer is shown.

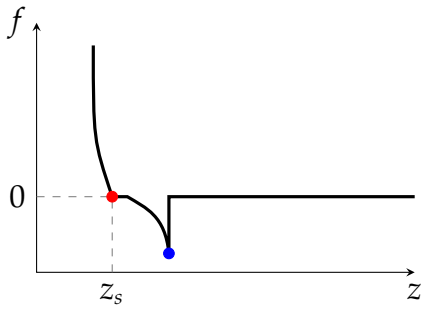


**Figure 6.4:** Extension of a polymer, or unfolding of a protein, bound to surface is well-described by the worm-like chain equation $F(z) = (k_B T/b)[0.25(1 - z/L)^{-2} - 0.25 + z/L]$, as shown with, for example, titin [140]. Note the force peak is asymmetrical.

## 6.4 Automatic analysis

After initial visual inspection to eliminate poorly defined data from a set of force curves, it is necessary to extract quantitative features. As noted in §6.3, the stochastic nature of the individual events recorded in force curves requires statistical interpretation over samples of tens or hundreds of curves. To facilitate this analysis a collection of scripts was developed by the author, called `Curves`, for the automatic processing and feature extraction of large sets of force curves. `Curves` includes scripts to convert proprietary format files to text format, perform curve alignment and drift correction, peak-finding and step-finding.

The software is written in Python and makes use of the NumPy and SciPy libraries for numerical processing, and the Machine Learning PYthon (mlpy) [194] library for wavelet transforms.

### 6.4.1 Peak-finding

Algorithms that locate peaks in signals by finding where the first derivative changes sign generally tend to be unreliable for noisy signals with unusually shaped peaks such as AFM force curves (e.g., the unfolding of a protein type peak shown in the diagram in Figure 6.4). A more robust algorithm is the continuous wavelet transform (CWT) method, originally developed for locating peaks in mass spectrometry data. The CWT method compares the signal $s(t)$ with a so-called 'mother'-wavelet transformed in both space and scale. A wavelet $\psi(t)$ is a short wave with the property[3]

$$\int_{\infty}^{\infty} \psi(t)\, dt = 0. \tag{6.6}$$

[3]Although the wavelet is defined in terms of time $t$ and the force curve data is in terms of distance $z$, the constant retraction velocity $v$ relates the two by $t = z/v$.

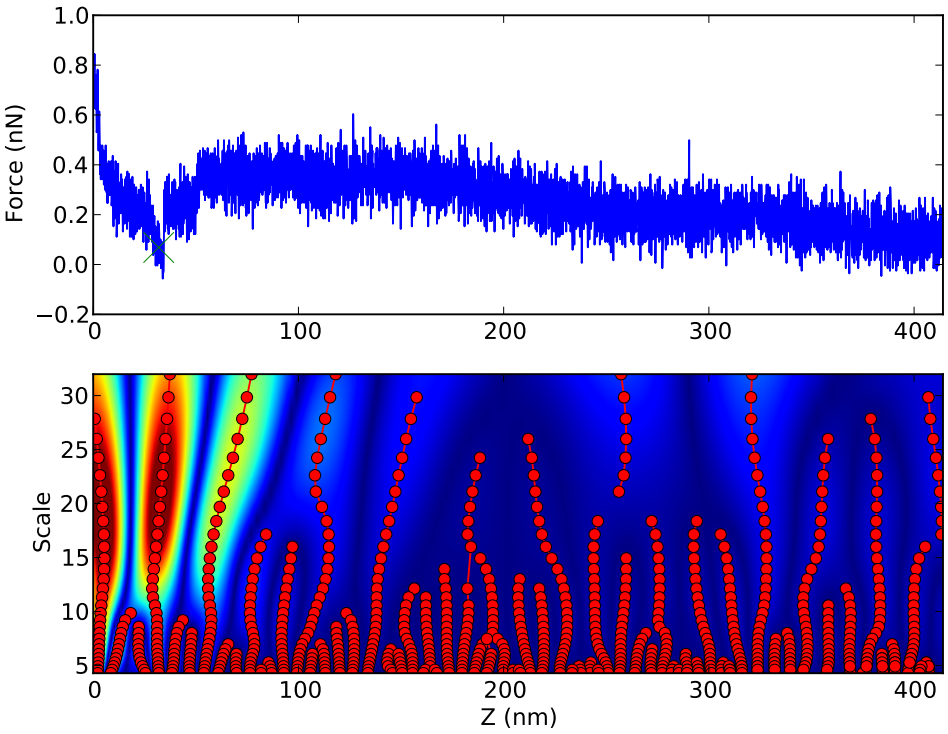


**Figure 6.5:** Peak finding using the continuous wavelet transform (CWT) method. (top) A segment of the retraction signal showing a distinct peak around 40 nm, followed shortly by a step. The identified peak is marked by a cross. (bottom) A contour plot of the CWT coefficients with a fourth-order derivative of a Gaussian wavelet; scale is shown as the $y$-axis. Larger coefficients are shown in red; smaller in blue. The circles trace out 'ridges' by following nearby local maxima at increasing scale. Only those ridges meeting a signal-to-noise ratio threshold are identified as peaks, as discussed in main text.

The CWT is defined as [195]

$$C(a,b) = \int_{\infty}^{\infty} s(t)\psi_{a,b}(t)\,dt, \tag{6.7}$$

where the wavelet is rescaled by

$$\psi_{a,b}(t) = \frac{1}{\sqrt{a}}\psi\left(\frac{t-b}{a}\right), \quad a > 0. \tag{6.8}$$

Applying the CWT at a given scale gives a coefficient for each input data point. A two-dimensional map is produced by repeating the transform over a range of scales. This provides an intuitive false-colour visualisation of how the signal matches the wavelet at different scales and positions, as shown in Figure 6.5.

By trial and error, the derivative of a Gaussian wavelet of order 4 has proved

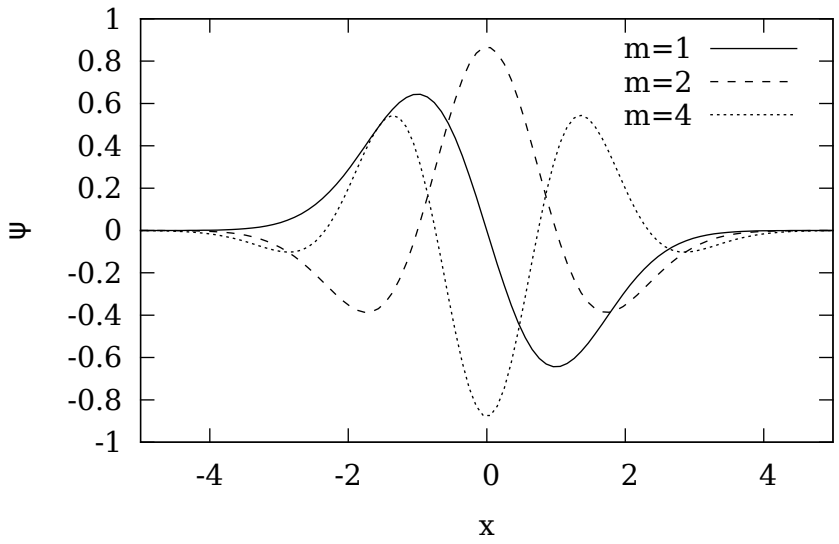


**Figure 6.6:** Derivative of Gaussian (DOG) wavelet used for peak finding. The DOG wavelet is defined in (6.9) and is shown for orders $m = 1$, 2 and 4. For peak finding the $m = 4$ wavelet is used; for step-finding the $m = 1$ wavelet is used.

useful for AFM force curve peak finding. The definition of the derivative of a Gaussian wavelet of order $m$ is [195]

$$\psi(t) = \frac{(-1)^{m+1}}{\sqrt{\Gamma\left(m + \frac{1}{2}\right)}} \frac{d^m}{dt^m}\left(e^{-t^2/2}\right). \tag{6.9}$$

A particular peak will match the wavelet best at a particular scale; above and below this scale the CWT coefficients will be less. By thinking of the CWT coefficients (bottom, Figure 6.5) as a three-dimensional (3D) landscape, peaks can be seen to give rise to ridges. The ridges can be traced out by locating all the local maxima at each scale using a sliding window, and then connecting the nearest in each window at each scale. If, repeatedly over a given number of scales, no maxima sufficiently close can be found, then the ridge is terminated.

For any typical curve, many ridges will be found, but most will not correspond to interesting peaks. To identify interesting peaks a signal-to-noise (SNR) ratio threshold is applied, where the SNR of a ridge initiating from $z^*$ at scale zero is defined as

$$\text{SNR} = \frac{\max_i c_i}{\xi_{z^*}}, \tag{6.10}$$

where $c_i$ is the CWT coefficient at scale $i$ along the ridge, and the noise $\xi$ at $z^*$ with window $w$ is defined as

$$\xi_{z^*} = \sqrt{\text{Var}\left\{z : z^* - w \leq z \leq z^* + w\right\}}, \tag{6.11}$$

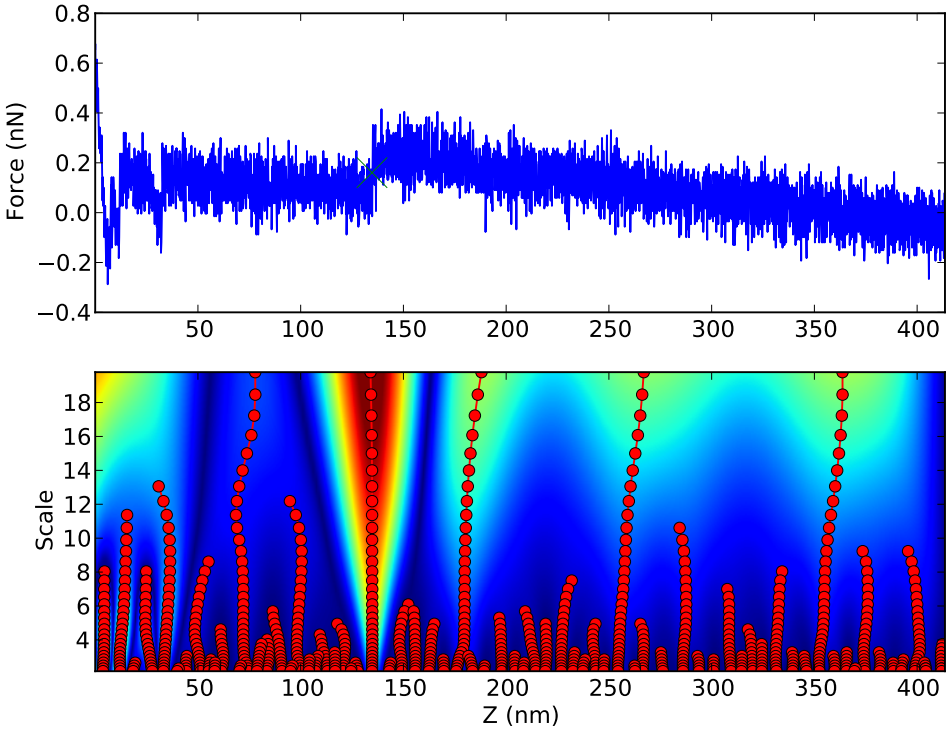


**Figure 6.7:** Step-finding by continuous wavelet transform (CWT) method. (top) A segment of the retraction signal showing a distinct step around 140 nm. The identified step is marked by a cross. (bottom) A contour plot of the CWT coefficients with a first-order derivative of a Gaussian wavelet; scale is shown as the $y$-axis. Larger coefficients are shown in red; smaller in blue. The circles trace out 'ridges' by following nearby local maxima at increasing scale. Only those ridges meeting a signal-to-noise ratio threshold are identified as steps, using the same procedure as for peaks.

where Var indicates taking the variance of the sequence.

### 6.4.2 Step-finding

One method for finding steps in force curve data is to use a Canny edge detection filter [196]. The Canny filter operates by convoluting the first derivative of a Gaussian

$$\frac{-x}{\sigma^3\sqrt{2\pi}}e^{-x^2/2\sigma^2}. \tag{6.12}$$

The result of the convolution is steps become peaks, which can then be located using a standard peak-finding algorithm.

However, since a peak-finding algorithm is still required and is, of course, subject to the same unreliability mentioned in §6.4.1, it has proven useful to employ the CWT peak-finding method directly to locate steps. A suitable wavelet

is the derivative of a Gaussian of order $m = 1$. This wavelet is an odd function, as is an idealised step, and therefore on some scales matches a step in the data well. Figure 6.7 demonstrates the result of this processing.

# 7

# Tube-pulling from solid-supported lipid bilayers with an atomic force microscope

In this chapter experiments where an atomic force microscope (AFM) was used to pull tubes from a lipid bilayer supported on a surface are described. These experiments relate to the theoretical investigations in Chapter 5. The experimental protocol used here is outlined in §3.3.

## 7.1 Characterisation of solid-supported lipid bilayer

AFM was used to verify the efficacy of the solid-supported lipid bilayer (SLB) preparation protocol (described in §3.4). Pure lipid bilayers in the fluid phase are smooth and featureless on the nanometre scale making it difficult to assess the quality of bilayer formation from AFM images (a pure 1,2-dioleoyl-*sn*-glycero-3-phosphocholine (DOPC) bilayer is shown in Figure 7.1). Therefore, a mixed bilayer of 1,2-dipalmitoyl-*sn*-glycero-3-phosphocholine (DPPC) and 1-palmitoyl-2-oleoyl-*sn*-glycero-3-phosphocholine (POPC) was formed and imaged (shown in Figure 7.2). The mixed bilayer image shows a difference in height between DPPC and POPC (height profile shown in Figure 7.3) and, moreover, the segregation into separate phases. This is in agreement with previous work on mixed bilayer phases [197].

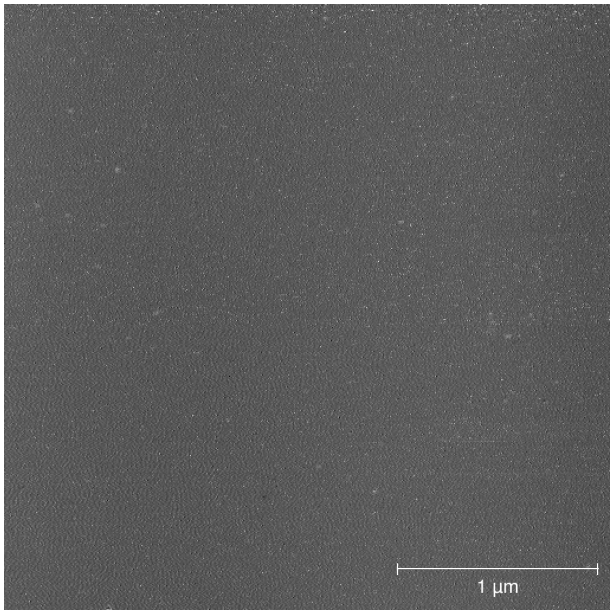


**Figure 7.1:** AFM image of DOPC bilayer. Pure solid-supported bilayers in the liquid disordered phase are featureless and smooth on this scale. The root-mean-square roughness is 0.4 nm.

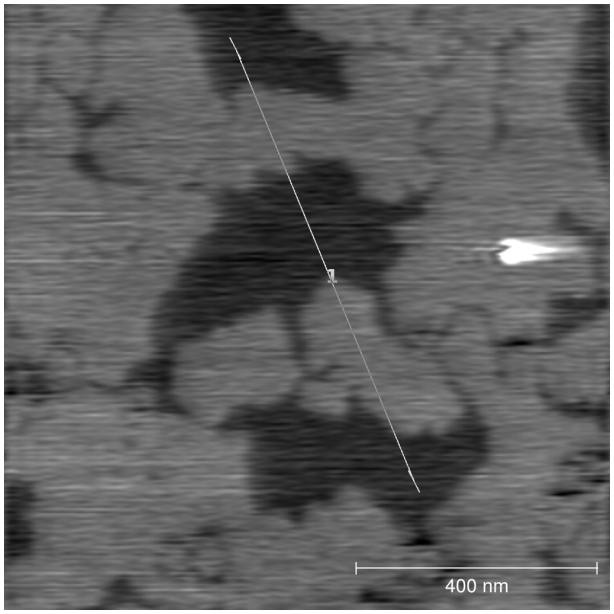


**Figure 7.2:** AFM image of a mixed DPPC-POPC bilayer. At room temperature, DPPC is in the liquid ordered and POPC is in the liquid disordered phase. When mixed together they phase separate and the two domains can be distinguish using AFM due to the lipids in the liquid ordered phase being taller.

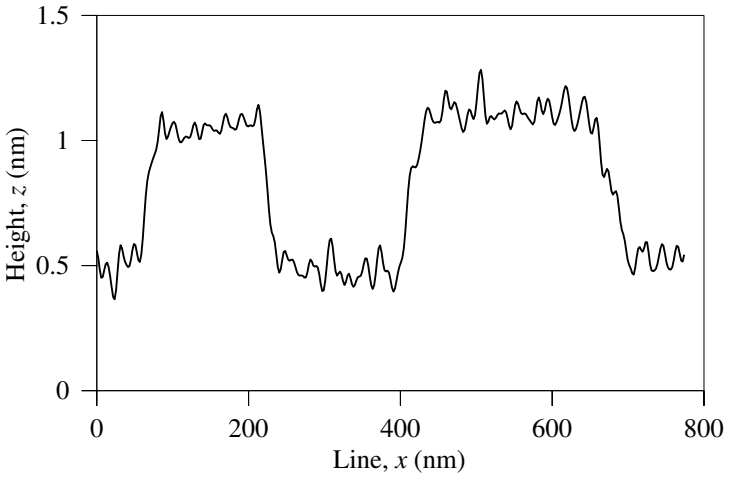


**Figure 7.3:** Line profile of mixed DPPC-POPC bilayer, from the image in Figure 7.2. The liquid ordered and liquid disordered domains are clearly distinguishable, with a height difference of 0.5 nm.

## 7.2 Preparation of AFM probe

Bilayers do not form on very sharp probe tips, unless they are chemically modified, due to the high radius of curvature [3]. Therefore, to enable some degree of bilayer adhesion to the AFM probe, standard sharp silicon nitride probes were ground down according to the protocol specified in §3.3.1. The effect of the grinding procedure on the probe geometry can be assessed by scanning electron microscopy or by imaging well-defined test samples with an AFM. Before and after images of a test sample containing very sharp spikes are shown in Figure 7.4. The spikes are sharper and thinner than the probe and the resulting image is simply images of the probe centred at the spike locations.

It is clear from the dilated probe images in Figure 7.4 that the probe is significantly blunter after grinding. Plotting a line profile through the centre of probe images before and after grinding shows the probe radius approximately doubled. There is a slight asymmetry in the probe images after grinding. This is most likely due to more effective grinding in the direction of the fast axis while raster scanning the probe.

## 7.3 Results

The retract force curve cycle on a SLB results in a number of distinctive features. Approach curves with standard sharp probes often show a step in force as the probe punctures the surface [189, 198]. However, the probe used here has been ground down and is much more blunt that a standard probe. Applying forces of up to 20 nN against the surface does not result in any observable bilayer

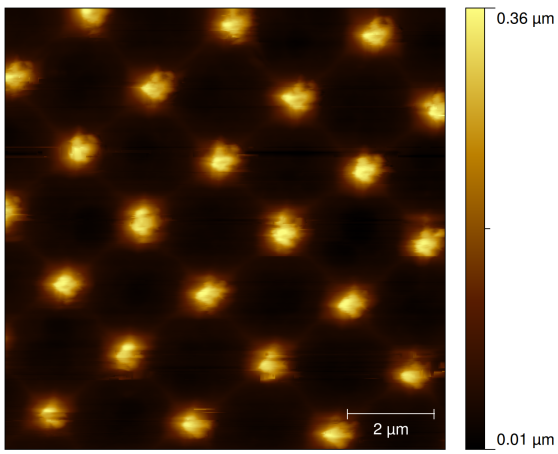


**(a)** Probe images before grinding.

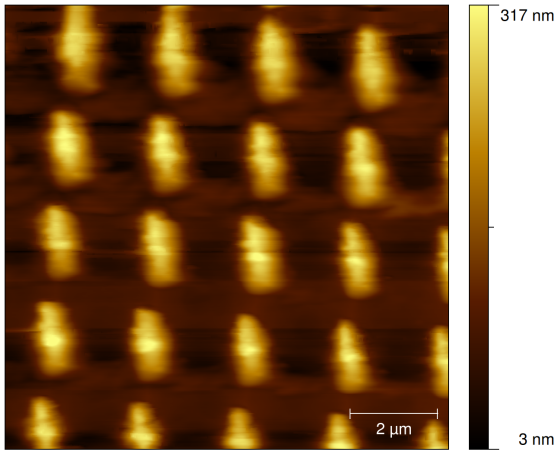


**(b)** Probe images after grinding.

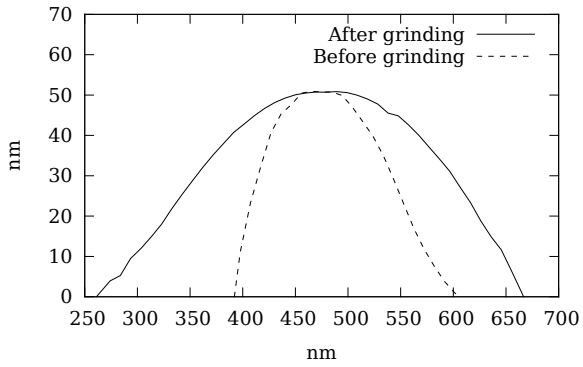


**(c)** Line profile through probe images, before and after grinding.

**Figure 7.4:** Result of grinding the probe tip against a rough diamond surface. (a and b) The image formed by the probe tip scanning over a sample of sharp spikes before and after grinding can be used to infer the change in probe geometry. (c) Line profiles of a image of spike before and after shows the effective probe radius increased from around 50 nm to almost 100 nm.

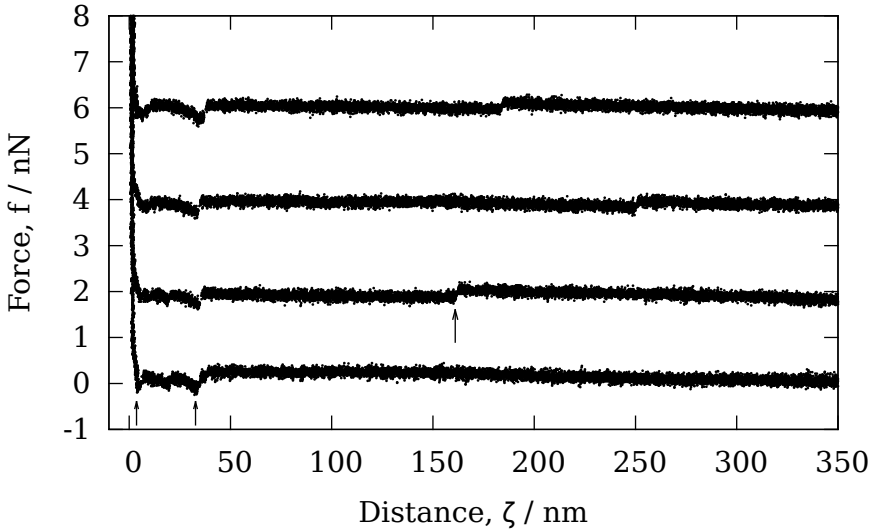


**Figure 7.5:** Typical retract force curves. Three characteristic features appear on these curves which may be attributable to adhesion, tube formation and tube rupture. Arrows show (from left to right) an adhesion feature, a formation feature and a tube rupture feature. All three features do not always appear, together or alone. Curves are offset in the vertical direction for clarity. Retraction velocity was $v_p = 500\,\text{nm/s}$.

rupture. The spring constant of the cantilever was determined by the thermal noise method [145] as $k = 0.23\,\text{N/m}$. On retraction, there is some variability in the features themselves, and particularly in which features are present in each curve. Figure 7.5 shows a selection of typical retraction curves; a more zoomed in view is shown in Figure 7.6. The features which are repeatedly manifest on many curves are apparently connected to the following phenomena:

- Adhesion
- Tube formation
- Tube rupture

Arguments for the association of these features to the above phenomena are made in Chapter 8. Results of analysis of these force curves using the methods of Chapter 6 follow.

### 7.3.1 Adhesion

Most of the forces curves show an attractive force at small distance from the surface, although it is variable. This may be due to bilayer adhesion to the underlying mica support. Pulling at 500 nm/s, the mean force is 164 ± 8 pN and arises at a mean distance of 7.8 ± 0.1 nm ($n = 227$). The range of the force remains

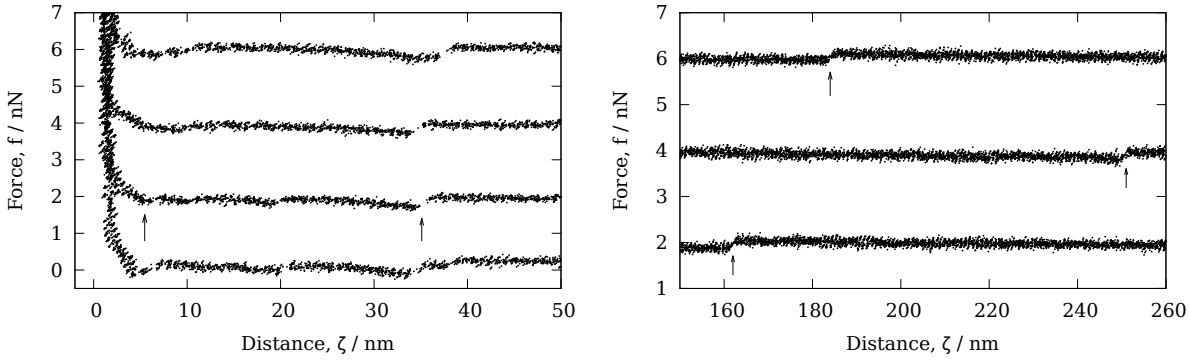


**Figure 7.6:** The retract force curves shown in Figure 7.5, but zoomed in near to the surface (a) and far from the surface (b). The arrows in (a) indicate an adhesion event (left) and a formation event (right). The arrows in (b) indicate tube ruptures.

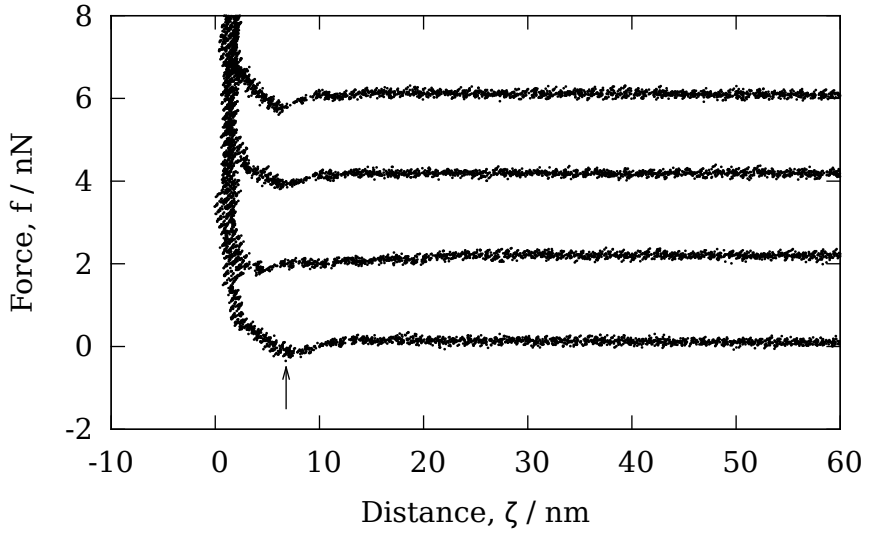


**Figure 7.7:** A selection of retract force curves showing an attractive force peak characteristic of adhesion (indicated by arrow). These particular curves do not show other features, within a retract distance of 120 nm, although curves that do show other features often display a similar characteristic adhesion. Curves are offset in the vertical direction for clarity. Retraction velocity was $v_p = 500$ nm/s.

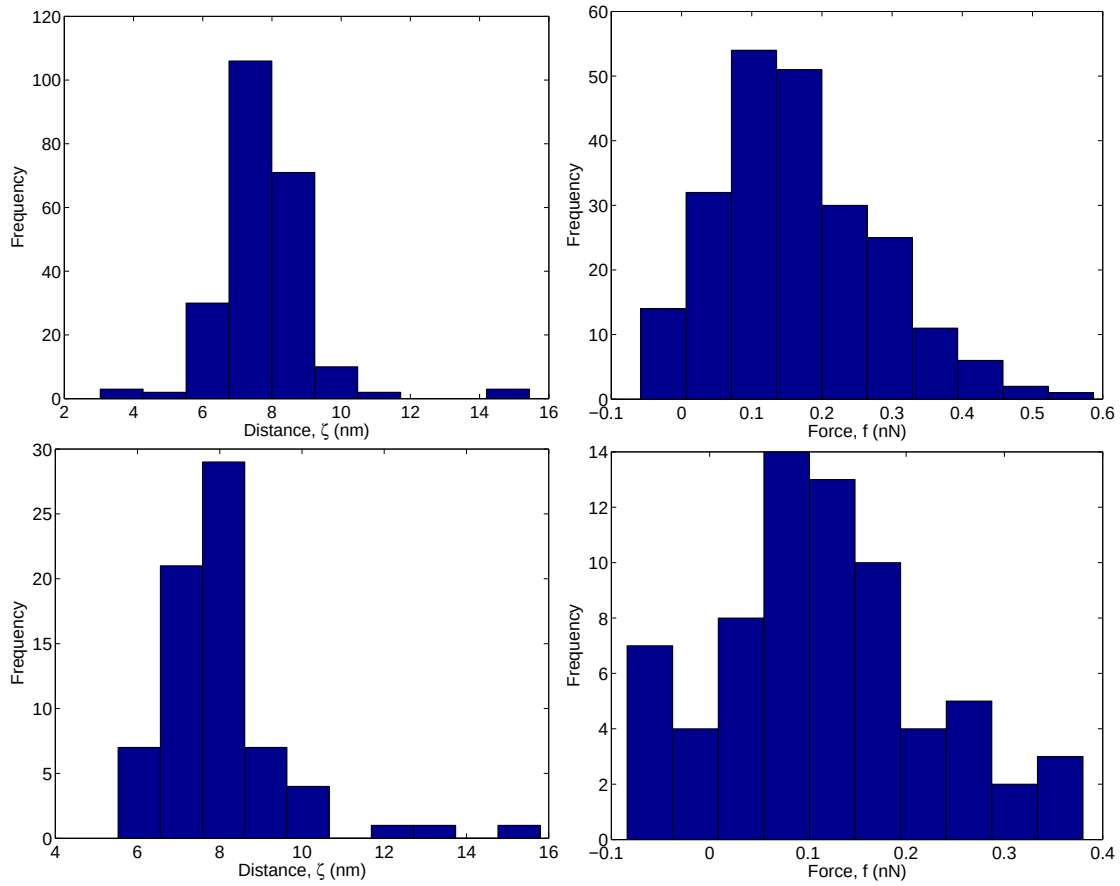


**Figure 7.8:** Peak adhesion force histograms, with $n = 227$ and $v_p = 500\,\text{nm/s}$ (top), and $n = 71$ and $v_p = 250\,\text{nm/s}$ (bottom).

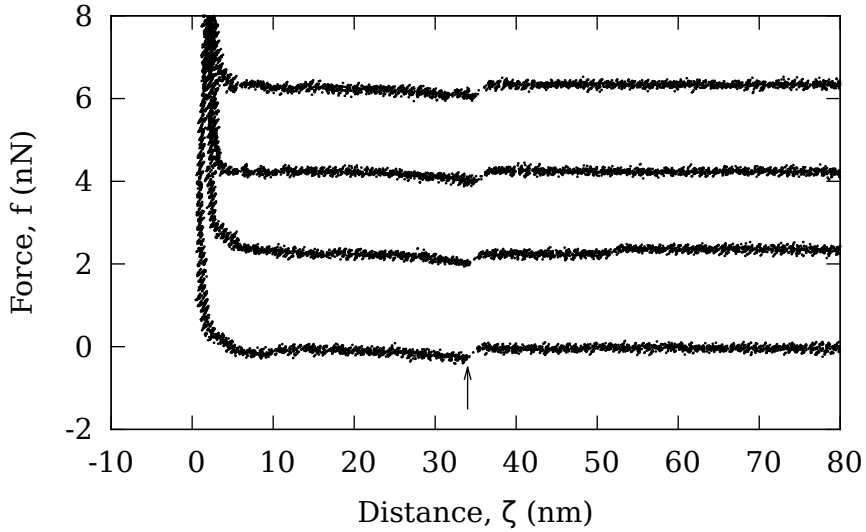


**Figure 7.9:** Force curves showing a feature which may indicate lipid tube formation, indicated by the arrow. The attractive force (negative on this diagram) rises nonlinearly, reaching a peak before rapidly relaxing. Curves are offset in the vertical direction for clarity. Retraction velocity was $v_p = 500$ nm/s.

roughly constant, with mean at $8.1 \pm 0.2$ nm, when pulling at a slower speed (250 nm/s), but the mean force is reduced to $112 \pm 13$ pN ($n = 71$) (see histograms in Figure 7.8). A loading rate dependent force is consistent with a 'bond-breaking' transition, such as an adhesion.

Taking the radius of the probe $r_p$ to be 100 nm, a crude adhesion energy is

$$F_A = \int \gamma_{ms} dA = \pi r_p^2 \gamma_{ms}, \tag{7.1}$$

where $\gamma_{ms}$ is the membrane-solid support interfacial surface tension. The energy due to the probe force can be roughly estimated by $fz_A$, where $z_A$ is the distance where adhesion fails. Equating this energy with (7.1) results in the estimate for the membrane-solid support interfacial surface tension $\gamma_{ms} = 4.1 \times 10^{-5}$ J/m$^2$ = 0.01 $k_B$T/nm$^2$. If $r_p = 100$ nm, then $F_A = 100\ k_B$T.

### 7.3.2 Tube formation

The mean peak force attributed to tube formation was $112 \pm 3$ pN, encountered at a mean distance of $31.3 \pm 0.2$ nm from surface contact ($n = 63$) for retraction velocity 500 nm/s. For the slower velocity 250 nm/s the force was $93 \pm 10$ pN at an average distance of $34.0 \pm 2.4$ nm ($n = 25$). The mean peak force at the slower velocity is somewhat less than that of the faster velocity. However, taking into account the standard error bounds they are reasonably consistent with each other,

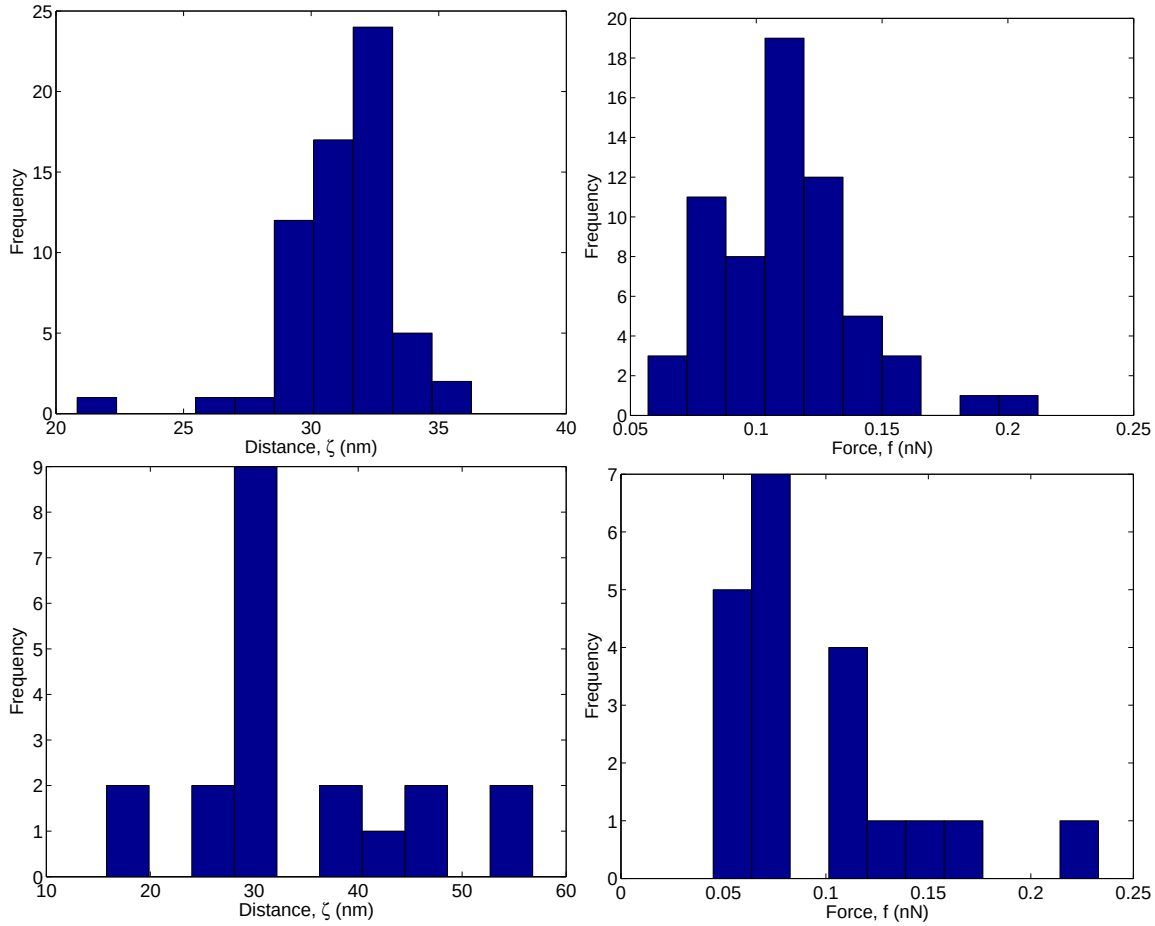


**Figure 7.10:** Tube formation peak histograms of distance (left) and force (right), $n = 63$ and $v_p = 500\,\text{nm/s}$ (top), and $n = 20$ and $v_p = 250\,\text{nm/s}$ (bottom).

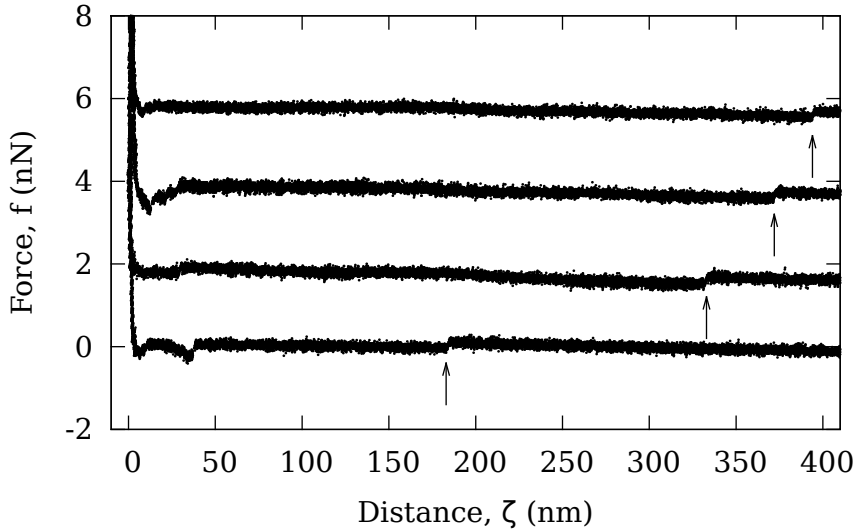


**Figure 7.11:** Force curves displaying a step in force at large probe-surface separation, indicated by arrows. This probably indicates rupture or detachment of a lipid tube. Note the high variability in distance. The magnitude of the force step remains relatively constant. Not all curves showing a putative tube formation feature show a step, and *vice versa*. Retraction velocity was $v_p = 500$ nm/s.

lending support to the conclusion that dissipation is not a significant effect at these velocities (as discussed in §5.8). Interestingly, the distance from the surface at which this force peak appears is rather constant around 32 nm.

### 7.3.3 Tube rupture

Often after observing an apparent tube formation peak, a step reduction in force appears at some larger, highly variable distance from the surface. The mean average distance at which the step occurred was 139.6 ± 8.8 nm for velocity 500 nm/s ($n = 122$) and 133.0 ± 17.6 nm for pulling velocity 250 nm/s ($n = 32$). The force magnitude of the steps were not significantly variable; 132 ± 5 pN at 500 nm/s, and 140 ± 3 pN at 250 nm/s.

The most ready explanation for a sudden drop in force, assuming a tube has been formed, is that the tube either ruptures or detaches from the probe. Assuming this to be the case, and further that the force after the step is zero, then the magnitude of the jump $f_r$ is equal to the tube extension force $f_0$ of Chapter 5.

Occasionally, the force step was repeated twice. The mean step force of second steps was 127 ± 9 pN, with mean distance 167.7 ± 20.1 nm, at a pulling velocity of 500 nm/s. Two steps were observed together 18 times out of 122 at this velocity. At a pulling velocity of 250 nm/s, two steps were observed only three times out of 32. The mean force of the second step, at this velocity, was 135 ± 4 pN, with mean distance 201.0 ± 79.9 nm.

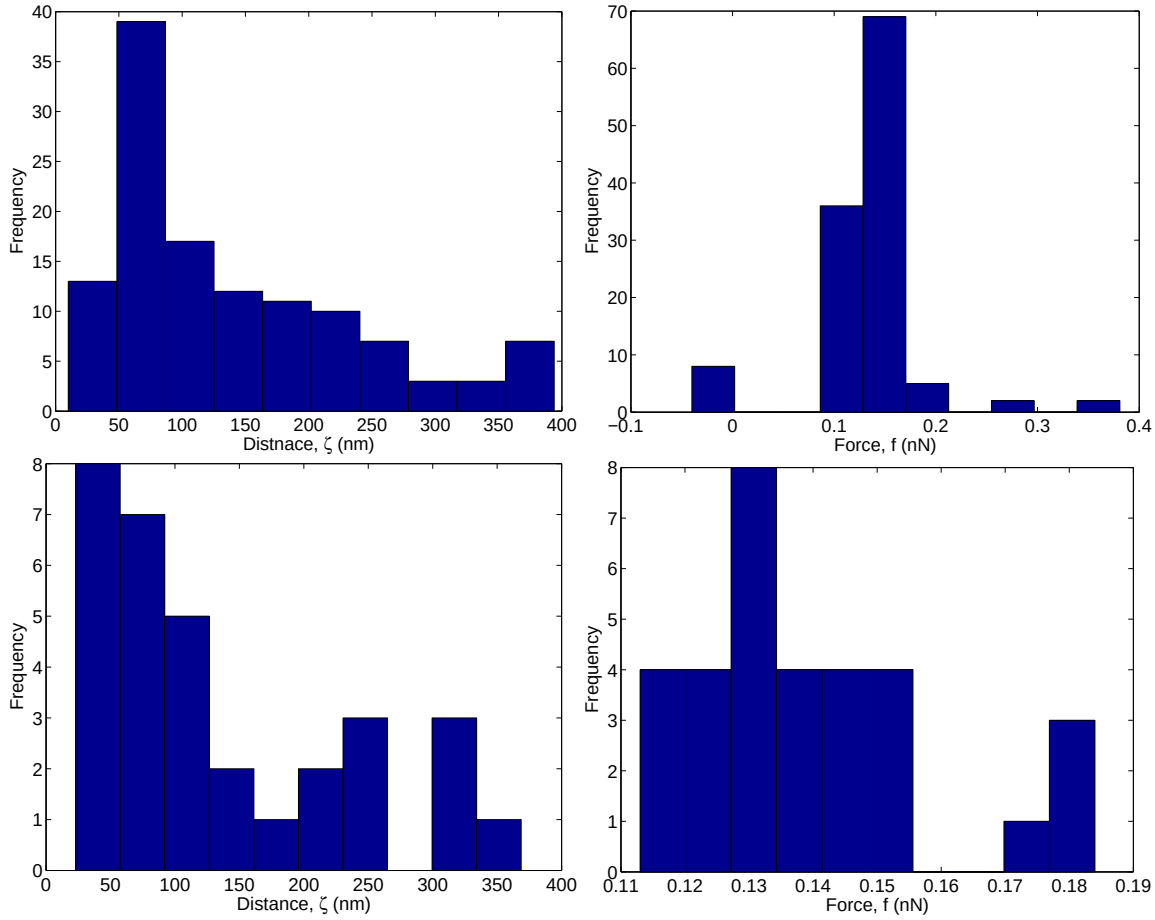


**Figure 7.12:** Tube rupture force step histograms showing distance (left) and force step magnitude (right), $n = 122$ and $v_p = 500$ nm/s (top), and $n = 32$ and $v_p = 250$ nm/s (bottom).

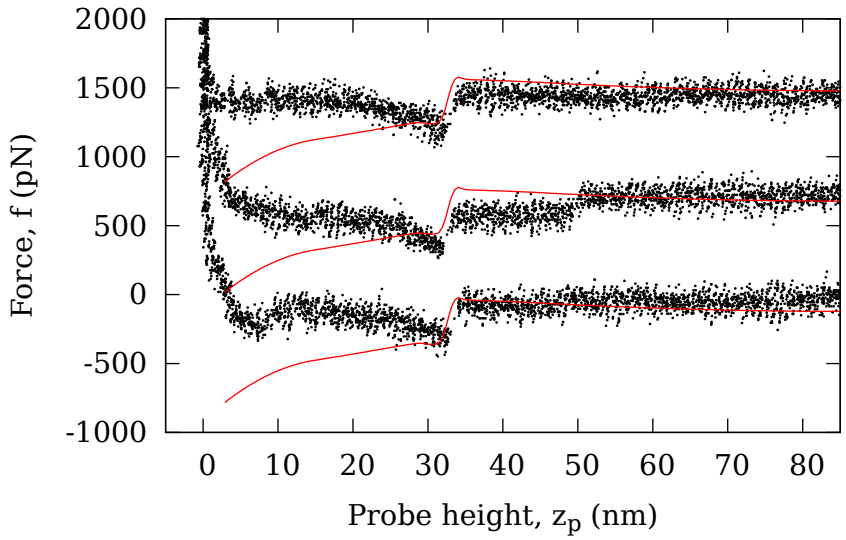


**Figure 7.13:** Overlay of theoretical prediction of force during retraction (red line) on data (black points) showing tube formation feature. The relaxation in force around 30 nm matches well between the theory and data, both in distance and force magnitude. However, there is a significant discrepency in the force at short distance, and also the gradient of the force at short distance has the wrong sign. Curves are offset in vertical direction for clarity. Retraction velocity was $v_p = 500$ nm/s.

## 7.4 Comparison with theoretical predictions

The putative tube rupture forces reported in section §7.3.3, correspond to a surface tension $\sigma_1 = 2.7$ pN/nm, using equation (5.8) and the rigidity $\kappa = 85$ pN nm for DOPC [199].

The highly repeatable distance at which the putative tube formation feature was observed can be used to define the length scale $r_0$ in the theoretically calculated force curves shown in Figure 5.5. Based on the probe images shown in Figure 7.4 assume the probe radius to be $r_p = 100$ nm. For such a probe the theory predicts the jump in force during formation of the tube to occur at $z = 3.2r_0$. Using the data given in §7.3.2 fixes $r_0 = 9.8$ nm as the radius of the tube and the length scale. This provides another estimation of the surface tension by (5.6) yielding $\sigma_2 = 2.1$ pN/nm. Together $\sigma_2$ and $\kappa$ give the force scale $f_0 = 119$ pN. This is the tube elongation force and is less than the experimentally determined value $132 \pm 5$ pN, although reasonably close. The disparity may indicate the $P = 0$ is not a valid assumption. Unfortunately, it was not possible to numerically solve for the free energy $F$ when $P \neq 0$, and therefore a theoretical force curve to compare with is not available.

# 8 Discussion

## 8.1 Microtubule-Dam1 force generation

Current microtubule (MT)-Dam1 force generation models take the approach of including all the molecular processes believed to take place. Specifically, a protofilament powerstroke, steric confinement by protofilaments, MT-Dam1 binding, and MT depolymerisation are all included. While this leads to models that fulfil the requirements of translocating a kinetochore and sustaining force, the high number of coupled processes limits the ability to discern the key mechanistic features. The modelling in Chapter 4 aimed to break down these key features into separate models which can be fitted to data. The results presented indicate that when considering the effects of MT-Dam1 binding and sterically-confining protofilaments (PFs) independently, each can explain the currently available data reasonably well and are thus unidentifiable. New experiments were therefore suggested that would be capable of discriminating between the models.

The depolymerisation model, where the Dam1 ring suppresses depolymerisation when it is close to the MT end, fits the load-dependent velocity data and supports the hypothesis that a faster depolymerisation mechanism must operate at lower loads. Furthermore, a power stroke does contribute to the effective force generated during depolymerisation but only becomes dominant at over 2pN load. Fitting to the data yields parameter estimations for the rate of powerstroke depolymerisation as opposed to free depolymerisation, a Dam1-ring binding energy, and an individual axial tubulin bond breaking rate. Furthermore, the model posits that the Dam1-ring interacts with the end of the MT over a range of $14.0 \pm 1.4$ nm, intriguingly close to a tubulin axial repeat length (8 nm or, perhaps, 1.5 times this due to helicity). Inside this length the kinetics of depolymerisation are reduced

by the Dam1-ring. A simple mechanism for this effect might be a Hill-like sleeve that suppresses depolymerisation by covering the next intact tubulin dimers in the PFs that are about to split and preventing them from curling. This may also support the idea that the MT depolymerises by first splitting along its seam, with the other PF pairs splitting apart somewhat behind this leading crack-like defect. Materials do tend to split along fractures due to the concentration of elastic stresses [200]. In particular, step-wise splitting between PFs could yield step sizes of approximately tubulin axial length. It would be hard to physically motivate a range $\delta$ that is significantly larger than the incremental depolymerisation step size or smaller than the polymeric repeat unit length.

Current structural visualisation capabilities cannot resolve the question of which model operates *in vivo*. In order to draw distinctions between the binding and protofilament models, parameter variations were considered. By employing new protocols in existing experimental systems the two basic models can be distinguished. By varying the depolymerisation velocity of the MT, the diffusion coefficient of the Dam1, or applying an oscillating load to the ring, differences in the models become apparent. Each of these parameters are feasible to alter during current experimental procedures.

Throughout this study it has been assumed that depolymerisation is sufficiently slow compared to ring diffusion that we can consider the distribution of the rings position to be quasi-equilibrated. Over the range of parameters considered this assumption is valid to within 1% of the predicted velocity. It is important to note that the present work has neglected *in vivo* factors such as microtubule-associated proteins (MAPs) or kinases. However, some of these factors operate to increase or reduce the depolymerisation rate of the microtubule, a parameter included in the model, so they could conceivably be incorporated. On this basis, it can be expected that the general results will remain largely applicable.

Dam1 has been assumed to be present as a ring, although only the protofilament model critically depends on this topology. Since this work was completed, further results have raised the possibility that Dam1 may operate as short oligomers or single complexes. Oligomers of 2–4 Dam1 complexes are also capable of diffusion on the MT and tracking the depolymerisation. However, the residence time – the time between complex binding and unbinding – for unphosphorylated Dam1 was only $0.85 \pm 0.04$ s and for phosphorylated Dam1 it was $2.1 \pm 0.1$ s [160], suggesting that cooperative binding between complexes may be required for effectively maintaining a kinetochore attachment, over the more than ten minute course of anaphase. Dam1 oligomers can also support loads and transport cargo. Assemblies larger than a ring ($> 25$ complexes), such as helices, are not able to track the depolymerisation [201]. Load-bearing oligomers can only sustain forces

smaller than those sustained by rings, and are less reliable [46].

*In vivo* quantitative fluorescence copy number measurements put the number of Dam1 complexes localised at the kinetochore during anaphase at 6-7 per kinetochore [161, 202], far fewer than the 16-25 required to form the ring according to symmetry [38, 162]. *In vitro* a Dam1 concentration of at least 1 nM is required to form rings, although reducing the tubulin concentration results in a correspondingly less Dam1 concentration requirement, suggesting that the local density of Dam1 on the MT is the key parameter [59].

If Dam1 oligomers or single complexes interact with PFs in a comparable fashion as a ring would, the model would be indistinguishable for rings or oligomers. Of course, *a priori* this is not likely to be known. However, it is clear that the binding is insensitive to the topology of the Dam1-MT attachment; only a binding energy is relevant. The protofilament model does rely on steric confinement of a ring by the PFs, which clearly would not work if Dam1 was present as single particles or oligomers. However, even in this case it is conceivable that the existence of PFs could prevent the Dam1 complexes from detaching, e.g., by favourable binding to curved PFs, or by direct fibrillar attachments between kinetochore and PFs (as observed by McIntosh et al. [60]). In any case, the two models would still provide a distinction between a dominant binding effect or an intact PF dependency. Even if it was not possible to define a realistic model depending on intact PFs, the binding model may be of use to determine whether ring or oligomer is present based on e.g., differing diffusion constant.

In summary, two distinct and simple models of the MT-Dam1 attachment mechanism have been shown to be amenable to discrimination by varying MT depolymermisation velocity, Dam1 ring diffusion coefficient, or oscillating load force frequency, and monitoring changes in runtime.

## 8.2 Pulling lipid tubes

Force curves resulting from experiments where an atomic force microscope (AFM) probe is pressed into a lipid bilayer on a surface and then retracted appear to show similar features to lipid tube pulling experiments where optical tweezers are used to pull lipids from a vesicle [109, 110]. The data is in qualitative agreement with previous surface-supported lipid tube pulling experiments using AFM [2, 3], however in the present experiments the probe was ground flat to facilitate better membrane adhesion. Three distinct features can be discerned: an adhesion at short range, a nonlinear force peak at around 31 nm, and a step change in force at larger distances averaging $\sim 160$ nm.

The short-range adhesion force is probably due to the detachment of an area

of membrane similar to the flat area of the probe. It is difficult to see how this could be a gradual dewetting process. It seems more likely that the adhesion energy of membrane presents a significant barrier and thus the probe encounters a substantial force until rapid dewetting occurs after the adhesion energy can be overcome. This effect is not included in the theoretical model of Chapter 5.

The force peak at 31 nm is very repeatable and can be explained by the formation of a tube. Prior to tube formation the membrane sheet adopts a tent-like configuration. As the probe is raised, the tent enlargement is very costly in terms of surface area, which is penalised energetically by the surface tension. At some point the energy cost of an enlarged tent becomes greater than that of a tube and a rapid relaxation occurs as the membrane adopts the tube configuration. Tube elongation requires only a constant amount of area per length pulled, so the energy increase is linear and the force of elongation is a constant. The solutions to the theoretical model reveal the shape of the membrane as the probe is retracted and clearly demonstrate the transition between the tent-like and tube-like configurations. Moreover, the predicted free energy and force curve contain a rapid relaxation in force when the transition occurs. The length and force scales in the theory can be set independently by the asymptotic force of tube elongation $f_0$ and the probe height at which the shape transition occurs. Overlaying the theoretical and experimental force curves shows good agreement in the magnitude of the relaxation in force, which is not a fitted value. However, the force gradient before the transition has the wrong sign. It is not immediately obvious why this should be the case. The surface radius graph in Figure 5.3 suggests a reason for this discrepancy. In the theoretical calculations the surface radius of membrane detachment is zero at zero probe height, and quickly enlarges as the probe is retracted. The rate of enlargement reduces with increasing height until a maximum is reached. As result the free energy $F$ (in Figure 5.2) rises rapidly at small $z_p$. Force is the derivative of $F$ with respect to $z_p$ and is therefore large near $z_p = 0$ and decays with retraction. This does not accurately model the experiment system as the membrane almost has surface radius $> r_p$ immediately after retraction, as the adhesion effect previously described suggests. Calculating the theoretical force curve for $P \neq 0$, using the fluid flow approximation described in §5.7.2, may solve this problem. Unfortunately, due to numerical instability in the solution procedure, it was not possible to minimise the free energy with respect to the surface radius of membrane detachment and obtain force curves.

The step in force at larger distances is most likely the detachment or rupture of the lipid tube. It is quite consistent in force magnitude but is highly variable in the distance at which it occurs. It is not clear what causes rupture or detachment, and indeed which of these two possibilities occurs. Detachment could occur as a

result a sudden increase in force, possibly due to surface tension increasing as the reservoir of membrane area on the surface is exhausted or inhibited in some way. However, the data do not show a force increase prior to the step. Rupture could also be caused by increasing tension as it would decrease the tube radius beyond the limit of sustainable curvature. Another possibility is that the attachment of the membrane to the probe is not strong, and detachment occurs stochastically, in a manner analogous to stick-slip friction [203]. As with the adhesion effect, this is not included in the theoretical model.

In summary, pulling tubes from solid-supported lipid bilayer membranes using AFM is feasible and, moreover, allows the measurement of the surface tension the bilayer by comparison with theoretical predictions based on axisymmetric shape equation approach. This has utility in applications where one wishes to insert, e.g. ion channels, into a solid-supported lipid bilayer, such as biosensors [147]. It may also prove useful where spatial mapping of the surface tension of flat membranes is of interest, e.g. photosynthetic thylakoid membranes.

# Bibliography


[1] H. Maiato and M. Lince-Faria. The perpetual movements of anaphase. *Cell. Mol. Life Sci.* 67:2251–269, 2010.

[2] N. Maeda, T. J. Senden, and J.-M. di Meglio. Micromanipulation of phospholipid bilayers by atomic force microscopy. *Biomembranes* 1564(1):165–172, 2002.

[3] I. Pera, R. Stark, M. Kappl, H.-J. Butt, and F. Benfenati. Using the atomic force microscope to study the interaction between two solid supported lipid bilayers and the influence of Synapsin I. *Biophys. J.* 87(4):2446–2455, 2004.

[4] E. Schrödinger. *What is life?* Cambridge University Press, canto edition, 1992.

[5] W. Flemming. *Zellsubstanz, kern und zelltheilung*. Verlag Vogel, Leipzig, 1882.

[6] M. Kikkawa, T. Ishikawa, T. Nakata, T. Wakabayashi, and N. Hirokawa. Direct visualization of the microtubule lattice seam both in vitro and in vivo. *J. Cell Biol.* 127(6):1965–1971, 1994.

[7] M. Kikumoto, M. Kurachi, V. Tosa, and H. Tashiro. Flexural rigidity of individual microtubules measured by a buckling force with optical traps. *Biophys. J.* 90(5):1687–1696, Mar. 2006.

[8] T. Mitchison and M. Kirschner. Dynamic instability of microtubule growth. *Nature* 312(5991):237–242, Nov. 1984.

[9] M. Moritz, M. B. Braunfeld, J. W. Sedat, B. Alberts, and D. A. Agard. Microtubule nucleation by $\gamma$-tubulin-containing rings in the centrosome. *Nature* 378:638–640, 1995.

[10] Y. Zheng, M. L. Wong, B. Alberts, and T. Mitchison. Nucleation of microtubule assembly by a $\gamma$-tubulin-containing ring complex. *Nature* 378:578–583, 1995.

[11] S. Inoué and E. Salmon. Force generation by microtubule assembly/disassembly in mitosis and related movements. *Mol. Biol. Cell* 6(12):1619–1640, 1995.

[12] R. B. Nicklas. Chromosome velocity during mitosis as a function of chromosome size and position. *J. Cell Biol.* 25(1):119–135, 1965.

[13] B. R. Nicklas. Measurements of the Force Produced by the Mitotic Spindle in Anaphase. *J. Cell Biol.* 97:542–548, 1983.

[14] M. Coue, V. Lombillo, and J. McIntosh. Microtubule depolymerization promotes particle and chromosome movement in vitro. *J. Cell Biol.* 112(6):1165–1175, 1991.

[15] G. Civelekoglu-Scholey, D. J. Sharp, A. Mogilner, and J. M. Scholey. Model of Chromosome Motility in *Drosophila* Embryos: Adaptation of a General Mechanism for Rapid Mitosis. *Biophys. J.* 90(11):3966–3982, June 2006.

[16] K. R. Porter. Cytoplasmic microtubules and their functions. *Principles of biomolecular organization*, pp. 308–356, 1966.

[17] S. Inoué. *Studies of the structure of the mitotic spindle in living cells with an improved polarization microscope*. Ph.D. thesis, Princeton University, Princeton, NJ, 1951.

[18] C. L. Rieder. The formation, structure, and composition of the mammalian kinetochore and kinetochore fiber. *Int. Rev. Cytol.* 79:1–58, 1982.

[19] S. Inoué and H. Sato. Cell Motility by Labile Association of Molecules: The nature of mitotic spindle fibers and their role in chromosome movement. *J. Gen. Physiol.* 50(6):259–292, 1967.

[20] R. Skibbens, V. Skeen, and E. Salmon. Directional instability of kinetochore motility during chromosome congression and segregation in mitotic newt lung cells: a push-pull mechanism. *J. Cell Biol.* 122(4):859–875, 1993.

[21] K. Ke, J. Cheng, and A. J. Hunt. The distribution of polar ejection forces determines the amplitude of chromosome directional instability. *Curr. Biol.* 19(10):807–815, 2009.

[22] T. M. Kapoor and D. A. Compton. Searching for the middle ground: mechanisms of chromosome alignment during mitosis. *J. Cell Biol.* 157(4):551–556, 2002.

[23] J. R. McIntosh, E. L. Grishchuk, and R. R. West. Chromosome-microtubule interactions during mitosis. *Annu. Rev. Cell Dev. Biol.* 18(1):193–219, 2002.

[24] J. Simon and E. Salmon. The structure of microtubule ends during the elongation and shortening phases of dynamic instability examined by negative-stain electron microscopy. *J. Cell Sci.* 96(4):571–582, 1990.

[25] E.-M. Mandelkow, E. Mandelkow, and R. A. Milligan. Microtubule dynamics and microtubule caps: a time-resolved cryo-electron microscopy study. *J. Cell Biol.* 114(5):977–991, 1991.

[26] D. Chrétien, S. D. Fuller, and E. Karsenti. Structure of growing microtubule ends: two-dimensional sheets close into tubes at variable rates. *J. Cell Biol.* 129(5):1311–1328, 1995.

[27] J. Löwe, H. Li, K. H. Downing, and E. Nogales. Refined structure of $\alpha\beta$-tubulin at 3.5a resolution. *J. Mol. Biol.* 313(5):1045 – 1057, 2001.

[28] R. B. Ravelli, B. Gigant, P. A. Curmi, I. Jourdain, S. Lachkar, A. Sobel, and M. Knossow. Insight into tubulin regulation from a complex with colchicine and a stathmin-like domain. *Nature* 428(6979):198–202, 2004.

[29] M. Caplow and J. Shanks. Evidence that a single monolayer tubulin-GTP cap is both necessary and sufficient to stabilize microtubules. *Mol. Biol. Cell* 7(4):663–675, 1996.

[30] A. Krebs, K. N. Goldie, and A. Hoenger. Structural rearrangements in tubulin following microtubule formation. *EMBO Rep.* 6(3):227–232, 2005.

[31] L. M. Rice, E. A. Montabana, and D. A. Agard. The lattice as allosteric effector: Structural studies of alphabeta- and gamma-tubulin clarify the role of GTP in microtubule assembly. *Proc. Natl. Acad. Sci. U. S. A.* 105(14):5378–5383, 2008.

[32] E. L. Grishchuk, M. L. Molodtsov, F. I. Ataullakhanov, and J. R. McIntosh. Force production by disassembling microtubules. *Nature* 438:384–388, 2005.

[33] D. E. Koshland, T. J. Mitchison, and M. W. Kirschner. Polewards chromosome movement driven by microtubule depolymerization in vitro. *Nature* 331(6156):499–504, Feb. 1988.

[34] T. J. Mitchison. Microtubule dynamics and kinetochore function in mitosis. *Ann. Rev. Cell Biol.* 4(1):527–545, 1988.

[35] L. Cassimeris. Mitosis: Riding the Protofilament Curl. *Curr. Biol.* 16(6):R214–R216, 2006.

[36] S. Westermann, A. Avila-Sakar, H.-W. Wang, H. Niederstrasser, J. Wong, D. G. Drubin, E. Nogales, and G. Barnes. Formation of a dynamic kinetochore-microtubule interface through assembly of the Dam1 ring complex. *Mol. Cell* 17(2):277–290, 2005.

[37] J. L. Miranda, P. D. Wulf, P. K. Sorger, and S. C. Harrison. The yeast DASH complex forms closed rings on microtubules. *Nat. Struct. Mol. Biol.* 12(2):138–143, Feb. 2005.

[38] H.-W. Wang, V. H. Ramey, S. Westermann, A. E. Leschziner, J. P. I. Welburn, Y. Nakajima, D. G. Drubin, G. Barnes, and E. Nogales. Architecture of the Dam1 kinetochore ring complex and implications for microtubule-driven assembly and force-coupling mechanisms. *Nat Struct Mol Biol* 14(8):721–726, Aug. 2007.

[39] S. Westermann, H.-W. Wang, A. Avila-Sakar, D. G. Drubin, E. Nogales, and G. Barnes. The Dam1 kinetochore ring complex moves processively on depolymerizing microtubule ends. *Nature* 440(7083):565–569, 2006.

[40] M. H. Jones, X. He, T. H. Giddings, and M. Winey. Yeast Dam1p has a role at the kinetochore in assembly of the mitotic spindle. *Proc. Natl. Acad. Sci. U. S. A.* 98(24):13675–13680, 2001.

[41] I. M. Cheeseman, M. Enquist-Newman, T. Muller-Reichert, D. G. Drubin, and G. Barnes. Mitotic Spindle Integrity and Kinetochore Function Linked by the Duo1p/Dam1p Complex. *J. Cell Biol.* 152(1):197–212, 2001.

[42] E. Kiermaier, S. Woehrer, Y. Peng, K. Mechtler, and S. Westermann. A dam1-based artificial kinetochore is sufficient to promote chromosome segregation in budding yeast. *Nat. Cell Biol.* 11(9):1109–1115, 2009.

[43] A. Franco, J. C. Meadows, and J. B. A. Millar. The Dam1/DASH complex is required for the retrieval of unclustered kinetochores in fission yeast. *J. Cell Sci.* 120(19):3345–3351, 2007.

[44] A. P. Joglekar, K. S. Bloom, and E. Salmon. Mechanisms of force generation by end-on kinetochore-microtubule attachments. *Curr. Opin. Cell Biol.* 22(1):57 – 67, 2010.

[45] T. N. Gaitanos, A. Santamaria, A. A. Jeyaprakash, B. Wang, E. Conti, and E. A. Nigg. Stable kinetochore-microtubule interactions depend on the ska complex and its new component ska3/c13orf3. *EMBO J.* 28(10):1442–1452, 2009.

[46] E. L. Grishchuk, A. K. Efremov, V. A. Volkov, I. S. Spiridonov, N. Gudimchuk, S. Westermann, D. Drubin, G. Barnes, J. R. McIntosh, and F. I. Ataullakhanov. The Dam1 ring binds microtubules strongly enough to be a processive as well as energy-efficient coupler for chromosome motion. *Proc. Natl. Acad. Sci. U. S. A.* 105(40):15423–15428, 2008.

[47] A. D. Franck, A. F. Powers, D. R. Gestaut, T. N. Davis, and C. L. Asbury. Direct physical study of kinetochore-microtubule interactions by reconstitution and interrogation with an optical force clamp. *Methods* 51(2):242 – 250, 2010.

[48] C. L. Asbury, D. R. Gestaut, A. F. Powers, A. D. Franck, and T. N. Davis. The Dam1 kinetochore complex harnesses microtubule dynamics to produce force and movement. *Proc. Natl. Acad. Sci. U. S. A.* 103(26):9873–9878, 2006.

[49] A. D. Franck, A. F. Powers, D. R. Gestaut, T. Gonen, T. N. Davis, and C. L. Asbury. Tension applied through the Dam1 complex promotes microtubule elongation providing a direct mechanism for length control in mitosis. *Nat. Cell Biol.* 9(7):832–837, July 2007.

[50] I. M. Cheeseman, J. S. Chappie, E. M. Wilson-Kubalek, and A. Desai. The conserved KMN network constitutes the core microtubule-binding site of the kinetochore. *Cell* 127(5):983 – 997, 2006.

[51] C. Ciferri, J. De Luca, S. Monzani, K. J. Ferrari, D. Ristic, C. Wyman, H. Stark, J. Kilmartin, E. D. Salmon, and A. Musacchio. Architecture of the human Ndc80-Hec1 complex, a critical constituent of the outer kinetochore. *J. Biol. Chem.* 280(32):29088–29095, 2005.

[52] C. Ciferri, A. Musacchio, and A. Petrovic. The ndc80 complex: Hub of kinetochore activity. *FEBS Lett.* 581(15):2862 – 2869, 2007.

[53] A. D. McAinsh, P. Meraldi, V. M. Draviam, A. Toso, and P. K. Sorger. The human kinetochore proteins Nnf1R and Mcm21R are required for accurate chromosome segregation. *EMBO J.* 25(17):4033–4049, 2006.

[54] J. G. DeLuca, Y. Dong, P. Hergert, J. Strauss, J. M. Hickey, E. D. Salmon, and B. F. McEwen. Hec1 and Nuf2 Are Core Components of the Kinetochore Outer Plate Essential for Organizing Microtubule Attachment Sites. *Mol. Biol. Cell* 16(2):519–531, 2005.

[55] J. G. DeLuca, W. E. Gall, C. Ciferri, D. Cimini, A. Musacchio, and E. Salmon. Kinetochore microtubule dynamics and attachment stability are regulated by Hec1. *Cell* 127(5):969 – 982, 2006.

[56] R. R. Wei, P. K. Sorger, and S. C. Harrison. Molecular organization of the Ndc80 complex, an essential kinetochore component. *Proc. Natl. Acad. Sci. U. S. A.* 102(15):5363–5367, 2005.

[57] A. F. Powers, A. D. Franck, D. R. Gestaut, J. Cooper, B. Gracyzk, R. R. Wei, L. Wordeman, T. N. Davis, and C. L. Asbury. The Ndc80 kinetochore complex forms load–bearing attachments to dynamic microtubule tips via biased diffusion. *Cell* 136(5):865–875, 2009.

[58] S. L. Kline-Smith, S. Sandall, and A. Desai. Kinetochore-spindle microtubule interactions during mitosis. *Curr. Opin. Cell Biol.* 17(1):35 – 46, 2005.

[59] J. F. Tien, N. T. Umbreit, D. R. Gestaut, A. D. Franck, J. Cooper, L. Wordeman, T. Gonen, C. L. Asbury, and T. N. Davis. Cooperation of the Dam1 and Ndc80 kinetochore complexes enhances microtubule coupling and is regulated by Aurora B. *J. Cell Biol.* 189(4):713–723, 2010.

[60] J. R. McIntosh, E. L. Grishchuk, M. K. Morphew, A. K. Efremov, K. Zhudenkov, V. A. Volkov, I. M. Cheeseman, A. Desai, D. N. Mastronarde, and F. I. Ataullakhanov. Fibrils connect microtubule tips with kinetochores: A mechanism to couple tubulin dynamics to chromosome motion. *Cell* 135(2):322–333, 2008.

[61] D. J. Sharp, G. C. Rogers, and J. M. Scholey. Microtubule motors in mitosis. *Nature* 407(6800):41–47, Sept. 2000.

[62] A. P. Joglekar and A. J. Hunt. A simple, mechanistic model for directional instability during mitotic chromosome movements. *Biophys. J.* 83(1):42–58, 2002.

[63] L. G. Bergen and G. G. Borisy. Head-to-tail polymerization of microtubules in vitro. Electron microscope analysis of seeded assembly. *J. Cell Biol.* 84(1):141–150, 1980.

[64] R. L. Margolis and L. Wilson. Microtubule treadmills - possible molecular machinery. *Nature* 293(5835):705–711, 1981.

[65] A. Wegner. Head to tail polymerization of actin. *J. Mol. Biol.* 108(1):139 – 150, 1976.

[66] T. L. Hill. Bioenergetic aspects and polymer length distribution in steady-state head-to-tail polymerization of actin or microtubules. *Proc. Natl. Acad. Sci. U. S. A.* 77(8):4803–4807, 1980.

[67] T. L. Hill. Microfilament or Microtubule Assembly or Disassembly against a Force. *Proc. Natl. Acad. Sci. U. S. A.* 78(9):5613–5617, Sept. 1981.

[68] T. L. Hill and M. W. Kirschner. Subunit treadmilling of microtubules or actin in the presence of cellular barriers: possible conversion of chemical free energy into mechanical work. *Proc. Natl. Acad. Sci. U. S. A.* 79(2):490–494, 1982.

[69] J. A. Theriot. The polymerization motor. *Traffic* 1(1):19–28, 2000.

[70] M. Caplow, R. L. Ruhlen, and J. Shanks. The free energy for hydrolysis of a microtubule-bound nucleotide triphosphate is near zero: all of the free energy for hydrolysis is stored in the microtubule lattice. *J. Cell Biol.* 127(3):779–788, 1994.

[71] B. Mickey and J. Howard. Rigidity of microtubules is increased by stabilizing agents. *J. Cell Biol.* 130(4):909–917, 1995.

[72] A. Desai, P. S. Maddox, T. J. Mitchison, and E. Salmon. Anaphase a chromosome movement and poleward spindle microtubule flux occur at similar rates in *Xenopus* extract spindles. *J. Cell Biol.* 141(3):703–713, 1998.

[73] J. C. Waters, T. J. Mitchison, C. L. Rieder, and E. D. Salmon. The kinetochore microtubule minus-end disassembly associated with poleward flux produces a force that can do work. *Mol. Biol. Cell* 7(10):1547–1558, 1996.

[74] N. J. Ganem, K. Upton, and D. A. Compton. Efficient Mitosis in Human Cells Lacking Poleward Microtubule Flux. *Curr. Biol.* 15(20):1827–1832, 2005.

[75] T. L. Hill. Theoretical Problems Related to the Attachment of Microtubules to Kinetochores. *Proc. Natl. Acad. Sci. U. S. A.* 82(13):4404–4408, 1985.

[76] J. Liu and J. N. Onuchic. A driving and coupling "Pac-Man" mechanism for chromosome poleward translocation in anaphase A. *Proc. Natl. Acad. Sci. U. S. A.* 103(49):18432–18437, 2006.

[77] M. I. Molodtsov, E. A. Ermakova, E. E. Shnol, E. L. Grishchuk, J. R. McIntosh, and F. I. Ataullakhanov. A molecular-mechanical model of the microtubule. *Biophys. J.* 88(5):3167–3179, 2005.

[78] M. I. Molodtsov, E. L. Grishchuk, A. K. Efremov, J. R. McIntosh, and F. I. Ataullakhanov. Force production by depolymerizing microtubules: A theoretical study. *Proc. Natl. Acad. Sci. U. S. A.* 102(12):4353–4358, Mar. 2005.

[79] A. Efremov, E. L. Grishchuk, J. R. McIntosh, and F. I. Ataullakhanov. In search of an optimal ring to couple microtubule depolymerization to processive chromosome motions. *Proc. Natl. Acad. Sci. U. S. A.* 104(48):19017–19022, 2007.

[80] S. A. Endow. Microtubule motors in spindle and chromosome motility. *Euro. J. Biochem.* 262(1):12–18, 1999.

[81] N. R. Barton and L. S. Goldstein. Going mobile: microtubule motors and chromosome segregation. *Proc. Natl. Acad. Sci. U. S. A.* 93(5):1735–1742, 1996.

[82] R. Hooke. *Micrographia: or, Some physiological descriptions of minute bodies made by magnifying glasses*. J. Martyn and J. Allestry, London, 1665.

[83] B. Alberts, A. Johnson, J. Lewis, M. Raff, K. Roberts, and P. Walter. *Molecular biology of the cell*. Garland Science, New York, fourth edition, 2002.

[84] E. Bi and J. Lutkenhaus. FtsZ ring structure associated with division in *Escherichia coli*. *Nature* 354(6349):161–164, Nov. 1991.

[85] S.-y. Miyagishima, K. Nishida, T. Mori, M. Matsuzaki, T. Higashiyama, H. Kuroiwa, and T. Kuroiwa. A plant-specific dynamin-related protein forms a ring at the chloroplast division site. *Plant Cell* 15(3):655–665, 2003.

[86] M. A. Fogel and M. K. Waldor. A dynamic, mitotic-like mechanism for bacterial chromosome segregation. *Genes Dev.* 20(23):3269–3282, 2006.

[87] J. Pogliano. The bacterial cytoskeleton. *Curr. Opin. Cell Biol.* 20(1):19 – 27, 2008.

[88] A. Rustom, R. Saffrich, I. Markovic, P. Walther, and H.-H. Gerdes. Nanotubular highways for intercellular organelle transport. *Science* 303:1007–1010, 2004.

[89] H.-H. Gerdes, N. V. Bukoreshtliev, and J. F. Barroso. Tunneling nanotubes: A new route for the exchange of components between animal cells. *FEBS Lett.* 581(11):2194 – 2201, 2007.

[90] B. Önfelt, S. Nedvetzki, K. Yanagi, and D. M. Davis. Cutting Edge: Membrane Nanotubes Connect Immune Cells. *J. Immunol.* 173(3):1511–1513, 2004.

[91] S. C. Watkins and R. D. Salter. Functional connectivity between immune cells mediated by tunneling nanotubules. *Immunity* 23(3):309–318, Sept. 2005.

[92] S. Sowinski, C. Jolly, O. Berninghausen, M. A. Purbhoo, A. Chauveau, K. Kohler, S. Oddos, P. Eissmann, F. M. Brodsky, C. Hopkins, B. Onfelt, Q. Sattentau, and D. M. Davis. Membrane nanotubes physically connect T cells over long distances presenting a novel route for HIV-1 transmission. *Nat. Cell Biol.* 10(2):211–219, 2008.

[93] K. Gousset, E. Schiff, C. Langevin, Z. Marijanovic, A. Caputo, D. T. Browman, N. Chenouard, F. de Chaumont, A. Martino, J. Enninga, J.-C. Olivo-Marin, D. Mannel, and C. Zurzolo. Prions hijack tunnelling nanotubes for intercellular spread. *Nat. Cell Biol.* 11(3):328–336, 2009.

[94] P. B. Canham. The minimum energy of bending as a possible explanation of the biconcave shape of the human red blood cell. *J. Theoret. Biol.* 26:61–81, 1970.

[95] W. Helfrich. Elastic properties of lipid bilayers: Theory and possible experiments. *Z. Naturforsch.* 28c:693–703, 1973.

[96] O.-Y. Zhong-can and W. Helfrich. Bending energy of vesicle membranes: General expressions for the first, second and third variation of the shape energy and applications to spheres and cylinders. *Phys. Rev. A* 39(10):5280–5288, 1989.

[97] U. Seifert. Vesicles of toroidal topology. *Phys. Rev. Lett.* 66(18):2404–2407, May 1991.

[98] U. Seifert, K. Berndl, and R. Lipowsky. Shape transformations of vesicles: Phase diagram for spontaneous-curvature and bilayer-coupling models. *Phys. Rev. A* 44(2):1182–1202, 1991.

[99] W.-M. Zheng and J. Liu. Helfrich shape equation for axisymmetric vesicles as a first integral. *Phys. Rev. E* 48(4):2856–2860, 1993.

[100] F. Jülicher and U. Seifert. Shape equations for axisymmetric vesicles: A clarification. *Phys. Rev. E* 49(5):4728–4731, 1994.

[101] R. Podgornik, S. Svetina, and B. Žekš. Parametrization invariance and shape equations of elastic axisymmetric vesicles. *Phys. Rev. E* 51(1):544–547, 1995.

[102] D. J. Bukman, J. H. Yao, and M. Wortis. Stability of cylindrical vesicles under axial tension. *Phys. Rev. E* 54(5):5463–5468, 1996.

[103] B. Božič, S. Svetina, and B. Žekš. Theoretical analysis of the formation of membrane microtubes on axially strained vesicles. *Phys. Rev. E* 55(5):5834–5842, 1997.

[104] V. Heinrich, B. Božič, S. Svetina, and B. Žekš. Vesicle deformation by an axial load: from elongated shapes to tethered vesicles. *Biophys. J.* 76:2056–2071, 1999.

[105] I. Derényi, F. Jülicher, and J. Prost. Formation and interaction of membrane tubes. *Phys. Rev. Lett.* 88(23):238101, 2002.

[106] T. R. Powers, G. Huber, and R. E. Goldstein. Fluid-membrane tethers: Minimal surfaces and elastic boundary layers. *Phys. Rev. E* 65(4):041901, 2002.

[107] A.-S. Smith, E. Sackmann, and U. Seifert. Pulling tethers from adhered vesicles. *Phys. Rev. Lett.* 92:208101, 2004.

[108] T. Umeda, T. Inaba, A. Ishijima, K. Takiguchi, and H. Hotani. Formation and maintenance of tubular membrane projections: Experiments and numerical calculations. *Biosystems* 93:115–119, 2008.

[109] G. Koster, A. Cacciuto, I. Derényi, D. Frenkel, and M. Dogterom. Force barriers for membrane tube formation. *Phys. Rev. Lett.* 94(6):068101, Feb 2005.

[110] D. Cuvelier, N. Chiaruttini, P. Bassereau, and P. Nassoy. Pulling long tubes from firmly adhered vesicles. *Europhys. Lett.* 71(6):1015–1021, 2005.

[111] G. Koster, M. VanDujin, B. Hofs, and M. Dogterom. Membrane tube formation from giant vesicles by dynamic association of motor proteins. *Proc. Natl. Acad. Sci. U. S. A.* 100(26):15583–1588, 2003.

[112] C. Leduc, O. Campas, K. B. Zeldovich, A. Roux, P. Jolimaitre, L. Bourel-Bonnet, B. Goud, J.-F. Joanny, P. Bassereau, and J. Prost. Cooperative extraction of membrane nanotubes by molecular motors. *Proc. Natl. Acad. Sci. U. S. A.* 101(49):17096–17101, 2004.

[113] R. Waugh and R. Hochmuth. Mechanical equilibrium of thick, hollow, liquid membrane cylinders. *Biophys. J.* 52(3):391–400, 1987.

[114] L. Bo and R. Waugh. Determination of bilayer membrane bending stiffness by tether formation from giant, thin-walled vesicles. *Biophys. J* 55(3):509–517, Mar. 1989.

[115] R. Hochmuth, N. Mohandas, and P. Blackshear. Measurement of the elastic modulus for red cell membrane using a fluid mechanical technique. *Biophys. J.* 13(8):747–762, 1973.

[116] R. Waugh. Surface viscosity measurements from large bilayer vesicle tether formation. II. Experiments. *Biophys. J.* 38(1):29–37, 1982.

[117] D. Raucher and M. P. Sheetz. Characteristics of a membrane reservoir buffering membrane tension. *Biophys. J.* 77:1992–2002, 1999.

[118] S. A. Nowak and T. Chou. Models of dynamic extraction of lipid tethers from cell membranes. *Phys. Biol.* 7(2):026002, 2010.

[119] M. Dogterom, M. Janson, C. Faivre-Moskalenko, A. van der Horst, J. Kerssemakers, C. Tanase, and B. Mulder. Force generation by polymerizing microtubules. *Appl. Phys. A* 75(2):331–336, 2002.

[120] D. K. Fygenson, J. F. Marko, and A. Libchaber. Mechanics of microtubule-based membrane extension. *Phys. Rev. Lett.* 79(22):4497–4500, 1997.

[121] N. J. Carter and R. A. Cross. Mechanics of the kinesin step. *Nature* 435(7040):308–312, 2005.

[122] A. Roux, G. Cappello, J. Cartaud, J. Prost, B. Goud, and P. Bassereau. A minimal system allowing tubulation with molecular motors pulling on giant liposomes. *Proc. Natl. Acad. Sci. U. S. A.* 99(8):5394–5399, 2002.

[123] G. Puu and I. Gustafson. Planar lipid bilayers on solid supports from liposomes - factors of importance for kinetics and stability. *Biochim. Biophys. Acta* 1327(2):149 – 161, 1997.

[124] M. Sun, J. S. Graham, B. Hegedus, F. Marga, Y. Zhang, G. Forgacs, and M. Grandbois. Multiple membrane tethers probed by atomic force microscopy. *Biophys. J.* 89(6):4320–4329, 2005.

[125] G. Binnig, C. F. Quate, and C. Gerber. Atomic Force Microscope. *Phys. Rev. Lett.* 56(9):930–934, Mar. 1986.

[126] F. Ohnesorge and G. Binnig. True atomic resolution by atomic force microscopy through repulsive and attractive forces. *Science* 260(5113):1451–1456, 1993.

[127] H. G. Hansma, M. Bezanilla, F. Zenhausern, M. Adrian, and R. L. Sinsheimer. Atomic force microscopy of DNA in aqueous solutions. *Nucl. Acids Res.* 21(3):505–512, 1993.

[128] G. Meyer and N. M. Amer. Optical-beam-deflection atomic force microscopy: The NaCl (001) surface. *Appl. Phys. Lett.* 56(21):2100–2101, 1990.

[129] U. Hartmann. Magnetic force microscopy. *Ann. Rev. Mat. Sci.* 29(1):53–87, 1999.

[130] G. Valdre. Electric force microscopy. *Imag. Micro.* 8(3):44–46, 2006.

[131] J. V. Macpherson and P. R. Unwin. Combined scanning electrochemical¢atomic force microscopy. *Anal. Chem.* 72(2):276–285, 2000.

[132] A. Avila and B. Bhushan. Electrical measurement techniques in atomic force microscopy. *Crit. Rev. Solid State Mat. Sci.* 35(1):38–51, 2010.

[133] M. Nonnenmacher, M. P. O'Boyle, and H. K. Wickramasinghe. Kelvin probe force microscopy. *Appl. Phys. Lett.* 58(25):2921–2923, 1991.

[134] A. Majumdar, J. P. Carrejo, and J. Lai. Thermal imaging using the atomic force microscope. *Appl. Phys. Lett.* 62(20):2501–2503, 1993.

[135] C. Stroh, H. Wang, R. Bash, B. Ashcroft, J. Nelson, H. Gruber, D. Lohr, S. M. Lindsay, and P. Hinterdorfer. Single-molecule recognition imaging microscopy. *Proc. Natl. Acad. Sci. U. S. A.* 101(34):12503–12507, 2004.

[136] E. Evans. Probing the relation between force – lifetime – and chemistry in single molecular bonds. *Annu. Rev. Biophys. Biomol. Struct.* 30:105–28, 2001.

[137] B. Heymann and H. Grubmüller. Dynamic force spectroscopy of molecular adhesion bonds. *Phys. Rev. Lett.* 84(26):6126–6129, 2000.

[138] F. Rico and V. T. Moy. Energy landscape roughness of the streptavidin-biotin interaction. *J. Mol. Recognition* 20(6):495–501, 2007.

[139] H. Li, M. Rief, F. Oesterhelt, and H. E. Gaub. Single-Molecule Force Spectroscopy on Xanthan by AFM. *Advanced Materials* 10(4):316–319, 1998.

[140] M. Rief, M. Gautel, F. Oesterhelt, J. M. Fernandez, and H. E. Gaub. Reversible unfolding of individual titin immunoglobulin domains by AFM. *Science* 276(5315):1109–1112, may 1997.

[141] C. Jarzynski. Nonequilibrium Equality for Free Energy Differences. *Phys. Rev. Lett.* 78(14):2690–2693, 1997.

[142] G. Hummer and A. Szabo. Free energy reconstruction from nonequilibrium single-molecule pulling experiments. *Proc. Natl. Acad. Sci. U. S. A.* 98(7):3658–3661, 2001.

[143] J. Preiner, H. Janovjak, C. Rankl, H. Knaus, D. A. Cisneros, A. Kedrov, F. Kienberger, D. J. Muller, and P. Hinterdorfer. Free energy of membrane protein unfolding derived from single-molecule force measurements. *Biophys. J.* 93(3):930–937, 2007.

[144] L. D. Landau and E. M. Lifshitz. Theory of elasticity. *Course of theoretical physics*, third edition, vol. 7. Butterworth-Heinemann, 1986.

[145] J. L. Hutter and J. Bechhoefer. Calibration of atomic-force microscope tips. *Rev. Sci. Instrum.* 64(7):1868–1873, 1993.

[146] N. Whisman, D. York, L. Manning, J. Brant, R. Dyer, A. Childress, E. A. Marchand, and J. D. Adams. Probing microplatform for the study of biological adhesion forces. *Rev. Sci. Instrum.* 74(10):4491–4494, 2003.

[147] E. Sackmann. Supported membranes: Scientific and practical applications. *Science* 271:43–48, 1996.

[148] T. Spangenberg, N. F. de Mello, T. B. Creczynski-Pasa, A. A. Pasa, and H. Niehus. AFM in-situ characterization of supported phospholipid layers formed by solution spreading. *Phys. Stat. Sol.* 201(5):857–860, 2004.

[149] P. S. Cremer and S. G. Boxer. Formation and spreading of lipid bilayers on planar glass supports. *J. Phys. Chem. B* 103:2554–2559, 1999.

[150] R. P. Richter and A. Brisson. Characterization of lipid bilayers and protein assemblies supported on rough surfaces by atomic force microscopy. *Langmuir* 19(5):1632–1640, 2003.

[151] R. P. Richter, R. Brat, and A. R. Brisson. Formation of solid-supported lipid bilayers: an integrated view. *Langmuir* 22(8):3497–3505, 2006.

[152] A. Y. Morozov, E. Pronina, A. B. Kolomeisky, and M. N. Artyomov. Solutions of burnt-bridge models for molecular motor transport. *Phys. Rev. E* 75(3):031910, 2007.

[153] M. N. Artyomov, A. Y. Morozov, and A. B. Kolomeisky. Molecular motors interacting with their own tracks. *Phys. Rev. E* 77(4):040901, 2008.

[154] I. M. Cheeseman, S. Anderson, M. Jwa, E. M. Green, J.-s. Kang, J. R. Yates, C. S. Chan, D. G. Drubin, and G. Barnes. Phospho-Regulation of Kinetochore-Microtubule Attachments by the Aurora Kinase Ipl1p. *Cell* 111(2):163–172, 2002.

[155] M. M. Shimogawa, B. Graczyk, M. K. Gardner, S. E. Francis, E. A. White, M. Ess, J. N. Molk, C. Ruse, S. Niessen, J. R. Yates, E. G. Muller, K. Bloom, D. J. Odde, and T. N. Davis. Mps1 phosphorylation of Dam1 couples kinetochores to microtubule plus ends at metaphase. *Curr. Biol.* 16(15):1489–1501, 2006.

[156] A. J. Hunt and J. R. McIntosh. The dynamic behavior of individual microtubules associated with chromosomes in vitro. *Mol. Biol. Cell* 9(10):2857–2871, 1998.

[157] J. W. Armond. Modelling the force-generating properties of depolymerising microtubules. Master's thesis, University of Warwick, 2006.

[158] P. M. Chaikin and T. C. Lubensky. *Principles of condensed matter physics*. Cambridge University Press, Cambridge, 1995.

[159] R. M. Corless, G. H. Gonnet, D. E. G. Hare, D. J. Jeffrey, and D. E. Knuth. On the Lambert *W* function. *Adv. Comp. Math.* 5(1):329–359, 1996.

[160] D. R. Gestaut, B. Graczyk, J. Cooper, P. O. Widlund, A. Zelter, L. Wordeman, C. L. Asbury, and T. N. Davis. Phosphoregulation and depolymerization-driven movement of the Dam1 complex do not require ring formation. *Nat. Cell Biol.* 10(4):407–414, 2008.

[161] A. P. Joglekar, D. Bouck, K. Finley, X. Liu, Y. Wan, J. Berman, X. He, E. Salmon, and K. S. Bloom. Molecular architecture of the kinetochore-microtubule attachment site is conserved between point and regional centromeres. *J. Cell Biol.* 181(4):587–594, 2008.

[162] J. L. Miranda, D. S. King, and S. C. Harrison. Protein Arms in the Kinetochore-Microtubule Interface of the Yeast DASH Complex. *Mol. Biol. Cell* 18(7):2503–2510, 2007.

[163] P. W. Atkins. *Physical chemistry*. Oxford University Press, Oxford, third edition, 1986.

[164] H. A. Kramers. Brownian motion in a field of force and the diffusion model of chemical reactions. *Physica* 7:284–304, 1940.

[165] N. V. Agudov and A. N. Malakhov. Nonstationary diffusion through arbitrary piecewise-linear potential profile. Exact solution and time characteristics. *Radiophys. Quant. Electron.* 36(2):97–109, 1993.

[166] A. N. Malakhov and A. L. Pankratov. Evolution times of probability distributions and averages - exact solutions of the Kramers' problem. *Adv. Chem. Phys.* 121:357–438, 2002.

[167] G. B. Arfken and H. J. Weber. *Mathematical methods for physicists*. Elsevier Academic Press, Amsterdam, sixth edition, 2005.

[168] F. Gittes, B. Mickey, J. Nettleton, and J. Howard. Flexural rigidity of microtubules and actin filaments measured from thermal fluctuations in shape. *J. Cell Biol.* 120(4):923–934, 1993.

[169] V. VanBuren, D. J. Odde, and L. Cassimeris. Estimates of lateral and longitudinal bond energies within the microtubule lattice. *Proc. Natl. Acad. Sci. U. S. A.* 99(9):6035–6040, 2002.

[170] A. Rényi. On the theory of order statistics. *Acta Math. Hungarica* 4(3):191–231, 1953.

[171] B. C. Arnold, N. Balakrishnan, and H. N. Nagaraja. *A first course in order statistics*. John Wiley and Sons, Inc., 1992.

[172] D. E. Knuth. Fundamental algorithms. *The art of computer programming*, third edition, vol. 1. Addison-Wesley, 1997.

[173] W. Feller. *An introduction to probability theory and its applications*, vol. 1. Wiley, New York, 1968.

[174] S. Redner. *A guide to first passage processes*. Cambridge University Press, 2001.

[175] E. T. O'Brien, E. D. Salmon, and H. P. Erickson. How calcium causes microtubule depolymerization. *Cell Motil. Cytoskel.* 36:125–135, 1997.

[176] A. W. Hunter, M. Caplow, D. L. Coy, W. O. Hancock, S. Diez, L. Wordeman, and J. Howard. The kinesin-related protein MCAK is a microtubule depolymerase that forms an ATP-hydrolyzing complex at microtubule ends. *Mol. Cell* 11(2):445 – 457, 2003.

[177] P. B. Schiff, J. Fant, and S. B. Horwitz. Promotion of microtubule assembly *in vitro* by taxol. *Nature* 277(5698):665–667, Feb. 1979.

[178] M. Fixman. Effects of fluctuating hydrodynamic interaction. *J. Chem. Phys.* 78(3):1594–1599, 1983.

[179] M. Doi and S. Edwards. *The theory of polymer dynamics*. Oxford University Press, 1986.

[180] U. M. Ascher and R. D. Russell. Reformulation of boundary value problems into "standard" form. *SIAM Rev.* 23(2):238–254, 1981.

[181] H. J. Kelley. Method of gradients. *Optimization techniques: with applications to aerospace systems*, pp. 206–252. Academic Press, New York, 1962.

[182] R. Courant. Variational methods for the solutions of problems of equilibrium and vibrations. *Bull. Amer. Math. Soc.* 49:1–23, 1943.

[183] W. I. Zangwill. Non-linear programming via penalty functions. *Man. Sci.* 13(5):344–358, 1967.

[184] U. Ascher, J. Christiansen, and R. Russell. COLSYS: A collocation code for boundary-value problems. *Codes for Boundary-Value Problems in Ordinary Differential Equations*, vol. 76, pp. 164–185. Springer, Berlin, Lecture Notes in Computer Science, 1979.

[185] E. J. Doedel, A. R. Champneys, T. F. Fairgrieve, Y. A. Kuznetsov, B. Sandstede, and X. Wang. Auto97: Continuation and bifurcation software for ordinary differential equations. Tech. rep., Concordia University, Montreal, Quebec, Canada, 1997.

[186] J. Kim, G. Kim, and P. S. Cremer. Investigation of water structure at the solid/liquid interface in the presence of supported lipid bilayers by vibrational sum frequency spectroscopy. *Langmuir* 17:7255–7260, 2001.

[187] M. Jansen and A. Blume. A comparative study of diffusive and osmotic water permeation across bilayers composed of phospholipids with different head groups and fatty acyl chains. *Biophys. J.* 68(3):997–1008, 1995.

[188] L. D. Landau and E. M. Lifshitz. Fluid mechanics. *Course of theoretical physics*, second edition, vol. 6. Pergamon, 1987.

[189] C. Das, H. S. Khizar, P. D. Olmsted, and S. D. Connell. Nano-scale mechanical probing of supported lipid bilayers with atomic force microscopy. *Phys. Rev. E* 82:041920, June 2010.

[190] L. D. Landau and E. M. Lifshitz. Statistical physics part 1. *Course of theoretical physics*, third edition, vol. 5. Butterworth-Heinemann, 1980.

[191] H. J. Butt and M. Jaschke. Calculation of thermal noise in atomic force microscopy. *Nanotech.* 6(1):1–7, 1995.

[192] W. H. Press, B. P. Flannery, S. A. Teukolsky, and W. T. Vetterling. Numerical recipes in C: The art of scientific computing. chapter 12, p. 438. Cambridge University Press, 1988.

[193] J. Jang, G. C. Schatz, and M. A. Ratner. Capillary force in atomic force microscopy. *J. Chem. Phys.* 120(3):1157–1160, 2004.

[194] D. Albanese, S. Merler, G. Jurman, R. Visintainer, and C. Furlanello. Mlpy machine learning py, 2010.

[195] C. Torrence and G. P. Compo. A practical guide to wavelet analysis. *Bull. Amer. Met. Soc.* 79:61–78, 1997.

[196] J. Canny. A computational approach to edge detection. *IEEE Trans. Pat.* 8:679–698, 1986.

[197] Z. V. Leonenko, E. Finot, H. Ma, T. E. S. Dahms, and D. T. Cramb. Investigation of temperature-induced phase transitions in DOPC and DPPC phospholipid bilayers using temperature-controlled scanning force microscopy. *Biophys. J.* 86(6):3783–3793, 2004.

[198] S. Loi, G. Sun, V. Franz, and H.-J. Butt. Rupture of molecular thin films observed in atomic force microscopy. II. Experiment. *Phys. Rev. E* 66(3):031602, 2002.

[199] W. Rawicz, K. Olbrich, T. McIntosh, D. Needham, and E. Evans. Effect of chain length and unsaturation on elasticity of lipid bilayers. *Biophysical Journal* 79(1):328 – 339, 2000.

[200] M. F. Kanninen and C. H. Popelar. *Advanced fracture mechanics*. Oxford University Press, 1985.

[201] E. L. Grishchuk, I. S. Spiridonov, V. A. Volkov, A. Efremov, S. Westermann, D. Drubin, G. Barnes, F. I. Ataullakhanov, and J. R. McIntosh. Different assemblies of the DAM1 complex follow shortening microtubules by distinct mechanisms. *Proc. Natl. Acad. Sci. U. S. A.* 105(19):6918–6923, 2008.

[202] A. P. Joglekar, D. C. Bouck, J. N. Molk, K. S. Bloom, and E. D. Salmon. Molecular architecture of a kinetochore-microtubule attachment site. *Nat. Cell Biol.* 8(6):581–585, 2006.

[203] B. N. J. Persson. Sliding friction. *Surf. Sci. Rep.* 33(3):83 – 119, 1999.

[204] A. Einstein and R. Fürth. *Investigations on the theory of the Brownian movement*. Courier Dover Publications, 1956.

[205] N. G. van Kampen. *Stochastic processes in physics and chemistry*. Elsevier, Amsterdam, third edition, 2007.

[206] R. P. Feynman, R. B. Leighton, and M. Sands. *The Feynman Lectures on Physics*, vol. 1. Pearson/Addison-Wesley, San Francisco, definitive edition, 2006.

[207] P. Reimann. Brownian motors: noisy transport far from equilibrium. *Physics Rep.* 361(2-4):57 – 265, 2002.

[208] C. S. Peskin, G. M. Odell, and G. F. Oster. Cellular motions and thermal fluctuations: the Brownian ratchet. *Biophys. J.* 65(1):316–324, 1993.

[209] H. B. Keller. *Numerical Methods for Two-Point Boundary-Value Problems*. Blaisdell Publishing Company, 1968.

[210] W. H. Press, B. P. Flannery, S. A. Teukolsky, and W. T. Vetterling. *Numerical Recipes in C: The Art of Scientific Computing*. Cambridge University Press, 1988.

[211] U. M. Ascher, R. M. M. Mattheij, and R. D. Russell. *Numerical Solution of Boundary Value Problems for Ordinary Differential Equations*. Society for Industrial and Applied Mathematics, 1995.

[212] C. W. Gear. *Numerical Initial Value Problems in Ordinary Differential Equations*. Prentice-Hall, 1971.

[213] H. B. Keller. Numerical solution of bifurcation and nonlinear eigenvalue problems. *Applications of bifurcation theory*. Academic Press, New York, 1977.

# A

# Useful mathematical results

## A.1 Lambert-$W$ function

The Lambert-$W$ function $W(z)$ is defined as the solution of the equation

$$W(z)e^{W(z)} = z. \tag{A.1}$$

Thus, using the Lambert-$W$ function, equations of the form

$$ye^{y} = x, \tag{A.2}$$

can be simply solved in terms of $W$

$$y = W(x). \tag{A.3}$$

In general, $W(z)$ is complex multivalued. However, for nonnegative real $z$ the principal branch takes on real values, and is the only branch of interest to us in order to solve equations of the form (A.2). The principal branch is shown in Figure A.1. An in-depth discussion of the Lambert-$W$ function, and it's uses, can be found in Corless et al. [159].

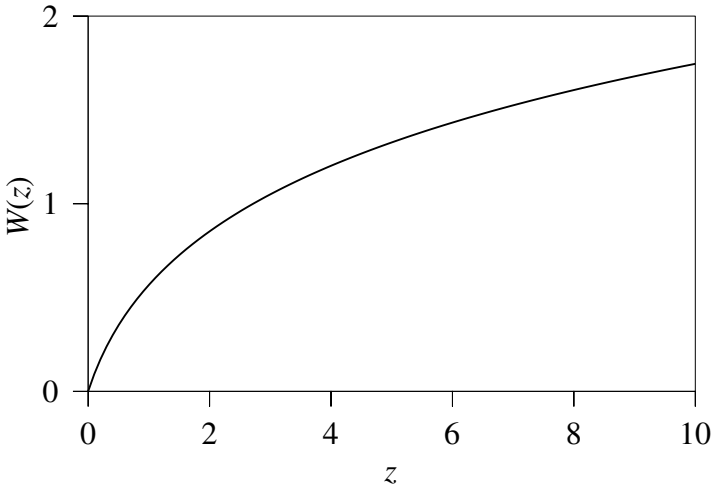


**Figure A.1:** The principal branch of the Lambert-$W$ function for real $x$.

## A.2 Binomial coefficients

The binomial coefficient is defined as

$$\binom{n}{j} = \frac{n(n-1)\dots(n-j+1)}{j(j-1)\dots(1)} \tag{A.4}$$

$$= \frac{n!}{j!(n-j+1)!} \tag{A.5}$$

$$= \prod_{k=1}^{j} \frac{n-k+1}{k}. \tag{A.6}$$

The identity used in (4.60) can be derived as follows

$$\begin{aligned}\binom{n}{j}(-1)^j &= (-1)^j \frac{n(n-1)\dots(n-j+1)}{j!} \\ &= (-1)^{j-1} \frac{(-n)(1-n)\dots(j-n-1)}{j!} \\ &= (-1)^{j-1} \frac{((j-1)-n)((j-2)-n)\dots(-n)}{j!} \\ &= \binom{j-n-1}{j},\end{aligned} \tag{A.7}$$

by (A.4), and cancelling $(-1)^{j-1}$ because are exactly $j-1$ negative terms in the numerator. See also [172] for many other binomial identities.

## A.3 Order statistics

A set of $n$ random variables $\{X_1, X_2, \ldots, X_n\}$ has the order statistics $\{X_1^*, X_2^*, \ldots, X_n^*\}$, where $X_1^* < X_2^* < \cdots < X_n^*$. Of specific interest for the calculations in §4.2.2 is $Y = \max X_i = X_n^*$. The following derivation for the exponential distribution special case follows the example of Rényi [170].

Suppose we have $n$ independently, exponentially distributed random variables $\{X_1, X_2, \ldots, X_n\}$, with mean $\lambda^{-1}$. Therefore

$$\mathbb{P}(X_i < t) = 1 - e^{-\lambda t}. \tag{A.8}$$

Let $Y$ be a random variable such that $Y = \max X_i$. Define

$$X_k^* = \mathcal{G}(X_1, \ldots, X_n; k), \tag{A.9}$$

where $\mathcal{G}$ is a function mapping the sequence $\{X_i\}$ to its $k^{\text{th}}$ smallest value. For example, $X_1^* = \mathcal{G}(X_1, \ldots, X_n; 1) = \min\{X_i\}$. Thus $\{X_i^*\}$ is the sequence $\{X_i\}$ arranged in order of magnitude. Hence

$$Y = X_1^* + (X_2^* - X_1^*) + (X_3^* - X_2^*) + \cdots + (X_n^* - X_{n-1}^*) = X_n^*. \tag{A.10}$$

Denote the differences between consecutive order statistics by $\delta_k \equiv (X_k^* - X_{k-1}^*)$, taking $X_0^* \equiv 0$. Hence

$$Y = \sum_{i=1}^{n} \delta_i. \tag{A.11}$$

We will now determine the distribution of the differences $\delta_i$. Consider

$$\mathbb{P}(X_{k+1}^* - X_k^* > t | X_k* = s) = P(X_{k+1}^* > t + s | X_k^* = s). \tag{A.12}$$

This states that none of the $n - k$ remaining waiting times expires before the $t + s$. The memoryless property of the exponential distribution implies

$$\mathbb{P}(X < t + s | X \geq s) = P(X < t) \tag{A.13}$$

Therefore the probability, due to the memoryless property and the mutual independence of $X_i$, is

$$(\mathbb{P}(X_i > t))^{n-k} = e^{-(n-k)\lambda t}. \tag{A.14}$$

Therefore,

$$\mathbb{P}(X_{k+1}^* - X_k^* < t | X_k^* = s) = 1 - e^{-(n-k)\lambda t}, \tag{A.15}$$

which does not depend on $s$, so

$$\mathbb{P}(X^*_{k+1} - X^*_k < t) = 1 - e^{-(n-k)\lambda t}. \tag{A.16}$$

Hence $\delta_k \equiv X^*_k - X^*_{k-1}$ is exponentially distributed and the expectation is

$$\mathbb{E}(\delta_k) = \frac{1}{(n-k+1)\lambda}. \tag{A.17}$$

Finally the expectation of $Y$ is the sum of the expectation of the differences $\delta_k$

$$\begin{aligned}
\mathbb{E}(Y) &= \sum_{k=1}^{n} \mathbb{E}(\delta_k) \\
&= \sum_{k=1}^{n} \frac{1}{(n-k+1)\lambda} \\
&= \frac{1}{\lambda} \sum_{k=1}^{n} \frac{1}{(n-k+1)} \\
&= \frac{H_n}{\lambda},
\end{aligned} \tag{A.18}$$

where $H_n = \sum_{i=1}^{n} 1/i$ is the $n^{\text{th}}$ harmonic number [172].

# B

# Theoretical background

The theoretical arguments employed in chapters Chapter 4 and Chapter 5 rely heavily on some general principles and formulations. A brief outline of these is given here for reference.

## B.1 Brownian motion

Brownian motion refers to the rapid and random changing of direction of small – but large enough to be visible – particles, when suspended in a fluid of much smaller, invisible particles. The large particles travel in a straight line for only a short time, before the constant buffeting of the smaller particles cause a change of direction.

In 1905, Einstein explained theoretically the Brownian motion [204]. Restricting attention to the $x$-component of velocity, it is clear that $\langle v_x \rangle = 0$, where $\langle \cdot \rangle$ denotes the mean average, as it is equally likely that particles are jostled to the left as to the right. Of course, velocity *fluctuations* are clearly visible in the experiment. The diffusion equation of particles following a Brownian motion is

$$\frac{\partial P}{\partial t} = D \frac{\partial^2 P}{\partial x^2}, \tag{B.1}$$

where $P$ can be viewed as the probability of finding a particle at $x$ at time $t$. However, for one-dimensional (1D) Brownian motion the diffusion coefficient is

$$D = \frac{\langle (\Delta x)^2 \rangle}{2\Delta t}. \tag{B.2}$$

Einstein showed that

$$D = \mu k_B T, \tag{B.3}$$

also holds, where $\mu$ is the mobility of the particle in the fluid, relating drift velocity to force $v_x = F_x \mu$, and so

$$\frac{\langle (\Delta x)^2 \rangle}{2\Delta t} = \mu k_B T. \tag{B.4}$$

This important relation, known as the Einstein relation, provides a deep connection between fluctuations and dissipation [205].

## B.2 Brownian ratchets

In addition to the most well-known cellular biological motors – the biochemical protein motors, such as kinesin, dynein, and myosin – there are also a number of other processes that produce directed transport by a nonequilibrium process, collectively known as Brownian motors or ratchets.

Feynman (and previously Smoluchowski) used the example of a ratchet and pawl to illustrate the second law of thermodynamics [206]. In order to harness the force from molecular collisions the ratchet and pawl have to be microscopically small. Due to their small size, they themselves are then subject to thermal fluctuations. At thermal equilibrium the probability of the ratcheted process going backwards, against the pawl, is equal to the probability of going forward, and hence no work can be extracted. For such a ratchet system to produce work it must be driven out of equilibrium [207].

In biological systems, it is possible for such a system to operate through nonequilibrium growth or depletion of a polymer. For example, a polymer growing against a membrane may exert a force on the membrane. The polymer grows in integral lengths of $L$, but only if not obstructed by the membrane. The membrane, experiencing thermal fluctuations around point $x$, is occasionally sufficiently removed from the tip of the growing polymer that a new monomer can bind. With the extension to the polymer, the membrane is prevented from relaxing and now fluctuates around $x + L$. Thus, the polymer produces an effective force. The critical difference between the polymer system and Feynman's ratchet is that free energy is consumed in the binding of monomers to the tip of the polymer effectively making the process irreversible [208].

A Brownian ratchet may also drive the motion of a particle. Consider the following 'perfect' Brownian ratchet. Suppose the particle is diffusing in 1D with diffusion coefficient $D$. If, at intervals of $\delta$, boundaries are placed such that the particle can cross a boundary in the positive $x$ direction only, then the motion

of the particle will be 'ratcheted' towards the positive $x$ direction. On average, the particle crosses the distance $\delta$ between boundaries in a time $t = \delta^2/2D$, and therefore has a velocity of $v = \delta/t = 2D/\delta$. Such a ratchet can again be physically realised by a particle diffusing along the length of a depolymerising polymer, with the condition that polymeric subunits can only detach after the particle has travelled away from the end of the polymer [208]. These types of Brownian ratchets have also been called *burnt-bridges models* [152, 153], and have been used to model Dam1 diffusion on MTs in Chapter 4.

## B.3 Fokker-Planck equation

It is often useful to have a representation of Brownian motion is terms of a probability distribution. The Fokker-Planck equation [205] is a partial differential equation (PDE) describing the time evolution of a probability distribution

$$\frac{\partial P(x,t)}{\partial t} = -v\frac{\partial P(x,t)}{\partial x} + D\frac{\partial^2 P(x,t)}{\partial x^2} \tag{B.5}$$

where $D$ is the diffusion coefficient and $v$ is the drift velocity. In general these coefficient can be more general functions of $x$, but the form in (B.5) provides a direct link to Brownian motion through the diffusion equation (B.1) and the Einstein relation (B.3).

## B.4 Kramers' escape problem

Consider a particle trapped in the potential well of a free-energy profile as in Figure B.1. The particle requires an energy $\Delta V$ to overcome the barrier and escape the well. Flexibility in the choice of coordinate $x$ allows this model wide applicability for chemical reactions, or protein unbinding for example. If $\Delta V \gg k_B T$ the particle will remain in the metastable state for some time. Eventually, it will receive enough energy, due to fluctuations from the thermal bath, and scale the barrier. The rate at which this occurs is known as the Kramers escape rate (this problem was considered by Kramers in 1940 [164]). An empirical relation, the Arrhenius law, gives the rate $r$ up to a constant of proportionality

$$r \propto \exp(-\Delta V/k_B T). \tag{B.6}$$

In the escape problem, the particle experiences a force due to the potential

$$F(x) = -\frac{dV(x)}{dx} \tag{B.7}$$

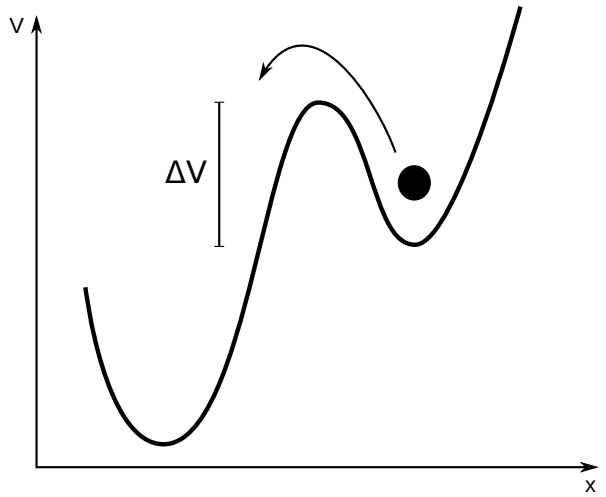


**Figure B.1:** The Kramers escape problem. A particle diffusing in a double-well potential $V(x)$, on some reaction coordinate $x$.

With this force, and the assumption that the particle motion is over-damped, the Fokker-Planck equation is found to be useful for the escape problem, and is formulated as in (B.5) with $v = F(x)/\mu$. Note also that, using the Einstein relation (B.3), we can rewrite (B.5) as

$$\frac{\partial P(x,t)}{\partial t} = D\frac{\partial}{\partial x}\left(P(x,t)\frac{1}{k_B T}\frac{\partial V(x)}{\partial x} + \frac{\partial P(x,t)}{\partial x}\right) \tag{B.8}$$

## B.5 Stokes' law

For many small particles, the diffusion coefficient $D$ can be well-approximated by assuming the particle to be spherical, for which $D$ can be obtained via Stokes' law. The mobility $\mu$ for a spherical particle of radius $a$ in a fluid of viscosity $\eta$ is given by [158]

$$\mu = \frac{1}{6\pi\eta a}. \tag{B.9}$$

Using Einstein's relation (B.3), we find the diffusion coefficient to be

$$D = \frac{k_B T}{6\pi\eta a}. \tag{B.10}$$

# C

# Numerical solution of boundary value problems

A boundary value problem (BVP) is an ordinary differential equation (ODE), or system thereof, subject to equality constraints at each end of the limits of integration. Very often it is not possible to analytically solve nonlinear boundary value problems, and so numerical solution methods are important. In general, we require a solution of the system of $n$ coupled, first-order ODEs

$$\frac{dy_i(x)}{dx} = f_i(x, y_1(x), \ldots, y_n(x)), \qquad i = 1, \ldots, n, \quad x_a \leq x \leq x_b, \tag{C.1}$$

subject to the boundary conditions

$$B_j(y_1(x_a), \ldots, y_n(x_a)) = 0, \qquad j = 1, \ldots, n_1 \tag{C.2}$$

$$B_k(y_1(x_b), \ldots, y_n(x_b)) = 0, \qquad k = n_1 + 1, \ldots, n, \quad x_a < x_b. \tag{C.3}$$

Higher-order equations are trivially transformed to a set of first-order equations by introducing a new variable for each higher derivative. Boundary conditions depending on the values of the variables $y_i$ at either only $x_a$ or only $x_b$ are called separated boundary conditions. Non-separated boundary conditions can be transformed into separated boundary conditions by introducing an additional variable [180]. To be well-defined the BVP must have $n$ boundary conditions. A brief description follows of the two most common methods for the numerical solution of BVPs: *shooting* and *finite difference* [209–211].

## C.1 Shooting methods

Shooting is a conceptually simple technique for solving BVPs. To begin we require a suitable initial guess for $y_1(x_a), \ldots, y_n(x_a)$, which must satisfy the $n_1$ conditions defined by (C.2). This leaves $n_2 = n - n_1$ degrees of freedom in $y_i(x_a)$. To shoot, we integrate (C.1) from $x_a$ using the initial guess by standard initial value problem (IVP) techniques (for example, explicit Runge-Kutta or implicit Gear [212]) up to $x_b$. At this boundary it is highly unlikely that (C.3) will have been satisfied by the $y_i(x_b)$, and the discrepancies are

$$\xi_k = B_k(y_1(x_b), \ldots, y_n(x_b)), \qquad k = n_1 + 1, \ldots, n. \tag{C.4}$$

Since we are aiming for $\xi_k = 0$, we apply an iteration of the Newton-Raphson method to compute a new initial guess $y_i(x_a)$. Equation (C.1) is then integrated again with the new guess. The procedure is iterated until the desired tolerance on $\xi_k$ is reached.

## C.2 Finite difference methods

Finite difference methods rely on replacing the ODE system with a set of approximating equations defined on a mesh over the solution interval. For some BVPs, finite difference methods are more effective because they do not require an IVP solver, which can be sensitive to extraneous intermediate 'solutions' encountered while iterating towards the final solution.

Defining the mesh as

$$x_a = x_1 < x_2 < \cdots < x_m = x_b, \tag{C.5}$$

we then can then discretise each ODE in (C.1) as follows[1]

$$\frac{y_i(x_{j+1}) - y_i(x_j)}{x_{j+1} - x_j} = f(\frac{1}{2}(x_{j+1} - x_j), \frac{1}{2}(y_1(x_j) + y_1(x_{j+1})), \ldots, \frac{1}{2}(y_n(x_j) + y_n(x_{j+1}))),$$
$$j = 1, \ldots, m-1, \quad i = 1, \ldots, n. \tag{C.6}$$

Starting with an initial guess, approximately satisfying (C.6), (C.2) and (C.3), a nonlinear equation solver, such as Newton-Raphson, is used to iteratively adjust the values of $y_i$ on the mesh until (C.6), (C.2) and (C.3) are satisfied to within a desired tolerance. To use the finite difference method, it is often necessary to

[1] There are other ways to discretise ODEs. This method is called the midpoint scheme.

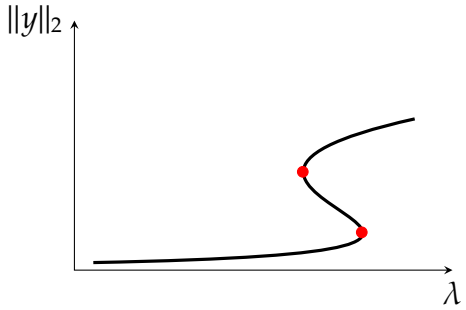


**Figure C.1:** $L_2$-norm of the solution vector of a boundary-value problem with a turning points. The location of the turning points are indicated by red dots. To follow the solution curve, the direction of $\lambda$ iteration must change. This is not possible in normal continuation, as progress on the solution curve will reverse direction as well and retrace its steps.

already have a good initial guess, which may be supplied through a continuation procedure.

## C.3 Continuation

When solving a parametrised nonlinear BVP, that is when

$$f = f(x, y_1, \ldots, y_n; \lambda) \tag{C.7}$$

for a parameter $\lambda$, it is often necessary to supply a good initial guess. Unfortunately, it is also often rather difficult to make a good guess for a desired $\lambda$. However, it may be possible to supply a suitable guess for a different $\lambda_0$. The solution obtained for this $\lambda_0$ can be used as the initial guess for the BVP with parameter $\lambda_1 = \lambda_0 + \delta\lambda$, a small step closer to the target value. Continuing iteratively, the solution with parameter $\lambda$ can be obtained, without the need to provide a initial guess. This procedure is called continuation.

### C.3.1 Pseudo-arclength continuation

Continuation fails when the procedure encounters a *turning point*. If we imagine the solution of the BVP for a given $\lambda$ as occupying a point in an $n+1$-dimensional space, then the continuation procedure of §C.3 traces out a curve in this space. For some problems the solution curve doubles back on itself, after reversing direction of $\lambda$. An example of this is shown in Figure C.1, with the $L_2$-norm used to represent the $n$-dimensional solution vector.

Keller proposed an alternative continuation technique called pseudo-arclength continuation. This requires an addition equation to be added to the BVP, increas-

ing the dimensionality of the solution to $n+1$ and imposing an arclength constraint on the solution curve. The solution at the desired $\lambda$ is again obtained iteratively, via interim solutions, but steps are made in pseudo-arclength $s^*$ rather than in $\lambda$ [213].

## C.4 Boundary conditions at unknown points

Some physical problems may result in a BVP that has a boundary condition defined at an unknown point. For example, in system (C.1), $x_b$ may be an unknown. In this case, a BVP of standard form can be obtained by introducing a trivial ODE and rescaling. Suppose $x_a = 0$ ($x_a \neq 0$ can be accommodated by translation). Letting $z = x/x_b$, the system (C.1) becomes

$$\frac{1}{x_b}\frac{dy_i(z)}{dz} = f_i(z, y_1(z), \ldots, y_n(z)), \qquad i = 1, \ldots, n, \quad 0 \leq z \leq 1, \tag{C.8}$$

$$\frac{dx_b}{dz} = 0 \tag{C.9}$$

$$B_j(y_1(0), \ldots, y_n(0)) = 0, \qquad j = 1, \ldots, n_1 \tag{C.10}$$

$$B_k(y_1(1), \ldots, y_n(1)) = 0, \qquad k = n_1 + 1, \ldots, n. \tag{C.11}$$

## C.5 Integral constraints

An integral

$$\int_{x_a}^{x_b} g(x, y_1, \ldots, y_n)\, dx, \tag{C.12}$$

can be trivially computed as part of the BVP solution process by introducing an additional equation

$$\frac{dI}{dx} = g \tag{C.13}$$

to the ODE system, and adding a boundary condition $I(x_a) = 0$.

This addition may also be used to enforce a constraint such as

$$\int_{x_a}^{x_b} g(x, y_1, \ldots, y_n)\, dx = c, \tag{C.14}$$

by also adding a second boundary condition $I(x_b) = c$.